UNITED STATES DEPARTMENT OF THE INTERIOR

GEOLOGICAL SURVEY

Sedimentologic study of Horizon Guyot, Mid-Pacific Mountains

Edited by

William C. Schwab[1]

Open File Report 86-433

[1] Woods Hole, Massachusetts

1986

REPORT SUMMARY

This report presents and summarizes the preliminary interpretation of sedimentologic data collected on Horizon Guyot, Mid-Pacific Mountains, during two cruises aboard the U.S. Geological Survey research vessel S.P. LEE (Hein and others, 1985a; Schwab and Bailey, 1985). The main objective of these cruises was to study the distribution and composition of ferromanganese-oxide precipitates that encrust the hard substrate of sea floor edifices, such as seamounts and linear volcanic ridges. The concentrations of certain trace metals, such as cobalt, nickel, and platinum, in these Mn crusts are higher than those of abyssal ferromanganese nodules and hydrothermal crusts from spreading centers (Toth, 1968; Craig and others, 1982; Halbach and Manheim, 1984; Hein and others, 1985a, 1986) and thus, appear to be a potential target for commercial exploitation.

Mass wasting and bedload sediment transport appear to influence the thickness of crusts on seamount flanks. Crusts typically are thin and textural evidence of destruction and regrowth of crusts occurs where geophysical and sediment textural evidence suggesting mass movement or bottom-current activity is particularly strong (Hein and others, 1985b). Therefore, the sedimentary environment of these sea floor edifices appears to be a fundamental parameter controlling the distribution and possibly the chemistry of ferromanganese crusts.

Horizon Guyot has been studied more extensively than any other location in the Mid-Pacific Mountains (Heezen, Fischer and others, 1971; Lonsdale and others, 1972; Winterer, Ewing and others, 1973; and references therein). The major emphasis of this report is on new data and interpretations that have become available as a result of the multidisciplinary study of ferromanganese crusts in the central Pacific Ocean.

This report consists of the three chapters listed below:

Chapter I.	Geologic setting and sedimentologic environment of Horizon Guyot by William C. Schwab and Paula J. Quinterno.
Chapter II.	Geotechnical analysis and physical properties of sediment from Horizon Guyot by Robert E. Kayen, Homa J. Lee, and William C. Schwab.
Chapter III.	Current meter and temperature measurements on Horizon Guyot and implications for sediment transport by David A. Cacchione, William C. Schwab, George Tate, and Marlene Noble.

Analysis of high-resolution seismic-reflection profiles, textural and micropaleontologic analysis of sediment gravity cores (Chapter I), and interpretation of current-meter data collected over a 9 month period (Chapter III) show that erosion and redistribution of sediment are important processes affecting the sediment cap of Horizon Guyot. Although these processes may periodically affect the entire summit of Horizon Guyot, they are apparently concentrated around its perimeter. The currents recorded above Horizon Guyot are dominated by internal M_2 (semi-diurnal lunar) tidal flow. These currents are itensified relative to other tidal currents measured in the north central Pacific, and are thought to be the result of topographic intensification of the internal tide that propagates across the guyot's summit. Estimates of the mobility of the Horizon Guyot bottom sediment indicate that the internal tidal currents can cause bedload transport of the near-surface foraminiferal sand during the periods of maximum flow (March-May, flow speed of 43 cm/s). Slope stability analysis (Chapter II) suggests that if the measured overconsolidation of the sediment collected on Horizon Guyot is produced by the current reworking of the surficial sediment and if localized undercutting by bottom currents steepens the sea floor declivity, the sediment capping the summit of Horizon Guyot may be unstable during infrequent earthquake loading. This scenario is proposed as a possible cause of the observed sediment slumping on the northwest perimeter of Horizon Guyot's sediment cap.

I. GEOLOGIC SETTING AND SEDIMENTOLOGIC ENVIRONMENT OF HORIZON GUYOT

by

William C. Schwab and Paula J. Quinterno

Introduction

Horizon Guyot is a 300-km-long, 75-km-wide volcanic ridge with a gently-sloping summit that is diagnostic of guyots (Hess, 1946). It is located in the Mid-Pacific Mountains south of Necker Ridge (Fig. 1-1). Seismic-reflection data have delineated a pelagic sedimentary deposit up to 160-m-thick capping an irregular volcanic basement, thus enhancing the flatness of the summit area (Karig and others, 1970). Seamounts draped by varied thicknesses of unconsolidated sediment have been described in many other areas of the world ocean (for example: Karig and others, 1970; Uchupi and others, 1970; Roberts and others, 1974; Taylor and others, 1975; Heirtzler and others, 1977; Jackson, Koisum and others, 1978; Hein and others, 1985b), however, the physical oceanographic and other environmental processes that affect this sediment are poorly understood (Lonsdale and others, 1972; Roberts and others, 1974; Johnson and Lonsdale, 1976).

Drilling of Horizon Guyot's sediment cap (Deep Sea Drilling Project, DSDP, Site 44; Fig. 1-2) ended with the drillstring twisted off in Eocene chert at a subsurface depth of 75 m (Heezen, Fischer, and others, 1971). The exposure of this same chert bed on the north perimeter of the pelagic sediment cap, bedforms revealed by bottom photos, and near-bottom current meter data indicate the importance of submarine erosion in fashioning the morphology of Horizon Guyot's sediment cap (Lonsdale and others, 1972). It has been suggested that sediment removal and redistribution is performed by accelerated tidal currents (Lonsdale and others, 1972).

This chapter is a synthesis of previous work completed on Horizon Guyot and presents further evidence of erosion obtained from recently collected high-resolution seismic-reflection data and sediment gravity cores. In addition, evidence for the occurence of mass movement on the sediment cap will be presented.

Sampling Methods

Horizon Guyot was surveyed and sampled on USGS cruises L5-83-HW (Hein and others, 1985a) and L9-84-CP (Schwab and Bailey, 1985) utilizing the R/V S.P. LEE. Shipboard navigation was conducted using an integrated LORAN-C-SAT. NAV.-GPS-Dead Reckoning system. The geophysical data, which includes 12 kHz, 3.5 kHz, and 80 in^3 airgun seismic-reflection profiles, bottom camera surveys, hydro-casts, and CTD-O$_2$ probe profiles, are synthesized in Hein and others (1985a, 1985b) and Schwab and Bailey (1985). Bottom sampling techniques include dredging and gravity coring. Dredging results are presented in Hein and others (1985a). Gravity core samples were taken with corers weighing between 2 and 10 kN. These cores were contained within a plastic liner. Once onboard ship, the core liners were sectioned into 1 m lengths. The core sections were capped and sealed with cheesecloth and microcrystalline wax and preserved under refrigeration for shore laboratory testing. At some sites replicate cores were obtained; one was split, described and subsampled, while the other was used for triaxial compression and consolidation testing.

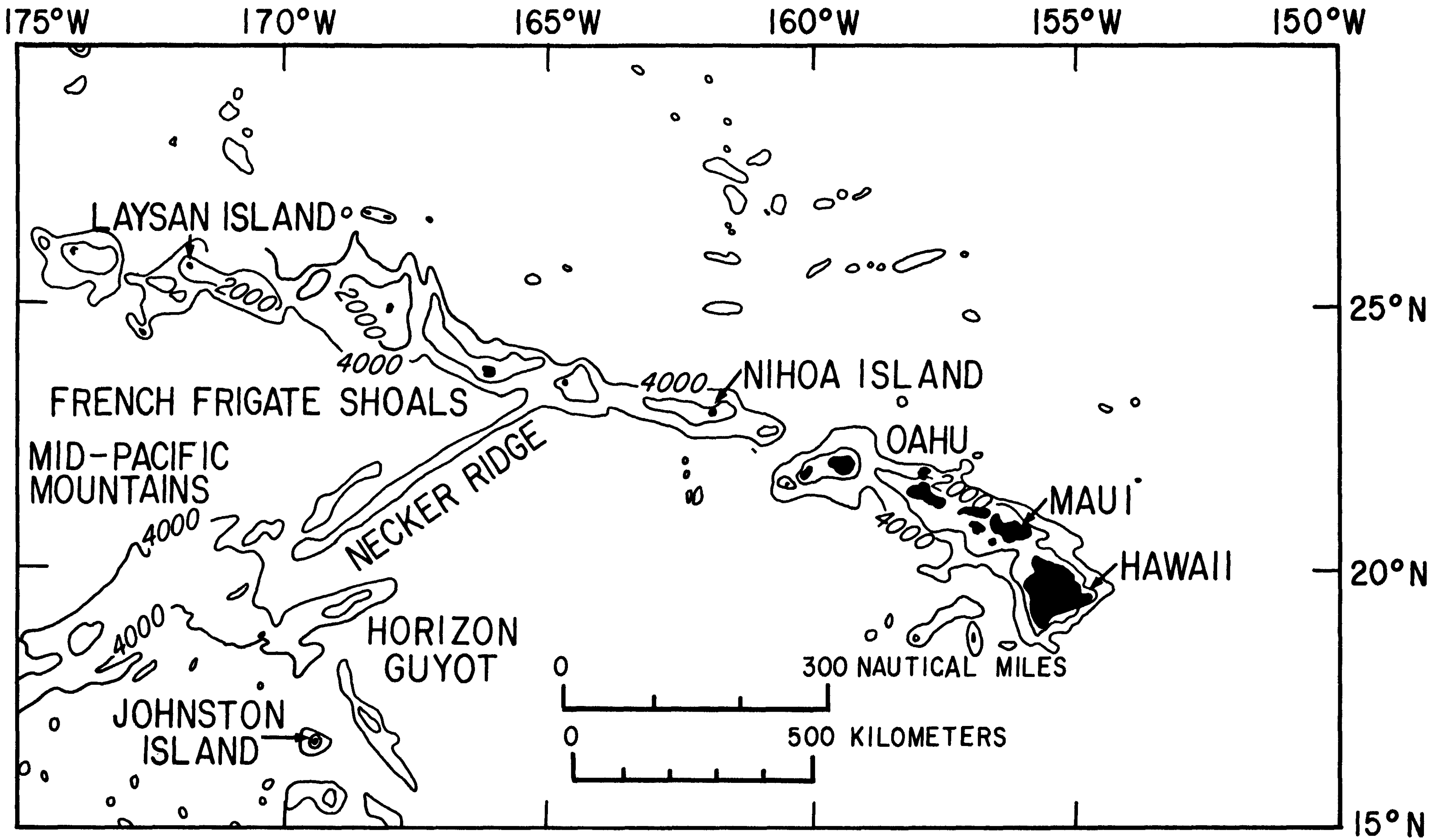

Figure 1-1. Position of Horizon Guyot in the central Pacific Ocean.

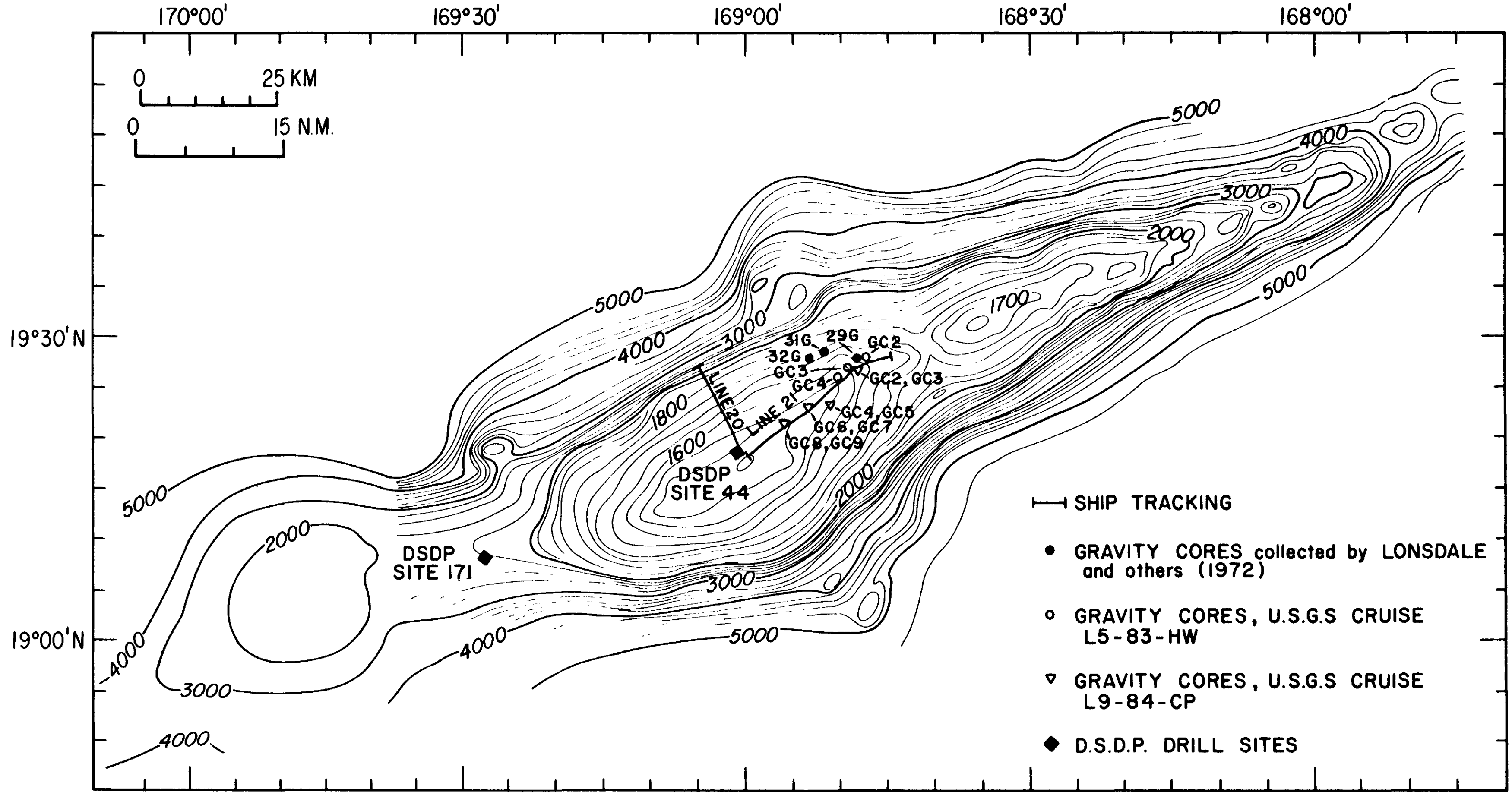

Figure 1-2. Horizon Guyot: Sample locations, drill sites, and ship tracklines. Bathymetry after Lonsdale and others (1972).

Geologic Setting

DSDP Site 171 (Fig. 1-2) reached volcanic basement in a saddle between the two summit platforms of Horizon Guyot, recovering sediment as old as the Cenomanian-Turonian boundary (Winterer, Ewing and others, 1973). The recovery of island or undepleted thoeliites at Site 171 suggests that Horizon Guyot formed close to a mid-ocean spreading ridge (Clague, 1981). Albian foraminifers, associated with basalt clasts in a hyaloclastite dredged near the summit of Horizon Guyot, are the oldest indication of submarine exposure of basalt, while lower Eocene foraminifers associated with hyaloclastite matrix and overlying stratum of middle to lower Eocene nannofossil-foram ooze set the minimum age for cessation of volcanic activity (Lonsdale and others, 1972). The recovery of shallow water limestone, subaerial basalt, and plant remains in the upper Cretaceous sequence of DSDP Site 171 indicates that Horizon Guyot was subaerially exposed from at least early Cenomanian (approximately 100 m.y. BP) to late Turonian-early Coniacian time (approximately 90 m.y. BP) (Winterer, Ewing and others, 1973). Submergence was well underway by Conacian time and it continued through the remainder of the Cretaceous and Tertiary. The similarity in age and geochemistry between basalts from the Mid-Pacific Mountains and the Line Island seamount chain suggests that volcanism in both areas is related and occurred over a span of 40-50 m.y. (Clague, 1981).

The late Cretaceous submergence of Horizon Guyot caused any superficial deposits and volcanic landforms to be buried by pyroclastics and pelagic sediment (Lonsdale and others, 1972). Sedimentation rates interpreted from DSDP results are approximately 3 m/m.y. for the middle Cretaceous, 22 m/m.y. for the late Createceous, and 4 m/m.y. for the early Tertiary (Winterer, Ewing, and others, 1973). Data from DSDP Site 171 on Horizon Guyot and from Sites 165 (sediment apron about 300 km northwest of Kingman Reef, Line Islands Ridge), 168 (west edge of the Central Pacific Basin about 300 km east of Mejit Island, Marshall Islands), and 170 (northwest part of the Central Pacific Basin) indicate very slow or even negative rates of accumulation in post-middle Miocene time (Winterer, Ewing and others, 1973). Cores obtained at these DSDP sites either enter directly into old sediment at the sea floor or within a few meters of the sea floor. A slowing sediment accumulation rate is expected for Horizon Guyot and these other DSDP sites due to their northward movement on the Pacific plate away from the equatorial zone of high productivity. However, results from DSDP Sites 165, 168, and 171 suggest that there has been an increase in erosion and sediment transport by bottom currents sometime in the past 10 m.y., as compared to earlier times (Winterer, Ewing and others, 1973). These effects were felt in deep water along the lower slope of the Marshall Island Arch, near deep passes in the Line Island Seamount Chain, and in shallow water on Horizon Guyot. It has been suggested that this increase in erosion is a consequence of late Cenozoic glaciation and the formation of large quantities of cold bottom water in the circum-Antarctic region (Winterer, 1973).

Horizon Guyot presently is capped by an acoustically transparent blanket of Tertiary nannofossil-foram ooze with intercalated chert layers (Heezen, Fischer, and others, 1971). The thickness of this sediment cap ranges from 160 m on top of the summit platform to a thin veneer around the perimeter of the summit (Lonsdale and others, 1972). Analysis of bottom photographic surveys indicate that sediment from the cap spills over to the guyot's flanks, covering approximately 50 percent of the upper flanks, and seismic-reflection profiles indicate these sediments ultimately form talus deposits at the base of the north and south flanks (Hein and others, 1985a, 1985b).

Flat, hard-rock terraces are exposed at the summit perimeter, especially on the north flank (Lonsdale and others, 1972; Fig. 1-3). Similar terraces have been reported on other seamounts (Hess, 1946; Budinger, 1967; McManus and Morrison, 1968; Pratt, 1963; Hein and others, 1985b; Manheim, 1986). Lonsdale and others (1972) suggest that the terraces found on Horizon Guyot are primary constructional features related to submarine volcanic activity; i.e., the advance of successive foreset beds of pyroclastics or overlapping flows of mobile volcanic debris suddenly "frozen" or dammed behind obstructing volcanic ridges.

Results from a detailed Deep-Tow survey conducted in a 300 km^2 area on the summit platform of Horizon Guyot (Figs. 1-3 and 1-4) suggest that continued erosion is winnowing away the fine-grained nannofossil component of the sediment around the perimeter of the summit platform in water depth from 1570 to 2000 m (Lonsdale and others, 1972). Ripples and sand waves observed on the remaining foram-sand-rich sedimentary lag deposit indicate a net bedload transport of sediment upslope, thus exposing the underlying hard rock terraces (Lonsdale and others, 1972). This erosional beveling of the perimeter of the summit platform creates a sea floor with a 1.6^o to 4^o declivity. The almost flat-lying intercalated chert layers are truncated by this sea floor slope and outcrop. One such chert outcrop dredged in the Deep-Tow survey area is believed to be correlative to the Eocene chert obtained at subsurface depths of 63 and 76 m at DSDP Site 44 (Lonsdale and others, 1972; Fig. 1-4; Outcrop A).

Current measurements collected 12 m above the sea floor (for a maximum duration of 115 hrs) in the Deep-Tow survey area recorded a strong flow dominated by a tidal component with velocities of 1 to 17 cm/sec (Lonsale and others, 1972). It was suggested by those authors that impingement of this tidal current onto Horizon Guyot could create instantaneous velocities adequate to entrain the surficial sediment, and create the erosional features observed around the perimeter of the summit platform. More recent data and the related physical oceanographic processes affecting Horizon Guyot will be discussed in Chapter III.

Previous micropaleontological studies of Horizon Guyot also indicate the affect of erosion and sediment redistribution. Hamilton (1953) reported that two cores collected from the southwest perimeter of Horizon Guyot's pelagic sediment cap contained an Eocene planktonic foraminiferal fauna mixed with modern tropical Pacific foraminifers. Lonsdale and others (1972) described three gravity cores from the deep-tow survey area (Fig. 1-4). Core 29G consists of a Pliocene foram-rich ooze overlain by Quaternary sediment that contains minor amounts of reworked Eocene foraminifers. Cores 31G and 32G, located below a Middle Eocene chert outcrop, contain mostly lower Eocene foraminifers. The occurrence of pre-Quaternary sediment close to the surface of Horizon Guyot's sediment cap has been interpreted to result from active erosion (Lonsdale and others, 1972).

DSDP Site 44 (Fig. 1-2) was not cored in the upper 40 m, so there is no biostratigraphic information for that interval. However, below a subsurface

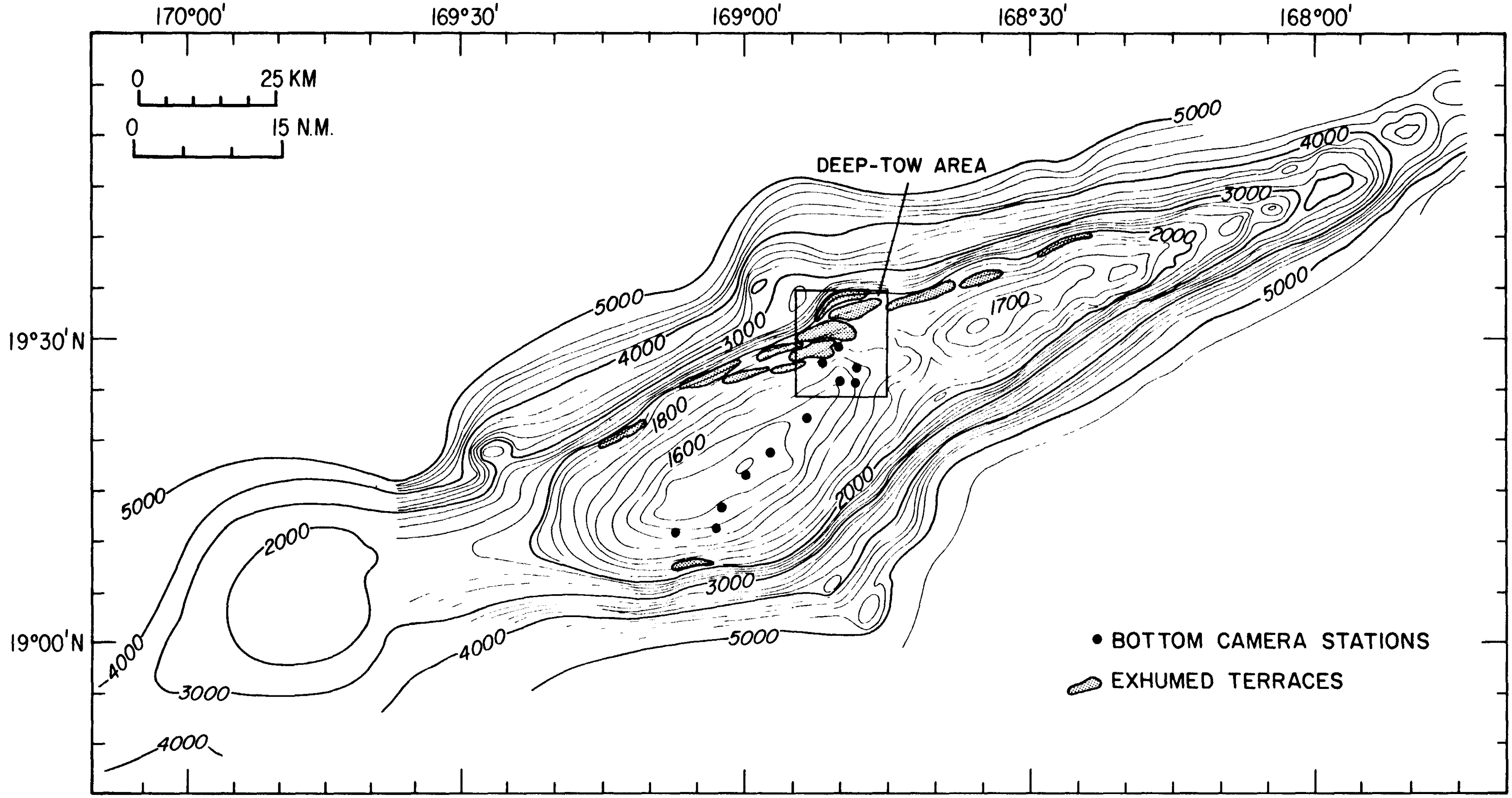

Figure 1-3. Location of exhumed terraces, Deep-Tow survey area, and camera stations on Horizon Guyot (Lonsdale and others, 1972).

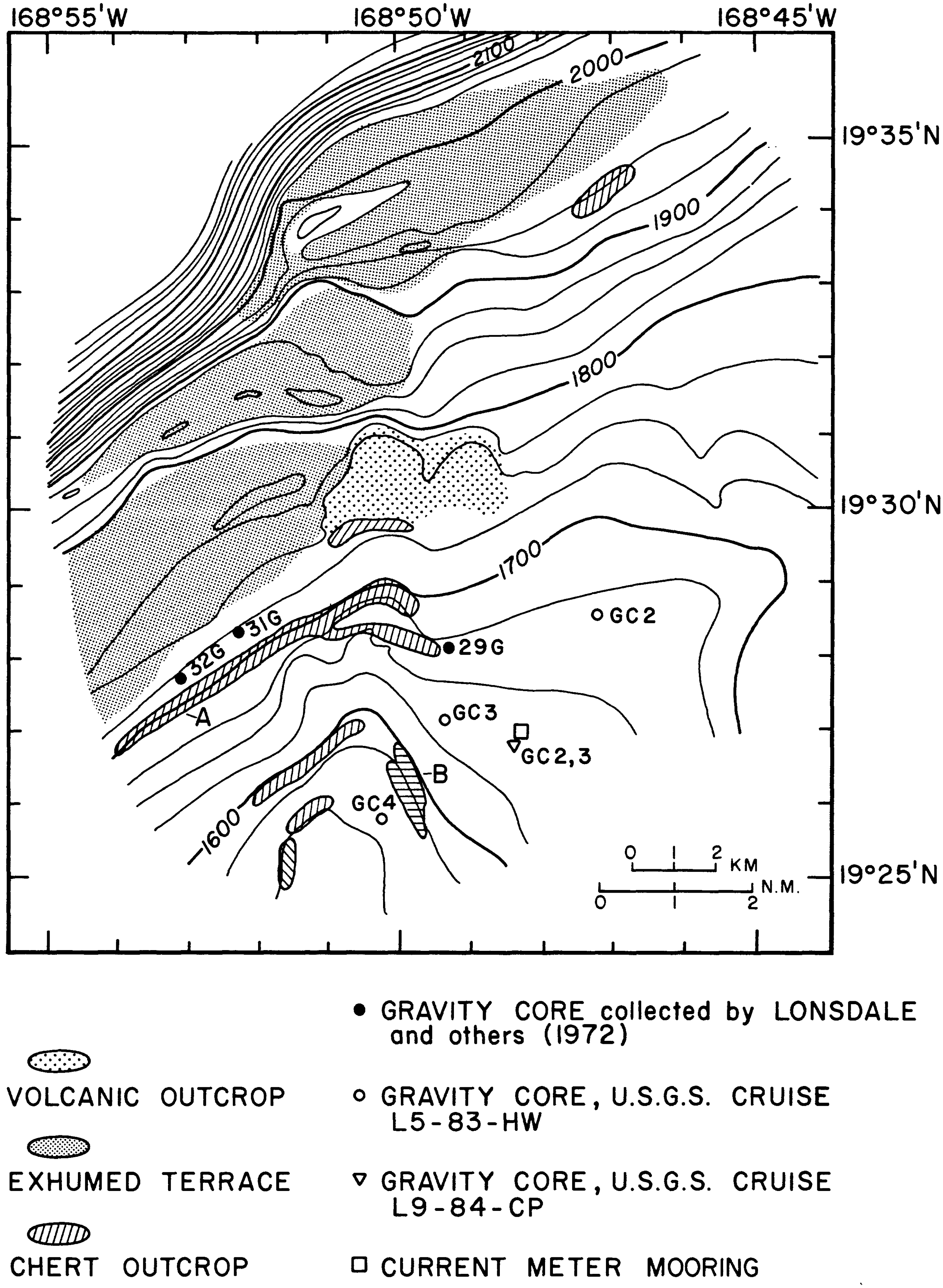

Figure 1-4. Deep-Tow survey area (modified from Lonsdale and others, 1974).

depth of 40 m, the youngest material dated was early Oligocene and this sediment was underlain by upper Eocene and middle Eocene nannofossil ooze (Bukry, 1971; Hay, 1971, Blow, 1971, Krasheninnikov, 1971). Sediment cores collected at DSDP Site 171 (Fig. 1-2) are composed of a mixture of Quaternary, Miocene, Oligocene, and Eocene foraminifers in the upper 14 m while mid Miocene sediment is present at approximately a 27 m subsurface-depth (Douglas, 1973; Roth, 1973; Bukry, 1973). The probable reason that mid-Miocene sediment was not encountered at DSDP Site 171 until 27 m was drilled is that this Site is located on a saddle between two topographic highs and might be expected to contain a thicker accumulation of sediment derived from nearby slopes.

Discussion

Interpretation of Geophysical Data

High-resolution seismic-reflection data, recently collected by the USGS (Schwab and Bailey, 1985), show that erosional processes acting on the sediment cap of Horizon Guyot are more extensive than originally reported by Lonsdale and others (1972). A chert outcrop (Outcrop B on Fig. 1-4) in the deep-tow survey area can be recognized and followed upslope for 10 km under the pelagic sediment on USGS profile 21 (Fig. 1-5) where it again appears to crop out at a water depth of 1513 m due to erosion of overlying sediment. Interpretation of profile 21 also suggests that erosion of the sediment cap extends upslope to a water depth of at least 1472 m where, through extrapolation, the same chert layer appears to be exposed. Thus, erosion of the summit platform of Horizon Guyot appears to be more extensive than the 1570 to 2000 m isobath-limit recognized by Lonsdale and others (1972). A review of available bottom photographs further supports this interpretation.

Reexamination of the bottom photographs collected by Lonsdale and others (1972) (Fig. 1-3) show that the portion of the summit platform shallower than approximately 1600 m water depth is not "unrippled sea floor" as reported. In all of the bottom photographs, ripples can be identified. However, in water depth less than approximately 1600 m, the ripples are severely degraded by biological activity. Therefore, seismic-reflection profile 21 and bottom photographs indicate that sediment transport and erosion may affect a large portion of the summit platform intermittently but is apparently concentrated around its perimeter.

The erosional scenario presented above does not appear to be limited to Horizon Guyot. Approximately 40 years ago, Hess (1946) noted that the summits of most guyots are very flat except for a beveled, gently sloping shelf around the edge. For example, a seismic-reflection profile run over an unnamed guyot in the north Marshall Islands (Schwab and others, 1986) shows three distinct erosional platforms at the perimeter of the guyot's sediment cap (A, B, and C on Fig. 1-6). Limited bottom photographs show that platform C is covered by long-crested symmetrical ripples indicating active sediment bed load transport (Fig. 1-7). Most of the subhorizontal internal reflectors within the sediment cap on this seismic-reflection profile do not continue beneath the erosional platforms. It is suggested that the erosional process that formed, or is forming, these platforms was active throughout the deposition of the pelagic sediment cap; thus, causing the variation in seismic-reflection signature between the sediment beneath the "undisturbed" sediment cap and the possibly winnowed or eroded sediment below the erosional platforms.

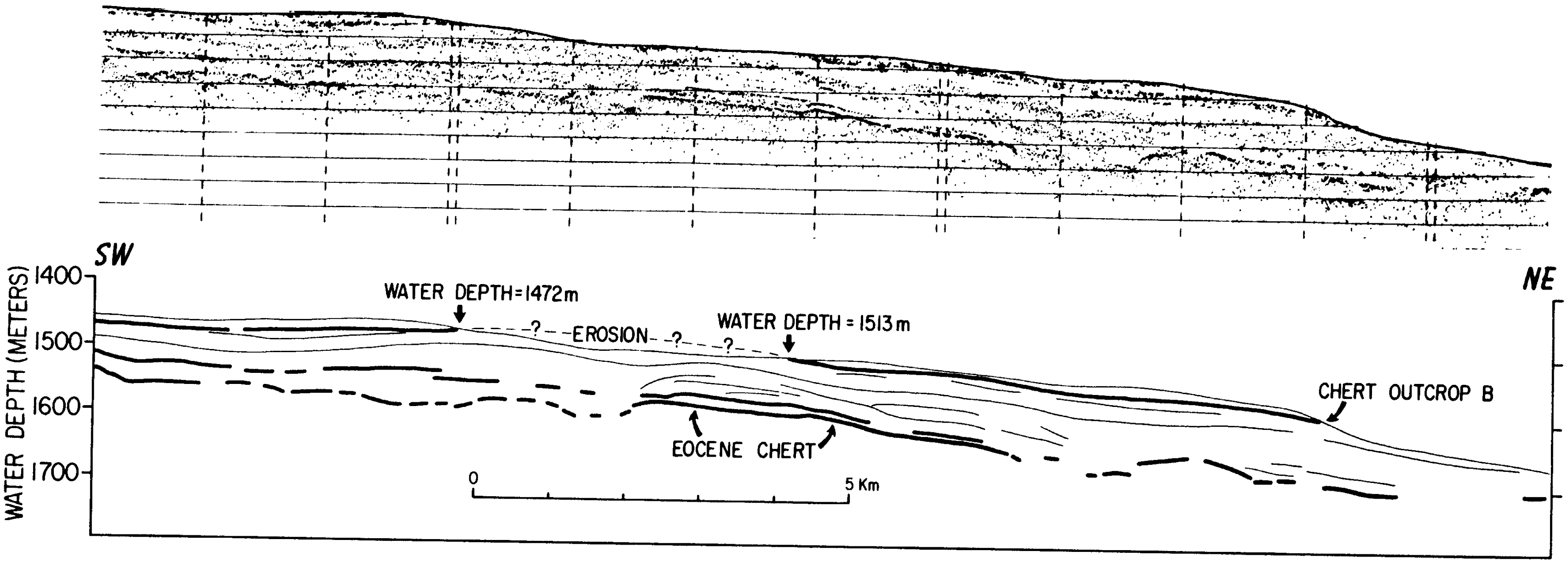

Figure 1-5. 3.5 kHz seismic-reflection profile 21 and interpretive sketch. The location of this profile is shown of Figure 1-2.

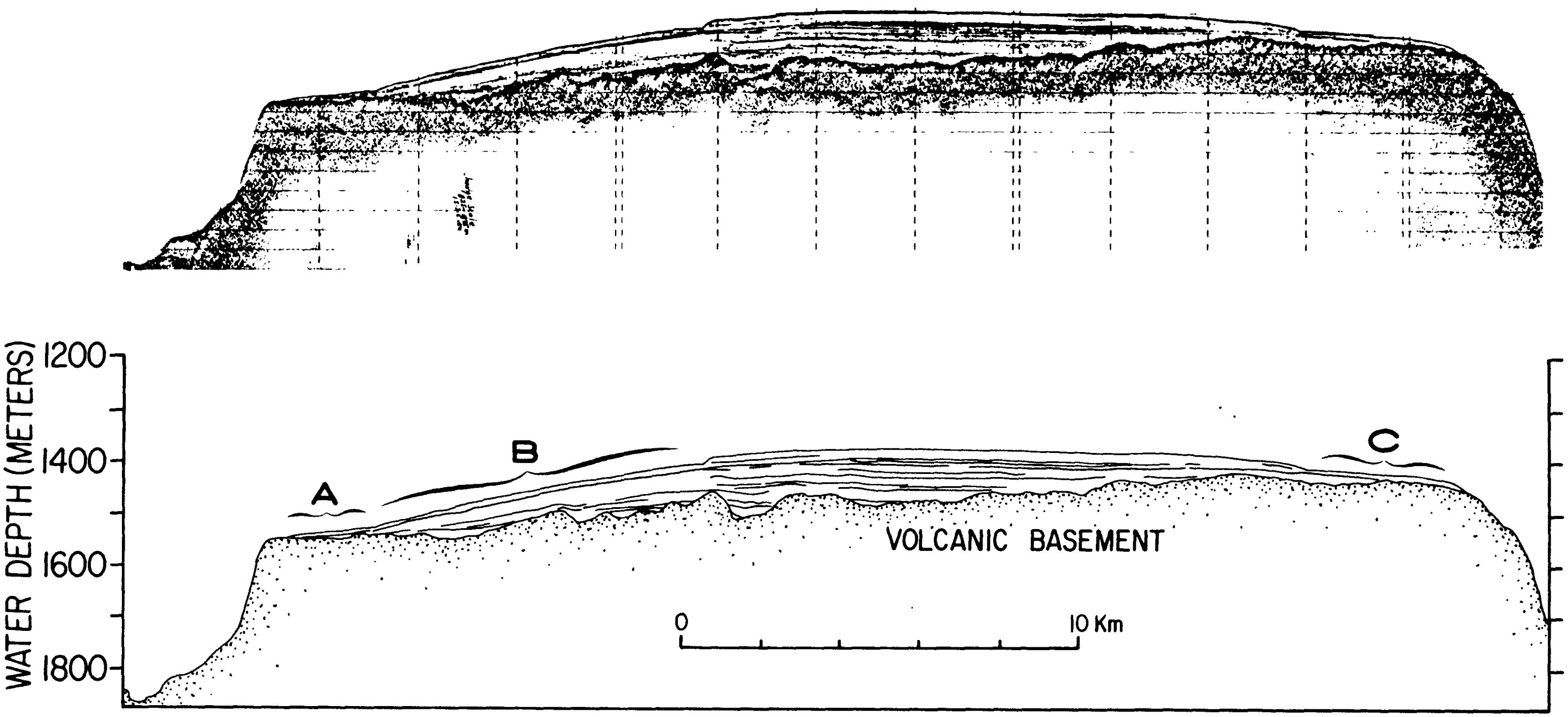

Figure 1-6. 3.5 kHz seismic-reflection profile and interpretive sketch over an unnamed guyot in the northern Marshall Islands (Schwab and others, 1986).

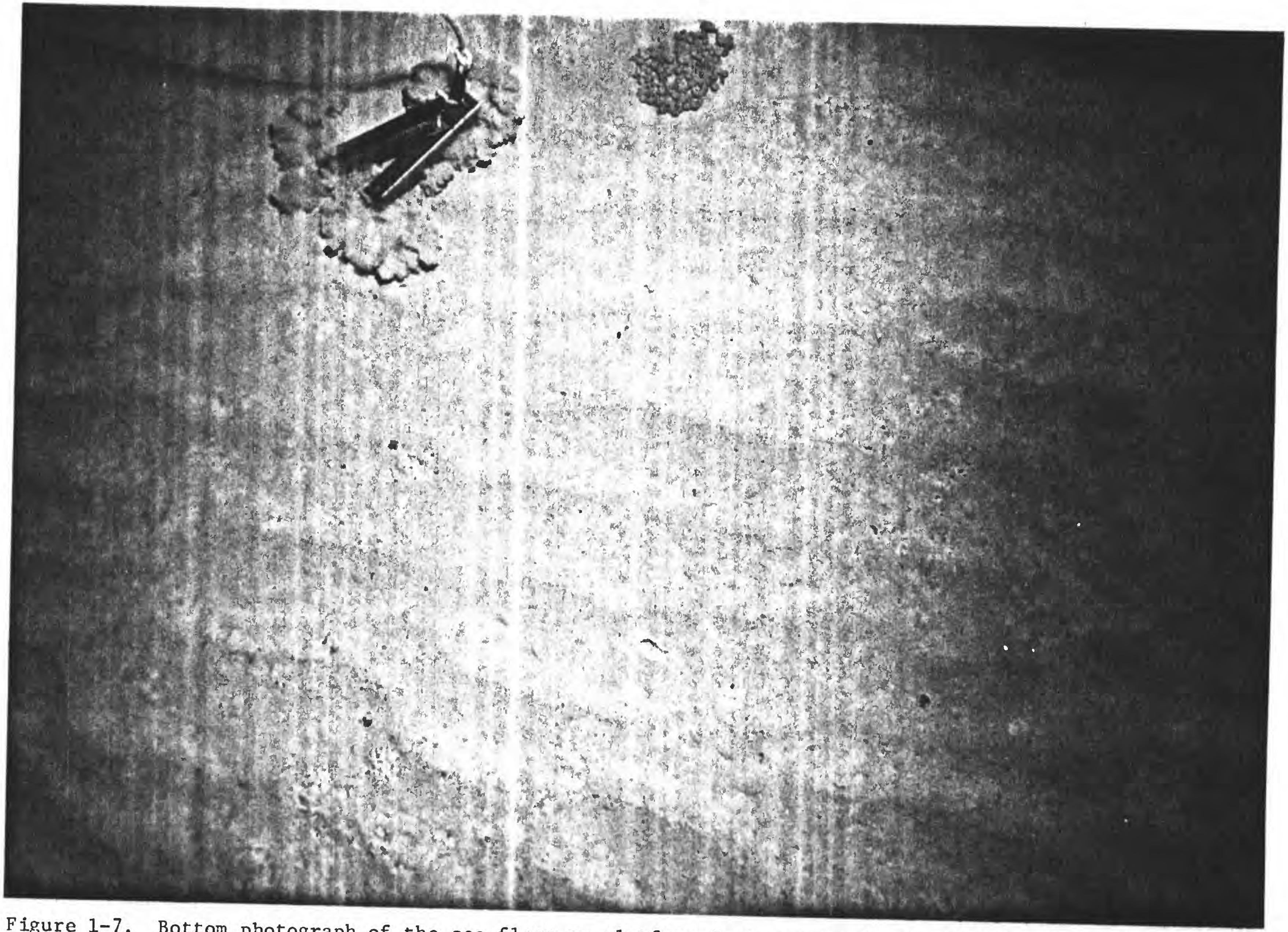

Figure 1-7. Bottom photograph of the sea floor on platform C at a water depth of 1395 m (see Figure 1-6; (Schwab and others, 1985). The trigger weights in the upper left corner are 30 cm long.

MADE FROM BEST AVAILABLE COPY

A group of large linear hummocks near the southern margin of Horizon Guyot's pelagic cap were interpreted from seismic-reflection profiles by Lonsdale and others (1972) to be erosional features also. USGS seismic-reflection profile 20 (Fig. 1-8) shows that similar hummocks on the north perimeter of the pelagic cap are caused by sediment slumping. This mass movement has occurred on an average sea floor declivity of 1.6° and extends from an exhumed hard-rock terrace at a water depth of 1845 m to a water depth of 1458 m. The slumping appears to have affected the sediment to a maximum subbottom depth of approximately 40 m. It is possible that the erosional beveling of the perimeter of the summit platform steepens the sea floor beyond the pelagic sediment's stable slope angle and thus indirectly triggers the observed mass movement. Slope stability analysis of Horizon Guyot sediment is presented in Chapter II.

Analysis Of Sediment Gravity Cores

Textural and micropaleontologic analysis of sediment gravity cores recently collected on Horizon Guyot support the geophysical indication of more extensive sediment transport than was originally suggested by Lonsdale and others (1972). Sediment collected at DSDP Site 44 (Pimm, 1971) is predominantly nannofossil ooze with a sand content (predominantly consisting of foraminifera tests) less than 12%, averaging 3.5%, and shows no evidence of winnowing. Sediment analyses show that the 26-cm-long sediment gravity core 29G, collected in the Deep-Tow area (Fig. 1-2), is composed of a 10-cm-thick layer of sediment with a foram-sand content of 93% composed of mixed Eocene and Quaternary foraminifers that unconformably overlies a sediment layer with a foram-sand content of 56% composed of Eocene foraminfers and a large Pliocene nannofossil component (Lonsdale and others, 1972). It was suggested by Lonsdale and others (1972) that the relatively high sand content of core 29G, as compared to cores collected at DSDP Site 44, is produced by current winnowing; i.e., the Pliocene nannofossil component is removed leaving the foram-sand as a lag deposit.

Following this reasoning, textural analysis of sediment gravity cores collected on Horizon Guyot by the USGS (see Chapter II; Table 2-1 and Appendix 2-1) also indicate winnowing. Above a subsurface depth of 215 cm, the sand content of core GC2 is greater than 35% whereas below 215 cm the sand content drops to less than 10%. Thus, textural analysis of core GC2 indicates that the sedimentary deposit from the sea floor down to a subbottom depth of approximately 240 cm is a winnowed sequence. Similarly, gravity core GC5 indicates that winnowing has affected the sediment down to a maximum subsurface depth of 55 cm, core GC6 down to a minimum subsurface depth of 270 cm and core GC9 down to a minimum subsurface depth of 278 cm.

Nine subsamples from six gravity cores collected on Horizon Guyot by the USGS were qualitatively analyzed for planktonic foraminfers to determine the ages of the sediment and to detect reworking. Eighteen subsamples from the same six gravity cores were qualitatively analyzed for nannofossil biostratigraphy. Foraminifer taxonomy and biostratigraphy follow the work of Postuma (1971), Stainforth and others (1975), and Kennett and Srinivasan (1983) and biostratigraphic zonation is based on Bukry (1973) and Okada and Bukry (1980). Table 1-1 shows the occurrence of planktonic foraminifers in the samples and Table 1-2 shows the nannofossils. Table 1-3 is a comparison of foraminifer and nannofossil ages. For most samples, the planktonic

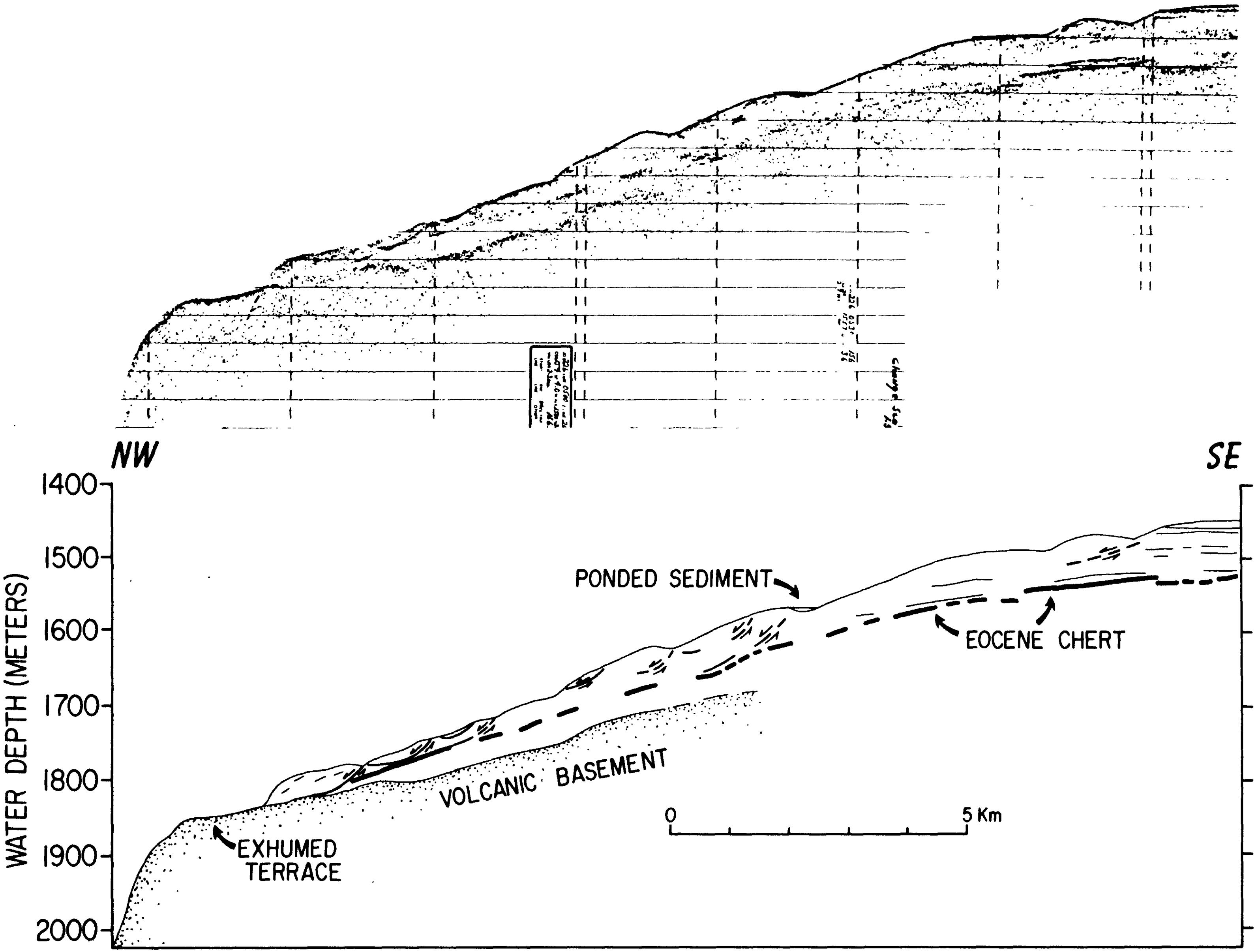

Figure 1-8. 3.5 kHz seismic-reflection profile 20 and interpretive sketch. The location of this profile is shown on Figure 1-2.

TABLE 1-1. DISTRIBUTION OF PLANKTONIC FORAMINIFERS

	Core #	GC2	GC2	GC2	GC3	GC5	GC6	GC8	GC9	GC9
SPECIES	Depth(cm)	70	215	250	196	180	250	280	20	215
Beella digitata						x				
B. praedigitata						x				
Candeina nitida						x				
Cassigerinella chipolensis				x						
Catapsydrax dissimilis								x		
C. stainforthi								x		
Dentoglobigerina altispira altispira			x		x		x			x
D. altispira conica							x			
D. altispira globosa			x		x		x	x		x
Globigerina binaeiensis								x		
G. aff. G. brazieri							x			
G. aff. G. ciperoensis				x						
G. aff. G. collactea			x							
G. sellii				x						
G. aff. G. senni				x						
G. tripartita				x			x	x		
G. aff. G. woodi							x			
Globigerinella aequilateralis							x		x	
G. aff. G. aequilateralis						x				
G. pseudobesa			x							
G. aff. G. pseudobesa								x		
Globigerinita glutinata						x	x	x		
G. uvula							x			
Globigerinoides aff. G. altiapertua								x		
G. aff. G.bollii			x					x		
G. conglobatus		x			x	x			x	
G. aff. G. conglobatus								x	x	
G. extremus		x	x		x	x			x	
G. fistulosis		x				x			x	x
G. immaturus							x			x
G. obliquus			x		x	x				
G. aff. G. parawoodi							x	x		
G. quadrilobatus		x				x		x	x	
G. ruber					x		x		x	x
G. aff. G. ruber		x	x			x				
G. sacculifer		x			x	x			x	
G. cf. G. sicanus							x	x		x
G. subquadratus			x				x	x		x
G. triloba		x	x			x	x	x		x
G. spp.			x							x
Globoquadrina baroemoenensis			x							
G. dehiscens							x			x
G. cf. G. praedehiscens										x
G. venezuelana		x	x	x	x		x		x	x
Globorotalia aragonensis				x						
G. aff. G. birnageae							x			
G. crassiformis					x					

TABLE 1-1. continued.

	Core #	GC2	GC2	GC2	GC3	GC5	GC6	GC8	GC9	GC9
SPECIES	Depth(cm)	70	215	250	196	180	250	280	20	215
G. fohsi fohsi							x			
G. fohsi lobata							x			
G. fohsi praefohsi							x			
G. inflata		x	x			x			x	
G. cf. G. kugleri										x
G. cf. G. multicamerata									x	
G. obesa									x	
G. opima				x						
G. pentacamerata				x						
G. cf. G. peripheroacuta							x			
G. peripheroronda										x
G. cf. G. primitiva				x	x					
G. scitula		x					x		x	x
G. subbotinae		x	x	x	x	x	x			
G. tosaensis		x							x	
G. truncatulinoides						x		x		
G. tumida cf. G.t. flexuosa					x					
G. plesiotumida			x		x					
G. cf. G. plesiotumida		x							x	
G. tumida tumida		x	x	x	x	x	x		x	
G. ungulata									x	
G. spp.			x				x	x	x	
Globorotaloides hexagona		x				x			x	
G. variabilis									x	
Heterohelix sp.?				x						
Neogloboquadrina acostaensis			x							
N. dutertrei		x								
N. cf. N. humerosa		x							x	
Orbulina bilobata									x	
O. suturalis									x	
O. universa					x				x	
O. spp.		x	x				x			
Praeorbulina sp.							x			
Pulleniatina cf. P. obliquiloculata		x								
P. praecursor		x							x	
P. cf. P. praecursor			x			x				
P. primalis										x
P. cf. primalis		x			x				x	
Sphaeroidinella dehiscens		x	x		x	x			x	
Sphaeroidinellopsis paenedehiscens				x			x		x	
S. seminulina			x							
S. aff. S. seminulina							x			

TABLE 1-2. DISTRIBUTION OF CALCAREOUS NANNOPLANKTON

	Core #	GC2	GC2	GC2	GC2	GC3	GC5	GC5	GC5	GC5
SPECIES	Depth(cm)	70	125	215	250	196	13	38	72	150
Amaurolithus delicatus										x
Calcidiscus macintyrei		x				x				
Ceratolithus cristatus and var.		x		x			x	x		
C. rugosus		x	x			x	x	x		
C. spp.		x				x				
Chiasmolithus grandis										
Coccolithus crassus?		x								
C. eopelagicus		x			x					
C. pelagicus (group)		x	x	x	x	x			x	x
Coronocyclus sp.										
Cyclicargolithus abisectus					x					
C. floridanus					x					
Cyclococcolithina aff. C. formosa										x
C. leptopora		x	x	x			x	x		
Cyclolithella pactilis					x					
Dictyococcites bisectus					x			x	x	x
Discoaster asymmetricus		x	x	x	x	x	x	x		x
D. barbadiensis										
D. berggreni			x	x						x
D. braarudii										x
D. brouweri		x	x	x	x	x	x	x	x	
D. deflandrei					x					
D. cf. dilatus								x	x	
D. druggi				x						
D. cf. D. exilis										
D. formosus			x							
D. intercalaris						x	x	x		
D. neohamatus			x							
D. nodifer					x					x
D. obtusus					x				x	
D. pentaradiatus		x	x	x	x	x	x	x		x
D. quinqueramus			x	x						
D. stellulus									x	
D. surculus		x	x	x		x	x	x		
D. tamalis			x	x		x				
D. tani					x					
D. triradiatus		x	x							
D. variabilis		x	x	x		x	x	x		

TABLE 1-2. DISTRIBUTION OF CALCAREOUS
NANNOPLANKTON(continued)

	Core #	GC2	GC2	GC2	GC2	GC3	GC5	GC5	GC5	GC5
SPECIES	Depth(cm)	70	125	215	250	196	13	38	72	150
Discolithina spp.							x			
Emiliania annula		x	x	x						
E. ovata		x	x	x						
Gephyrocapsa spp.										
Hayaster perplexus		x								
Helicosphaera ? intermedia										
H. kamptneri										
H. sellii		x								
H. spp.		x	x		x					x
Orthostylus cf. tribrachiatus								x	x	x
Pontosphaera aff. P. scutellum		x								
Rhabdosphaera spp.			x				x	x		
Scyphosphaera sp.				x		x				
Sphenolithus distentus					x					
S. heteromorphus										
S. moriformis					x				x	
S. predistentus					x					
S. pseudoradians					x					
S. radians					x					
Thoracosphaera sp.							x			
Triquetrorhabdulus carinatus					x					x

TABLE 1-2. DISTRIBUTION OF CALCAREOUS NANNOPLANKTON(continued)

	Core #	GC5	GC6	GC6	GC6	GC6	GC8	GC9	GC9	GC9	GC9
SPECIES	Depth(cm)	180	60	138	218	250	220	20	37	108	215
Amaurolithus delicatus						x					
Calcidiscus macintyrei		x	x	x		x		x	x	x	
Ceratolithus cristatus and var.		x						x			
C. rugosus		x	x	x	x	x		x	x	x	
C. spp.			x	x				x		x	
Chiasmolithus grandis					x						
Coccolithus crassus?											
C. eopelagicus											
C. pelagicus (group)				x	x	x	x	x	x	x	x
Coronocyclus sp.							x				
Cyclicargolithus abisectus		x				x	x				
C. floridanus							x				x
Cyclococcolithina aff. C. formosa											
C. leptopora		x		x	x			x		x	
Cyclolithella pactilis											
Dictyococcites bisectus		x				x	x				x
Discoaster asymmetricus				x	x	x		x	x	x	x
D. barbadiensis						x					
D. berggreni				x						x	
D. braarudii					x						
D. brouweri		x	x	x	x	x		x	x	x	x
D. deflandrei							x				
D. cf. dilatus					x						x
D. druggi		x					x				x
D. cf. D. exilis				x	x	x				x	
D. formosus											
D. intercalaris			x					x		x	x
D. neohamatus											
D. nodifer											
D. obtusus			x			x			x		x
D. pentaradiatus			x	x	x	x		x	x	x	x
D. quinqueramus				x	x			x			
D. stellulus											
D. surculus			x	x	x	x		x	x	x	x
D. tamalis				x	x	x			x	x	x
D. tani		x									
D. triradiatus			x					x	x		
D. variabilis					x	x				x	x

TABLE 1-2. DISTRIBUTION OF CALCAREOUS NANNOPLANKTON(continued)

	Core #	GC5	GC6	GC6	GC6	GC6	GC8	GC9	GC9	GC9	GC9
SPECIES	Depth(cm)	180	60	138	218	250	220	20	37	108	215
Discolithina spp.				x	x				x	x	
Emiliania annula								x	x	x	
E. ovata								x	x		
Gephyrocapsa spp.								x			
Hayaster perplexus					x	x	x	x			x
Helicosphaera ? intermedia					x						
H. kamptneri						x					
H. sellii			x								
H. spp.		x	x	x				x			
Orthostylus cf. tribrachiatus				x		x				x	x
Pontosphaera aff. P. scutellum											
Rhabdosphaera spp.			x	x							
Scyphosphaera sp.					x						
Sphenolithus distentus		x									
S. heteromorphus										x	x
S. moriformis						x					
S. predistentus											
S. pseudoradians											
S. radians											
Thoracosphaera sp.		x						x	x		
Triquetrorhabdulus carinatus							x				

TABLE 1-3. PLANKTONIC FORAMINIFER AND CALCAREOUS NANNOFOSSIL AGES

PLANKTONIC FORAMINIFERS		CALCAREOUS NANNOFOSSILS	
Core number	Age	Core number	Age
GC2-70cm	Late Pliocene(N21)	GC2-70cm	Late Pliocene(CN12cd)
——	——	GC2-125cm	Early-Mid Pliocene(CN11b-12a)
GC2-215cm	Early Pliocene(N19)	GC2-215cm	Early-Mid Pliocene(CN11b-12a)
GC2-250cm	Late Oligocene	GC2-250cm	Late Oligocene(CP18)
GC3-196cm	Early Pliocene(N19)	GC3-196	Pliocene
——	——	GC5-13cm	Pliocene
——	——	GC5-38cm	Pliocene
——	——	GC5-72cm	Late Oligocene-Middle Miocene
——	——	GC5-150cm	Late Mioc.(dominant) with E. Plioc;
GC5-180cm	Late Plioc.-E. Pleist	GC5-180cm	Quaternary with reworked Olig.
——	——	GC6-60cm	Late Pliocene(CN12d)
——	——	GC6-138cm	Pliocene
——	——	GC6-218cm	Pliocene
GC6-250cm	Mid Miocene	GC6-250cm	Pliocene
——	——	GC8-220cm	Early Miocene(CN1c)
GC8-280cm	Early Miocene(N5-6)	——	——
GC9-20cm	Late Pliocene(N21)	GC9-20cm	Pliocene
——	——	GC9-37cm	Pliocene
——	——	GC9-108cm	Pliocene
GC9-215cm	Early-Mid Miocene	GC9-215cm	Mid Miocene(CN4)

foraminifera and nannofossil ages are in agreement; however, some age determinations are questionable due to mixing of fossils of different ages.

Micropaleontologic analysis of the USGS sediment gravity cores suggests that the fine-grain sediment encountered in the deeper section of core GC2 and middle section of core GC5 is late Oligocene in age. Sandy sediment collected above these fine-grain sediments and in cores GC3, GC5, GC6, GC8, and GC9 (Fig. 1-2) ranges in age from early Miocene to late Pliocene or early Pleistocene. Six of the samples contain reworked Eocene foraminfers estimated to range from less than 1% to approximately 12% of the planktonic fauna. Miocene and Pliocene reworking was detected in four samples along with minor amounts of downworking due to bioturbation or from coring contamination. Calcareous nannofossils are abundant, diverse, and well-preserved in the Horizon Guyot samples. As with the planktonic foraminifers, there is some reworking and downworking, but it is minor in most samples. A more detailed description of the micropaleontological analysis of the USGS gravity cores is presented in Appendix 1-1.

The USGS gravity cores penetrated sediment as old as Oligocene at a subsurface depth of only 250 cm. Active erosion on the pelagic sediment cap of Horizon Guyot, where these cores were collected, would tend to limit sediment accumulation in this area. Therefore, it is not surprising to find pre-Quaternary sediment at 2.5 m below the sea floor. The common occurrence of reworked Eocene planktonic foraminifers and the possible unconformable contact between Oligocene and Pliocene sediment in cores GC2 and GC5 suggests that erosion and redistribution of sediment on the pelagic cap of Horizon Guyot has been a common occurrence during the Tertiary.

Several samples contain fossils of mixed ages; some are younger and some are older than our assigned ages. We have based our age determinations on the majority assemblages present. We attribute the presence of minor occurrences of older fossils to reworking, and the presence of younger fossils to downworking resulting from bioturbation and mixing within cores during sampling. There is a remote possibility that the minor assemblages should be used for age determinations; however, these fossils make up a very small percentage of the total assemblage, so reworking of this magnitude would be difficult to explain. Table 1-3 gives further evidence that our age determinations are valid. If mixing of fossils were widespread enough to cause erroneous determinations, it is doubtful that there would be the consistent progression in all cores (except for GC5) of older material downcore for both foraminifers and nannofossils. Instead, we might expect to see an almost homogenous distribution of ages throughout the cores.

The anomalously young age (Quaternary) of sediment from the lowest sample from core GC5 (subsurface depth = 180 cm, see Appendix 1-1) suggests that this core was taken in slumped material or that the core barrel entered the sediment twice. If core GC5 represents a slump deposit, mass movement may be more extensive on Horizon Guyot's pelagic sediment cap than just the slumps described on seismic-reflection profile 20 (Fig. 1-8).

Conclusions

Analysis of high-resolution seismic-reflection profiles, textural and micropaleontologic analysis of sediment gravity cores, and the previous investigation of Lonsdale and others (1972) show that erosion and redistribution of sediment are important processes affecting the sediment cap of Horizon Guyot. Although these processes may periodically affect the entire sediment cap, they are apparently concentrated around its perimeter. The erosional beveling of the perimeter of the pelagic cap creates a sea floor with a 1.5° to 4° average declivity. This erosional beveling appears to have oversteepened the sea floor and caused slumping of the pelagic sediment in at least one area on the northern perimeter. This combination of current activity and sediment mass movement may be an important mechanism for removal of sediment from the summit of Horizon Guyot, down the guyot flanks, to the abyssal floor.

APPENDIX 1-1: PALEONTOLOGIC ANALYSIS

Core GC2

Subsurface Depth = 70 cm

A late Pliocene age (N21) is assigned to this subsample based on the presence of: *Globigerinoides fistulosis* and *Globorotalia tosaensis* (late Pliocene N21 to early Pleistocene N22); *Globerinoides extremus* (late Miocene N16 to late Pliocene N21); *Globorotalia inflata* (late Pliocene to Holocene); *Pulleniatina praecursor* (Pliocene N19-N21); *Ceratolithus rugosus* (restricts age to the Pliocene); *Emiliania annula* and *E. ovata* (middle Pliocene CN116 to late Pleistocene CN14a); and *Discoaster triradiatus* (known to be abundant in the late Pliocene). Longer ranging species that are abundant include: *Sphaeroidinella dehiscens* (early Pliocene to Holocene); *Globorotalia tumida tumida* (late Miocene to Holocene); *Globigerinoides conglobatus* (late Miocene to Holocene); and discoasters known to be extinct at the end of the Pliocene. Reworked Eocene foraminifers (mostly *Morozovella subbotinae*) make up approximately 2% of the planktonic assemblage, reworked late Miocene to early Pliocene foraminifers make up about 4%, and reworked Miocene discoasters are present.

Subsurface Depth = 125 cm

Foraminifers were not analyzed in this sample. Nannofossil species present indicate an early to middle Pliocene age. The common occurrence of *Discoaster tamalis* allows assignment to Zones CN11a-CN12a.

Subsurface Depth = 215 cm

An early Pliocene age (N19) is assigned to this subsample based on the presence of: *Globoquadrina venezuelana* (middle Oligocene to early Pliocene); *Dentoglobigerina altispira globosa* (late Oligocene P22 to early Pliocene N19); *Globigerinella pseudobesa* (middle Miocene N13 to early Pliocene N19); *Neogloboquadrina acostaensis* (late Miocene N16 to early Pliocene N20); *Globorotalia plesiotumida* (late Miocene N17A to early Pliocene N19); and *Pulleniatina* cf. *P. praecursor* (Pliocene N19-N21). The nannofossil assemblage suggests a early to middle Pliocene age (CN11b-12a) based on the presence of *Discoaster tamalis*. Approximately 12% of the fauna is composed of reworked Eocene species including *Morozovella subbotinae* and *Truncorotaloides* aff. *T. collactea*. Minor Miocene reworking is also evident.

Subsurface depth of 250 cm

A late Oligocene age is assigned to this subsample due to the presence of: *Cassigerinella chipolensis* (early Oligocene to Miocene); *Globigerina tripartita* (late Oligocene to early Miocene); *Globigerina* aff. *G. ciperoensis* (late Oligocene to early Miocene); *Globigerina sellii* (Oligocene); *Globorotalia opima* (late Oligocene); and nannofossils typical of the late Oligocene *Sphenolithus distentus* zone (CP18) including *Coccolithus eopelagicus*, *Cyclicargolithus abisectus*, *C. floridanus*, *Dictyococcites bisectus*, Discoaster *deflandrei*, *D. nodifer*, *D. tani*, *Sphenolithus distentus*, *S. predistentus*, and *Triquetrorhabdulus* aff. *T. carinatus*. Approximately 5% of the assemblage is reworked Eocene planktonic foraminifers including: *Morozovella aragonensis*; *Acarinina*. *pentacamerata*; *A.* cf. *A. primitiva*; and *Morozovella*. *subbotinae*. Minor Eocene reworking is also evident in the nannofossil component. Late Miocene to Recent downworked foraminifers make up less than 1% of the fauna and minor Miocene and Pliocene nannofossil downworking is evident.

Core GC3
Subsurface Depth = 196 to 199 cm

An early Pliocene (N19) age is assigned to this subsample based on the presence of: *Globoquadrina venezuelana* (middle Oligocene to early Pliocene); *Neogloboquadrina altispira globosa* (late Oligocene P22 to early Pliocene N19); *Globorotalia plesiotumida* (late Miocene N17A to early Pliocene N19); *Pulleniatina* cf. *P. primalis* (late Miocene N17B to N20); *Sphaeroidinella dehiscens* and *Globorotalia crassiformis* (early Pliocene N19 to Holocene); *Discoaster asymmetricus*, *D. brouweri*, and *D.* surculus (late Miocene to late Pliocene); and *Discoaster tamalis* (few) and *Ceratolithus rugosus* (Pliocene). Approximately 5% of the fauna is composed of reworked Paleocene (?) to Eocene *Acarinina* aff. *A. primitiva* and *Morozovella subbotinae*.

Core GC5
Subsurface Depth = 13 cm

Foraminifers were not analyzed in this subsample. Delicate discoasters typical of late Miocene to late Pliocene are abundant. These species and the presence of *Ceratolithus rugosus* (Pliocene) indicate a Pliocene age.

Subsurface Depth = 38 cm

This subsample contains a flora similar to that described at a subsurface depth of 13 cm, but there are fewer delicate discoasters and more robust discoasters present; this subsample is probably also of Pliocene age. Foraminifers were not analyzed.

Subsurface Depth = 72 cm

Unlike the above two subsamples, delicate discoasters are absent. The nannofossil assemblage is composed of more massive (probably overgrown) discoasters. Ceratoliths are absent. A late Oligocene to middle Miocene age is tentatively assigned to this subsample. Again, foraminifers were not analyzed.

Subsurface Depth = 150 cm

The assemblage of this subsample is a mixture of massive and delicate discoasters. Other nannofossils present range from Eocene to Pliocene, with pre-Upper Miocene species seeming to dominate. Foraminifers were not analyzed.

Subsurface Depth = 180 cm

The age of this deepest sample from core GC5 is anomalous. It appears to be younger than those samples situated above it. The foraminifers are a mixture of late Pliocene and early Pleistocene species including: *Globigerinoides triloba* (early Miocene N4B to Pleistocene N22); *Globigerinoides obliquus* (early Miocene N5 to Pleistocene N22); *Beella* *praedigitata* and *Globigerinoides extremus* (late Miocene N16 to late Pliocene N21); *Globigerinoides fistulosis* (late Pliocene N21 to early Pleistocene N22); *Pulleniatina* cf. *P. praecursor* (Pliocene N21); and *Beella digitata* and *Globorotalia truncatulinoides* (Pleistocene N22 to Holocene). Only a trace of Eocene reworking is observed. There are few discoasters, and those present are of mixed ages. The presence of ceratoliths without discoasters (except for a few reworked ones) supports a Quaternary age. However, other species indicate an Oligocene age.

Core GC6

Subsurface Depth = 60 cm

A late Pliocene age (CN12d) is assigned to this sample base on the presence of: *Ceratolithus cristatus*; *C. rugosus*; *Helicosphaera sellii*; *Discoaster brouweri*; *D. triradiatus*; and *Calcidiscus macintyrei*. Foraminifers were not analyzed.

Subsurface Depths = 138 cm and 218 cm

The co-occurrence of *Ceratolithus rugosus* and discoasters typical of the late Miocene to late Pliocene indicate a Pliocene age for these samples. The presence of *Discoaster tamalis* in these samples brackets the age between CN12a and CN11b.

Subsurface Depth = 250 cm

A middle Miocene age is assigned to this sample based on the presence of the following foraminiferal species: *Globigerinoides subquadratus* (early Miocene N4B to middle Miocene N15); *Globigerinoides* cf. *G. sicanus* (early Miocene N8 to middle Miocene N9); *Globorotalia scitula* (middle Miocene N9 to recent); *Globorotalia* cf. *G. peripheroacuta* (middle Miocene N10 to N11); and *Globorotalia fohsi fohsi* and *G. fohsi lobata* (middle Miocene N12). There is a discrepancy between the foraminifer and nannofossil ages. Nannofossils suggest the same age (Pliocene) as the foraminifers at subsurface depths of 138 and 218 cm; however, there are older nannofossils present at 250 cm. There is less than 1% late Miocene to recent downworking, 2 to 4% early Miocene reworking and a trace of Eocene reworking in the foraminiferal component.

Core GC8

Subsurface Depth = 220 to 223 cm

The presence of the following species indicates an early Miocene (CN1c) age: *Cyclicargolithus abisectus*; *C. floridanus*; *Discoaster deflandrei*; *D. druggii*; *Hayaster perplexus*; *Sphenolithus dissimilis*; and *Triquetrorhabdulus carinatus*.

Subsurface Depth = 280 cm

The following species support an early Miocene (N5 to N6) age: *Catapsydrax dissimilis* (late Eocene P13 to early Miocene N6); *Globigerina tripartita* (late Oligocene to early Miocene); *Globigerina binaiensis* (late Oligocene P22 to early Miocene N5); *Catapsydrax stainforthi* (early Miocene N4B-N7); *Globigerinoides subquadratus* (early Miocene N4B to middle Miocene N15); and *Globigerinoides triloba* (early Miocene N4B to Pleistocene N22). A minor amount of late Miocene to recent reworking is present. Nannofossils were not analyzed.

Core GC9

Subsurface Depth = 20 cm

A late Pliocene age (N21) is indicated for this sample by the following species: *Globigerinoides extremus* (late Miocene N16 to late Pliocene N21); *Globorotalia* cf. *G. multicamerata* (late Miocene N17B to late Pliocene N21); *Globorotalia inflata* (late Pliocene to Holocene); *Pulleniatina praecursor* (Pliocene N19 to N21); *Globorotalia ungulata* (late Pliocene N21 to Holocene); *Globigerinoides fistulosis* and *G. tosaensis* (late Pliocene N21 to early Pleistocene N22); delicate late Miocene to late Pliocene discoasters; and *Ceratolithus cristatus* and *C. rugosus* (Pliocene). A few specimens of *Sphenolithus heteromorphus* suggest minor reworking of lower or middle Miocene sediment. Also, 1 to 3% of the fauna is composed of reworked Miocene and early Pliocene foraminifers.

Subsurface Depth = 37 and 108 cm

The nannofossil assemblage for these samples indicates the same age as reported for subsurface depth = 20 cm. Foraminifers were not analyzed.

Subsurface Depth = 215 cm

An early to middle Miocene age is assigned to this sample based on the presence of the following species: *Globoquadrina* cf. *G. praedehiscens* (late Oligocene P22 to early Miocene N6); *Globoquadrina dehiscens* (early to late Miocene); *Globigerinoides triloba* (early Miocene N4B to Pleistocene N22); *Dentoglobigerina altispira altispira* (early Miocene N4B to late Pliocene N21); *Globigerinoides immaturus* (early Miocene N5 to Holocene); *Globigerinoides subquadratus* (early Miocene N4B to middle Miocene N15); *Globorotalia peripheroronda* (early Miocene N4B to middle Miocene N10); and *Globigerinoides sicanus* (early Miocene N8 to middle Miocene N9). There is less than 5% Pliocene downworking. The nannofossil assemblage contains approximately 95% middle Miocene (CN4) nannofossils, 4% Pliocene discoasters and less than 1% early Miocene discoasters (Bukry, personal communication). Abundant *Sphenolithus heteromorphus* with *Cyclicargolithus floridanus* and *Calcidiscus macintyrei* indicate a middle Miocene (CN4) age for the sample. The sparse occurrence of *Discoaster asymmetricus*, *D. pentaradiatus*, and *D. tamalis* indicate mid-Pliocene mixing.

II. GEOTECHNICAL ANALYSIS AND PHYSICAL PROPERTIES OF SEDIMENT FROM HORIZON GUYOT

by

Robert E. Kayen, Homa J. Lee, and William C. Schwab

Introduction

A suite of geotechnical and index property tests was performed on sediment samples from sediment gravity cores collected on the summit of Horizon Guyot in order to classify the sediment, evaluate slope stability, and analyze the consolidation state. The core locations are shown in Chapter I, Figure 1-2. Included in this suite were seven static triaxial compression, four cyclic triaxial compression, and nine consolidation tests. In addition, water content, grain density, bulk density, grain size, and vane shear tests were run. Analyses of these test results through a normalized parameter framework produce an estimate of the in-place undrained shear strength under both static and cyclic loading conditions.

Purpose And Framework Of The Analysis

The critical geotechnical parameter derived in the geotechnical testing program is the undrained shear strength, that is, the strength that is mobilized in a short period of time with no pore water drainage. Submarine slope failure typically follows a mobilization of the undrained shear strength during short term wave, static, or earthquake loading (Sangrey, 1977). Because sampling, transportation, and laboratory preparation of the core sections alter engineering behavior, much of the geotechnical testing was directed towards eliminating the effects of disturbance. The test framework used was the normalized strength parameter (NSP) approach (Ladd and Foott, 1974). The principal assumption of the NSP approach is that sediment behavior primarily depends on three factors: (1) the general sediment properties (grain size, mineralogy, etc.), (2) the stress state (overburden pressure), and (3) the overconsolidation ratio (greatest effective stress that the sediment has experienced divided by the present effective overburden stress). The overconsolidation ratio (OCR) and the maximum past stress of the sampled material were estimated using the Casagrande (1936) procedure and the results of one-dimensional consolidation tests conducted under a constant rate of strain loading (Wissa and others, 1971). Relations between stress state, OCR, and undrained shear strength were established through triaxial compression testing. The following sections present the index properties and triaxial test results. Finally, these results are applied to an analysis of the general slope stability of the sediment cap of Horizon Guyot.

Index Property Measurements

Calcium Carbonate Content

Samples taken from the sediment cap of Horizon Guyot consist almost entirely of 10 YR 7/4 and 10 YR 8/2 (Goddard, 1970) biogenous calcium carbonate. Discoasters, other nannoplankton, and foraminifers comprise the majority of the sediment in the cores sampled (see Chapter I). Calcium carbonate contents (Table 2-1) range from 88.4% to 95.6%, as determined from a Coulometrics carbonate determinator connected to an acid digestor and an induction furnace, and classify the Horizon Guyot sediment as calcareous ooze (Sverdrup and others, 1942, p. 972).

TABLE 2-1

Test Log, Index Properties, and Shear Strength

Cruise	Core	Depth	Test*	w	ρ	Grain Size			$CaCO_3$	Vane Shear	G_s
		(cm)		(%)	(g/cc)	Sand(%)	Silt(%)	Clay(%)	(%)	Strength (kPa)	
L5-83-HW	GC2	72	VS	88.0						3.3	
L5-83-HW	GC2	174	VS	89.0						3.3	
L5-83-HW	GC2	274	VS	93.8						1.6	
L5-83-HW	GC2	303	CE144	84.3	1.54						
L5-83-HW	GC3	103	CE145	82.5	1.55						
L5-83-HW	GC3	119	VS	64.0						0.4	
L5-83-HW	GC4	36	VS	104.0						1.8	
L5-83-HW	GC4	133	VS	87.0						4.8	
L9-84-CP	GC2	30							94.3		
L9-84-CP	GC2	70	VS	81.5	1.53	46.63	40.71	12.66		12.2	2.72
L9-84-CP	GC2	80	VS	75.0		52.19	37.10	10.71		8.0	
L9-84-CP	GC2	90		86.6		52.46	39.01	8.53			
L9-84-CP	GC2	105	VS	104.4		42.63	44.36	13.01		23.9	
L9-84-CP	GC2	125	VS	96.0		41.70	40.83	17.48	88.4	16.1	
L9-84-CP	GC2	140	VS	71.4		39.52	46.84	13.64	92.4	18.1	
L9-84-CP	GC2	160	VS	98.8		35.33	49.85	14.83		20.2	
L9-84-CP	GC2	175		79.3					95.6		
L9-84-CP	GC2	195	VS	86.9		35.12	49.05	15.83		22.2	
L9-84-CP	GC2	205							92.5		
L9-84-CP	GC2	215	VS	81.5		6.37	70.18	23.46		21.4	
L9-84-CP	GC2	240	VS	57.6		5.46	63.44	31.15	95.2	12.4	
L9-84-CP	GC2	250	VS	65.2		5.77	80.48	13.75		14.8	
L9-84-CP	GC3	26		103.1							
L9-84-CP	GC3	111		91.0							
L9-84-CP	GC3	196				35.97	54.79	9.24			
L9-84-CP	GC4	16		90.1							
L9-84-CP	GC4	101		77.0							
L9-84-CP	GC4	115	TH9	75.3	1.61	38.03	57.03	4.94			
L9-84-CP	GC4	123	CE179	87.1	1.57	39.46	46.08	14.46			

TABLE 2-1 (cont.)

Cruise	Core	Depth (cm)	Test*	w (%)	ρ (g/cc)	Grain Size Sand(%)	Silt(%)	Clay(%)	$CaCO_3$ (%)	Vane Shear Strength (kPa)	G_s
L9-84-CP	GC5	13	VS	79.1	1.55	41.61	40.74	17.65		7.4	2.77
L9-84-CP	GC5	38	VS	91.9		23.49	52.39	24.12		6.6	
L9-84-CP	GC5	55	VS	76.0	1.56	7.92	40.51	51.58		9.5	2.73
L9-84-CP	GC5	72	VS	75.7		6.77	34.99	58.25		7.4	
L9-84-CP	GC5	98	VS	87.5		10.98	30.99	58.03		2.1	
L9-84-CP	GC5	121	VS	90.6		9.00	33.38	57.62		4.9	
L9-84-CP	GC5	150	VS	71.6		18.83	46.78	40.38		2.9	
L9-84-CP	GC5	165	VS	94.4	1.49	63.79	23.43	12.78		9.5	2.75
L9-84-CP	GC5	180	VS	93.4		45.19	26.74	28.07		7.4	
L9-84-CP	GC6	0		102.7							
L9-84-CP	GC6	12		91.4	1.50	81.48	7.89	10.62			2.77
L9-84-CP	GC6	20	VS	93.8		42.01	32.77	25.22		4.9	
L9-84-CP	GC6	34		62.4							
L9-84-CP	GC6	60	VS	70.8		40.85	50.93	8.22		17.7	
L9-84-CP	GC6	80	VS	81.1		35.32	29.47	35.20		23.1	
L9-84-CP	GC6	100	VS	87.9		36.55	51.54	11.91		18.9	
L9-84-CP	GC6	118		77.1							
L9-84-CP	GC6	138	VS	112.9		35.28	41.94	22.78		20.6	
L9-84-CP	GC6	164	VS	82.0		30.61	30.92	38.47		23.9	
L9-84-CP	GC6	191	VS	52.0		32.91	53.91	13.08		19.4	
L9-84-CP	GC6	202		75.2							
L9-84-CP	GC6	218	VS	72.7	1.59	33.48	50.80	15.72		18.1	2.80
L9-84-CP	GC6	250	VS	78.7	1.55	35.00	46.23	18.77		25.5	2.75
L9-84-CP	GC6	270	VS	90.0	1.49	43.01	27.81	29.18		19.4	2.69
L9-84-CP	GC7	0		74.7		52.40	29.63	17.97			
L9-84-CP	GC7	38		90.1							
L9-84-CP	GC7	95	CE177	93.8	1.49	44.72	24.88	30.40			
L9-84-CP	GC7	119		80.6							
L9-84-CP	GC7	170	CE178	93.3	1.49	45.50	33.50	21.00			
L9-84-CP	GC7	203		80.5							
L9-84-CP	GC7	260	CE181	70.0	1.58	33.92	31.94	34.14			

TABLE 2-1 (cont.)

Cruise	Core	Depth (cm)	Test*	w (%)	ρ (g/cc)	Grain Size Sand(%)	Grain Size Silt(%)	Grain Size Clay(%)	$CaCO_3$ (%)	Vane Shear Strength (kPa)	G_s
L9-84-CP	GC7	265	TH11	75.9	1.64	39.73	31.61	28.66			
L9-84-CP	GC7	275	TE280	65.8	1.76						
L9-84-CP	GC8	0		95.4							
L9-84-CP	GC8	70	D221	78.9	1.52	39.87	46.31	14.00			
L9-84-CP	GC8	80	D220	81.4	1.64	41.03	50.75	8.21			
L9-84-CP	GC8	90	D216	81.2	1.87	33.05	46.84	20.09			
L9-84-CP	GC8	100	TH6	83.9	1.60	33.70	51.84	10.46			
L9-84-CP	GC8	110	TH7	83.6	1.46						
L9-84-CP	GC8	120	CE175	76.8	1.56						
L9-84-CP	GC8	125	TH8	88.9	1.63	37.94	51.14	10.92			
L9-84-CP	GC8	133	D217	85.5	2.07	38.55	50.31	10.94			
L9-84-CP	GC8	156	CE180	78.2	1.56	27.58	52.51	19.90			
L9-84-CP	GC8	195	TH10	77.2	1.77	28.08	44.31	27.61			
L9-84-CP	GC8	200	CE176	78.7	1.56						
L9-84-CP	GC9	20	VS	72.1		33.23	45.5	21.25		17.3	
L9-84-CP	GC9	37	VS	78.1		54.45	40.21	5.34		28.0	
L9-84-CP	GC9	65	VS	103.7		41.13	24.97	33.90		10.7	
L9-84-CP	GC9	85	VS	91.0		37.05	48.80	14.16		13.2	
L9-84-CP	GC9	108	VS	78.9	1.54	36.45	21.41	42.14		15.6	2.67
L9-84-CP	GC9	118		69.4							
L9-84-CP	GC9	140	VS	84.0		24.23	61.68	14.09		10.3	
L9-84-CP	GC9	165	VS	92.1		22.67	26.05	51.28		15.6	
L9-84-CP	GC9	190	VS	80.3		24.62	26.47	48.91		8.2	
L9-84-CP	GC9	201		81.3							
L9-84-CP	GC9	215	VS	86.3		22.25	52.96	24.79		15.6	
L9-84-CP	GC9	235	VS	78.9		26.16	35.48	38.36		27.2	
L9-84-CP	GC9	255	VS	73.6	1.58	24.87	45.70	29.43		32.1	2.69
L9-84-CP	GC9	278	VS	81.4		30.76	45.60	23.64		13.2	

*CE - Consolidation Test
TE - Static Triaxial Test (low confining pressure)
TH - Static Triaxial Test (high confining pressure)
D - Cyclic Triaxial Test
VS - Vane Shear Test

Discoasters, an abundant calcareous nannofossil with fragile radiating spicules (rays), were used to determine the relative amount of grain crushing that had taken place during the consolidation and triaxial tests. The ratios of unbroken discoaster tests to broken ones, before and after all testing were recorded from smear slides. Approximately equal ratios indicate that no noticeable grain crushing had occured. This qualitative technique was also applied to foraminifera tests, with similar conclusions.

Water Content

Water content, w, was determined at many locations within the cores (Table 2-1) using drying and weighing technique (ASTM 1983 standard D2216-80). A correction was made to the weights to account for dried salt assuming a salinity of 35 parts per thousand. Water contents were calculated:

$$w = [1.035\ W_w]/[W_s-(0.035\ W_w)] \quad (1)$$

where W_w is the weight of water and W_s is the weight of dried sediment and salt. Note that water content values are related to dry sediment weight and therefore can be greater than 100%.

The water content of Horizon Guyot sediment varied between 52.0 and 112.9 percent (Table 2-1). There was no consistent correlation between water content and depth in the cores (Table 2-1 and APPENDIX 1).

Bulk Density and Grain Specific Gravity

Bulk density, ρ was determined from the known weights and volumes of both consolidation and triaxial test samples. These measured bulk densities ranged between 1.46 g/cc and 2.07 g/cc (Table 2-1). Grain densities, G_s, determined with a Beckman air comparison pycnometer vary between 2.67 and 2.80, averaging 2.73. Winters and Lee (1982) report similar grain specific gravities between 2.56 and 2.90 with an average of 2.73 for calcareous ooze sampled on the southwest slope off Oahu, Hawaii. Pure calcite has a grain specific gravity of 2.72.

Grain Size Distribution

Grain size analysis were determined from a wet sieve and coulter counter analysis following the procedures of Carver (1971). Using the Udden-Wentworth size classification (Blatt and others, 1972, p. 46) most of the Horizon Guyot sediment is either a sandy clayey silt or a silty clayey sand (Appendix 2-2). Grain size data are presented in Table 2-1, Appendix 2-1 and Appendix 2-2.

Consolidation Properties

Maximum Past Stress and Primary Compression Index

Knowledge of the maximum past stress, σ_{vm}', that has been imparted on the sediment is required in order to perform triaxial compression testing within the framework of the NSP approach. Nine consolidation tests were performed within a triaxial cell using a constant rate of strain loading technique outlined by Wissa and others (1971). In preparation for this procedure a thin wafer of sediment was confined within a cylindrical ring and placed at the base of a triaxial cell. After the triaxial cell was filled with deaired water and an elevated saturation pressure was applied, the sediment was then uniaxially loaded at a constant rate of compressive strain. Pore water pressure, axial deformation, and axial load were continually monitored and automatically logged at predetermined intervals during this procedure.

From the consolidation test data, the void ratio (volume of the void space/volume of the solids) was plotted versus the log of the vertical effective stress, e.g., Fig. 2-1. In fine-grained sediment, the right side of the curve typically defines a straight line, called the "virgin curve", whose slope is the compression index. The compression index, C_c, indicates the amount of void ratio change for a tenfold increase in vertical stress beyond σ_{vm}'.

The maximum past stress can be derived by extrapolating the virgin curve to higher void ratios and employing the Casagrande (1936) graphical construction (Lambe, 1951). Exceedingly high maximum past stresses were found in every core sample from Horizon Guyot. By dividing σ_{vm}' by the in-place overburden stress, σ_{vo}', the OCR is derived. An OCR of 1.0 is indicative of normally consolidated sediment whereas an OCR greater than 1.0 indicates that the sediment is overconsolidated. Overconsolidation of sediment is caused by, among other reasons, overburden erosion, cementation, and reworking by currents. Overconsolidation ratios obtained from consolidation tests conducted on Horizon Guyot sediment range from 32 to 57 (Table 2-2). Consolidation test plots are presented in Appendix 2-3.

Strength Properties

Estimation Of The In-Place Undrained Shear Strength

Vane shear testing (ASTM, 1982 standard D 2573-72) was performed on split stratigraphic core sections. A small four-bladed vane, 1.27 cm high by 1.27 cm diameter, was inserted perpendicular to the split core surface so that the top of the vane was at least 1 cm beneath the surface. The vane was rotated through a motorized torque cell at a rate of 90°/min. Peak torque was measured and used to calculate the undrained shear strength. Vane shear strength data are presented in Table 2-1 and Appendix 2-1.

The in-place static and cyclic undrained shear strengths, S_{us} and S_{ur} respectively, determined through triaxial testing were estimated using the NSP approach. During the consolidation phase of the triaxial tests, isotropic consolidaton stresses were elevated to levels approximately four times the maximum past stress. This high confining stress partly removes the complications of sample disturbance and thereby allows a more accurate analysis of field conditions (Ladd and Foott, 1974). If certain sediment parameters can be assumed constant within and below a sediment core, a useful methodology presented by Lee and others (1981) can be used to estimate S_{us} and S_{ur} at any depth. Two premises must hold in order to use this approach: (1) the sediment type and index characteristics must remain roughly constant with increasing subbottom depth, and (2) the OCR at any depth must be predictable. Analysis of the consolidation test data, visual inspection of the cores, and nearby DSDP drilling results (see Chapter 1) indicate that, although variable, the two premises likely hold for the Horizon Guyot sediment cap. Visual inspection of the Horizon Guyot cores show unbroken, homogeneous calcareous ooze throughout their length. Two Deep Sea Drilling Project (DSDP)

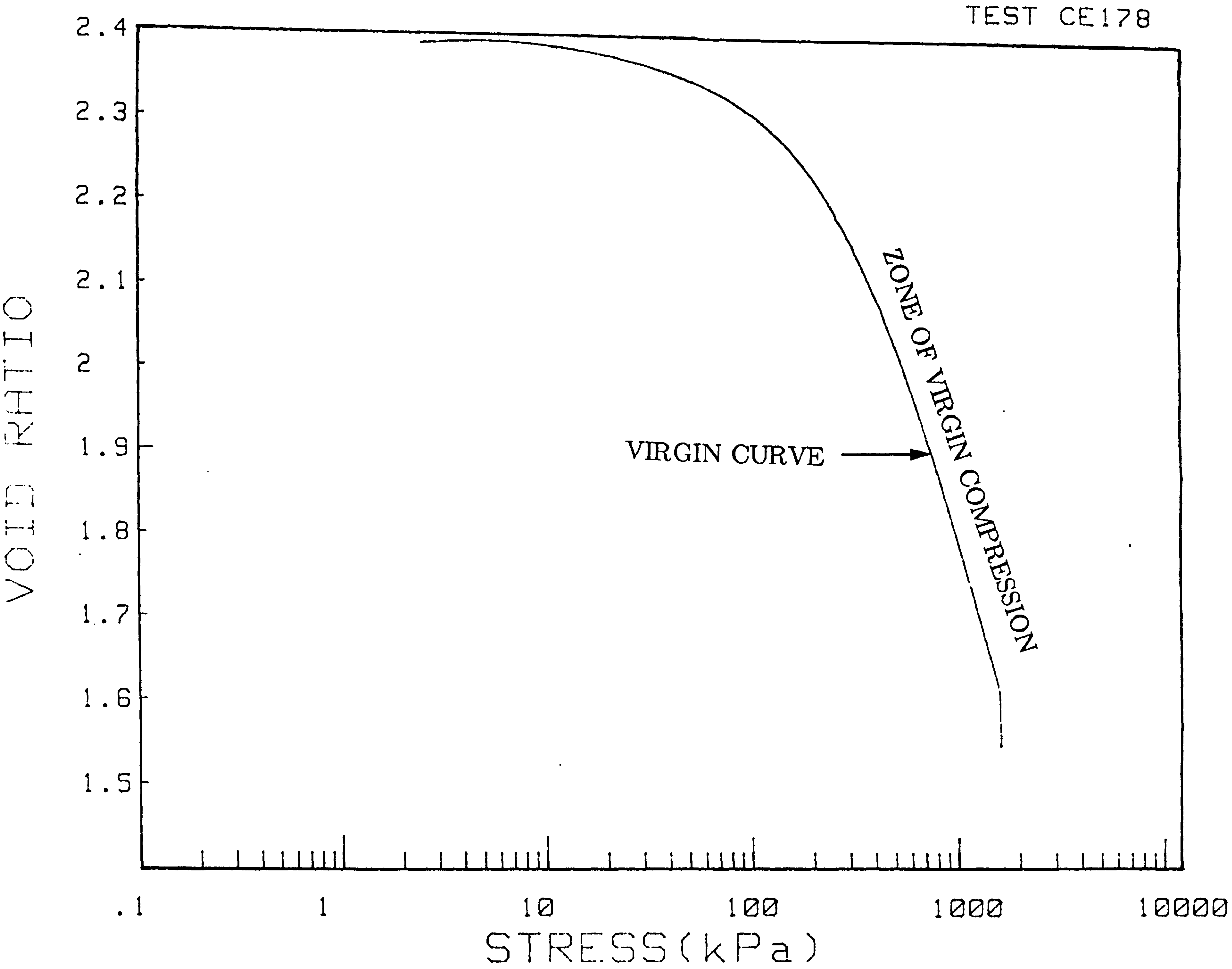

Figure 2-1. Example of a consolidation curve (see Appendix 2-1)

TABLE 2-2

Consolidation Test Results

TEST NO.	CRUISE	CORE	DEPTH (cm)	w (%)	σ'_{vm} (kPa)	σ'_{vo} (kPa)	σ'_{e} (kPa)	OCR	C_c
CE144	L5-83-HW	GC2	303	84.3	630	15.0	615	42	0.88
CE145	L5-83-HW	GC3	103	82.5	250	5.4	245	46	0.73
CE179	L9-84-CP	GC4	123	87.1	330	6.6	323	50	0.80
CE177	L9-84-CP	GC7	95	93.8	230	4.0	226	57	0.81
CE178	L9-84-CP	GC7	170	93.3	300	8.0	292	37	0.93
CE181	L9-84-CP	GC7	261	70.0	420	14.5	405	28	0.42
CE175	L9-84-CP	GC8	120	76.8	190	6.0	184	32	0.60
CE180	L9-84-CP	GC8	156	78.2	420	8.0	412	51	0.73
CE176	L9-84-CP	GC8	200	78.7	610	11.0	600	55	0.43

sites on Horizon Guyot also recovered homogeneous calcareous ooze (see Chapter I). On Leg 6 (Fisher, Heezen, and others, 1971) 24 m of uniform yellowish white nannofossil-foram oooze was recovered. On Leg 17 (Winterer, Ewing, and others, 1973), 148 m of similar calcareous ooze was recovered. Therefore, the measured, normalized triaxial shear strength parameters and index properties are probably representative of deep sediment. Because maximum past stresses derived from nine consolidation tests increase with subbottom depth (Fig. 2-2), estimations of σ_{vm}' can be made by extrapolation of the data.

The undrained shear strength under earthquake loading may be estimated at a particular depth by the following equation (modified from Lee and others, 1981),

$$S_{ur} = \sigma_{vo}' \, A_c \, A_r \, S_{nc} \, [(\sigma_{vo}' + \sigma_e')]^m \qquad (2)$$

where S_{ur} is the in-place undrained shear strength under cyclic loading at a particular subbottom depth, z, σ_{vo}' is the effective vertical stress at z, σ_e' is the excess effective consolidation stress at z and is equal to $\sigma_{vm}' - \sigma_{vo}'$, S_{nc} is the normally consolidated normalized static shear strength of the sediment (following the NSP approach, this factor is a constant for the same sediment and is equal to the measured S_{us} for a normally consolidated sediment divided by σ_{vo}'), m is a normalized strength behavior parameter that is constant for similar sediment and is constant for various consolidation states, A_c is a factor that is used to correct isotropically consolidated triaxial test results to agree with the anisotropic stress state in the field, and A_r is a cyclic strength correction factor that is used to account for strength degradation from cyclic earthquake loading. The static shear strength, S_{us}, can be calculated using the same equation without the cyclic strength degradation factor, A_r.

Values of S_{ur} were calculated from Equation 2. The individual parameters of Equation 2 were obtained from index properties and static triaxial testing (Table 2-3) and cyclic triaxial testing (Table 2-4) as follows: (1) S_{nc} was obtained from triaxial compression tests where a sample was consolidated well into the normally consolidated range (3 to 9 times σ_{vm}'). The resulting undrained shear strength, S_{us}, was divided by the isotropic consolidation stress, σ_c', to obtain S_{nc}; (2) the parameter m was assummed equal to 0.8 based on previous work (Ladd and others, 1977; Mayne, 1980; Lee and others, 1981; Winters and Lee, 1982; Lee and Schwab, 1983); (3) A_c was assumed equal to 0.8 based on previous work (Lee and others, 1981; Lee and Schwab, 1983; Mayne, 1985); (4) A_r was obtained from cyclic triaxial tests as follows. Samples were consolidated into the normally consolidated range to the same level as those used to determine S_{nc}. Next, the axial load was cycled, with nearly full stress reversal, at a level corresponding to a given percentage of the estimated static strength. Testing was continued until failure (>20% single amplitude strain) occured. Tests were conducted on several samples at different levels of cyclic axial loading, and the number of cycles to failure for each sample was determined. The maximum and minimum single amplitude cyclic shear stress, $\tau_{cyc.\ ave.\ max.}$ and $\tau_{cyc.\ ave.\ min.}$, normalized by the static shear strength, S_{us}, were plotted versus the log of the number of cycles to failure (Fig. 2-3). A linear regression of the average normalized cyclic shear stress, τ_{cyc}/S_{us}, versus the number of cycles to failure is constructed in Figure 2-3. The cyclic shear stress level corresponding to 10

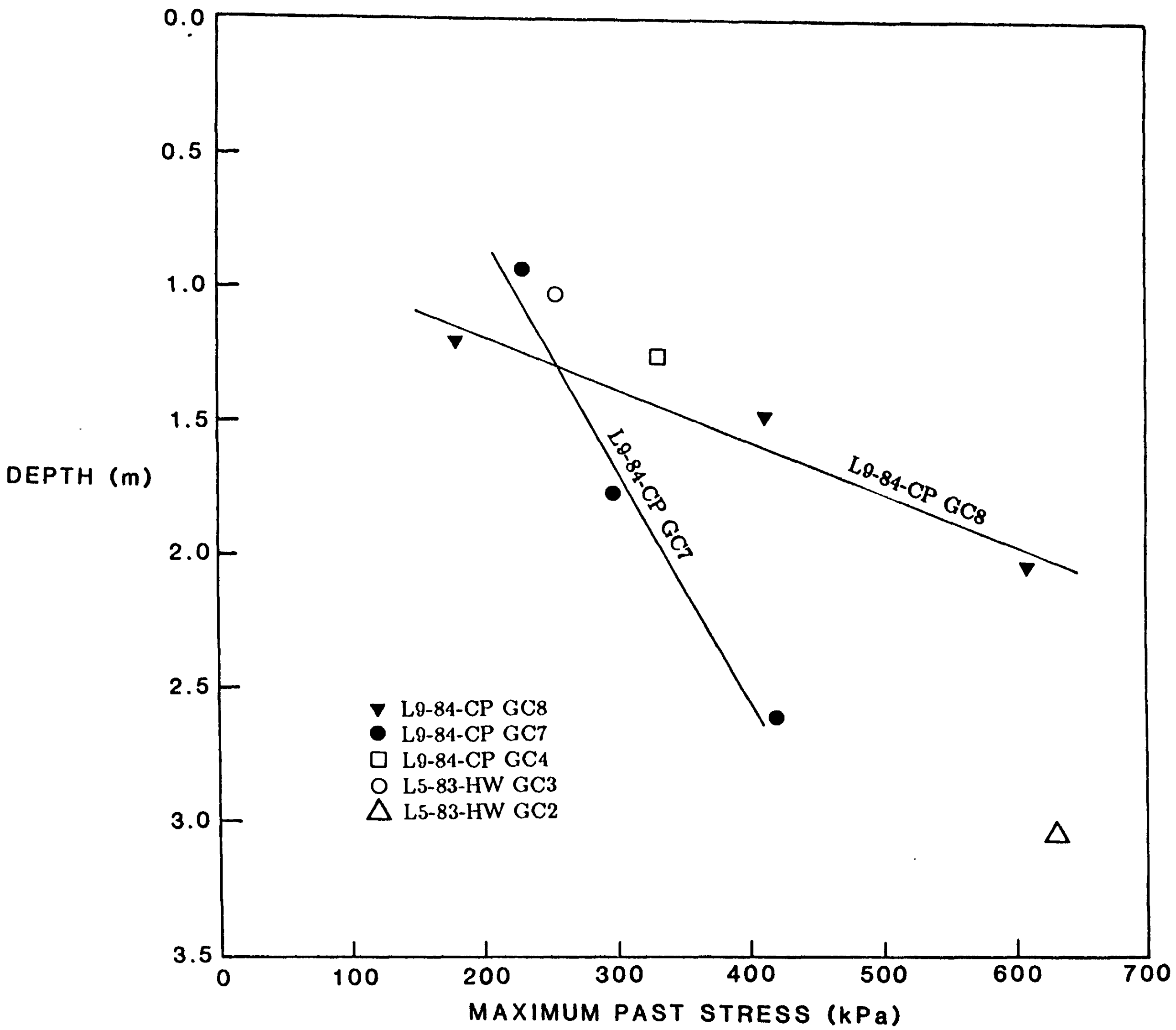

Figure 2-2. Subbottom depth versus maximum past stress.

TABLE 2-3

Static Triaxial Test Results

TEST NO.	CRUISE	CORE	DEPTH (cm)	w (%)	STRAIN AT FAILURE (%)	σ_c' (kPa)	σ_c'/σ_{vm}'	q at failure (kPa)	p' at failure (kPa)	ϕ' (degrees)	S_{nc}
TH9	L9-84-CP	GC4	115	90.8	1.91	1828.0	5.50	561.0	1728.0	39.5	0.31
TH11	L9-84-CP	GC7	265	75.9	1.92	1807.0	4.30	619.0	1263.0	41.7	0.34
TH280	L9-84-CP	GC7	275	65.8	20.07	12.4	0.03	54.3	86.8	39.7	-
TH6	L9-84-CP	GC8	100	83.9	5.60	760.0	4.00	308.0	674.0	31.9	0.40
TH7	L9-84-CP	GC8	110	83.6	0.85	574.0	3.00	212.0	438.0	41.4	0.37
TH8	L9-84-CP	GC8	125	88.9	1.65	1712.0	9.00	551.0	1332.0	35.1	0.32
TH10	L9-84-CP	GC8	196	77.2	1.40	1818.0	3.00	613.0	1526.0	38.4	0.34

TABLE 2-4

Cyclic Triaxial Test Results

TEST NO.	CORE	DEPTH (cm)	w (%)	ρ (g/cc)	σ_c' (kPa)	STRAIN AT FAILURE(%)	NUMBER OF CYCLES TO FAILURE	τ_{cyc}/S_{us} (%)max	(%)min
D221	GC8	70	78.9	1.52	572.1	3.21	3	95.7	85.5
D220	GC8	80	81.4	1.65	577.3	4.94	14	88.0	75.9
D217	GC8	130	85.5	2.05	585.0	5.77	296	53.9	55.0
D216	GC8	90	81.2	1.86	570.8	4.32	49	84.2	72.9

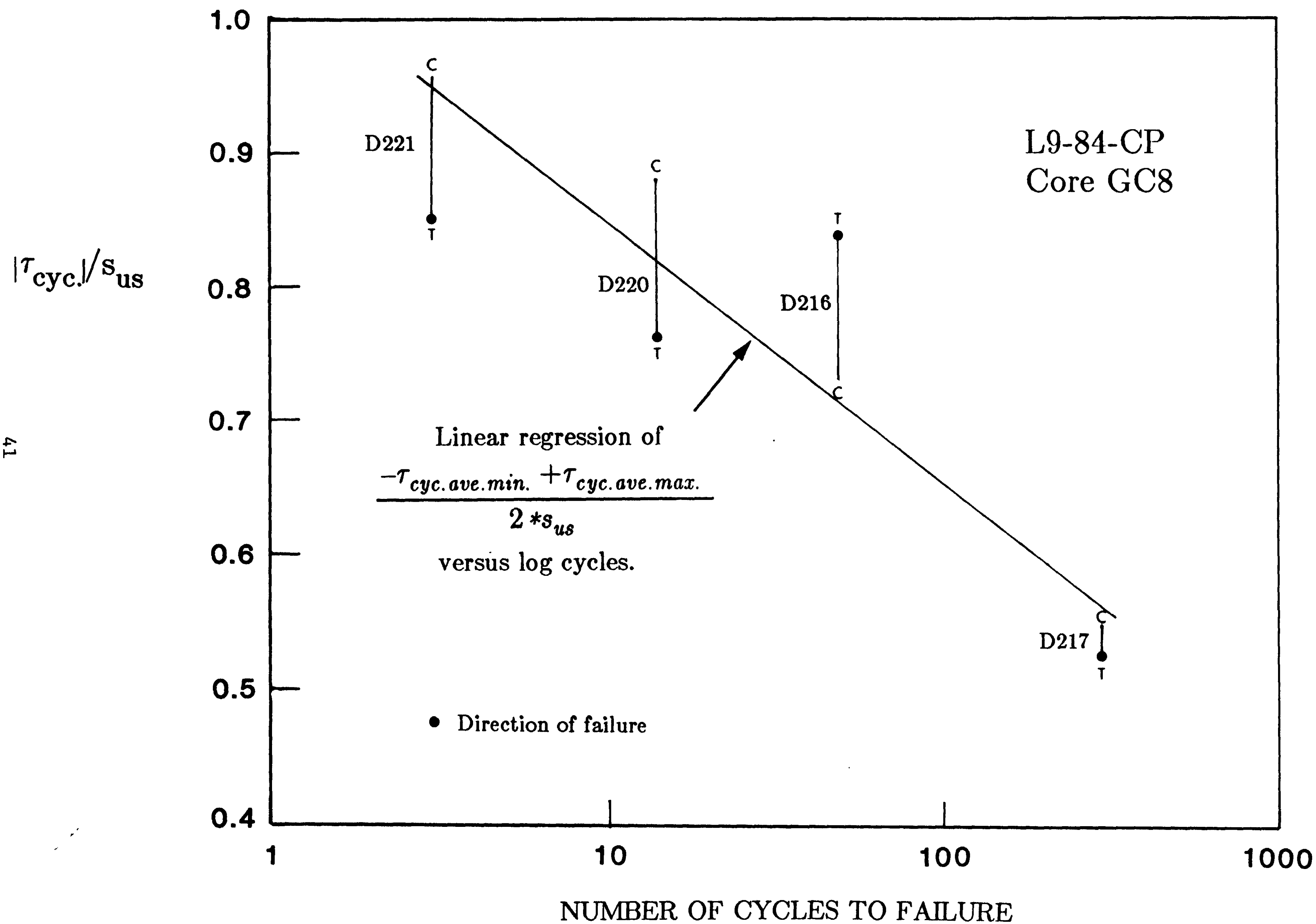

Figure 2-3. Average normalized cyclic shear stress versus log cycles to failure, where C indicates the compression cycle and T the tensile cycle.

cycles (typical number of cycles for a moderate earthquake) was determined from the regression line. The cyclic strength degradation factor, A_r, was taken as the 10-cycle-to-failure average shear stress level divided by the assumed static shear strength using equation 2 without A_r. For core GC8, A_r was determined to be 0.85 (Fig. 2-3).

The vertical effective stress at any given subbottom depth, σ_{vo}', was calculated by multiplying the average bouyant unit weight of the overlying sediment, γ', by the subbottom depth, z. The bouyant unit weight was calculated from the equation:

$$\gamma' = [(G_s \rho_w - \rho_w)/(1+e)] \qquad (3)$$

where G_s is the grain specific gravity, e is the void ratio (determined from the log vertical stress-consolidation curves), and ρ_w is the unit weight of sea water.

The excess effective stress parameter, σ_e', within the subbottom depths that were sampled, was determined from the consolidation tests. Two different assumptions were made regarding the variation of σ_e' below the sampled depth: (1) Overconsolidation effects are caused by erosion (i.e., σ_e' is constant with increasing subbottom depth and equal to the average measured σ_e'), and (2) The material is normally consolidated below a "transition zone" (i.e., $\sigma_e' = 0$ at depth). Assumption (2) implies that the observed overconsolidation within the tested samples is caused by apparent overconsolidation in the surficial sediment. That is, interparticle bonding or surficial effects such as reworking by bottom currents produces an unusually dense or rigid sediment near the sea floor. At greater depth, these effects are lost and the sediment appears normally consolidated. Excess effective stress estimations are tabulated for deep and shallow sediment on Table 2-5.

Laboratory Triaxial Test Methods

Cylindrical samples were trimmed using a wire saw with typical dimensions of 3.6 cm in diameter and 7.5 cm in height. A thin membrane was slipped over the sample to isolate it from the deaired confining fluid of the triaxial cell chamber and water was slowly flushed through the sample to expel any interstitial air. The cell and sample water pressure were then raised to dissolve any remaining air bubbles; thus completing saturation. Pore water lines connected to the top and bottom of the test specimen allowed either drainage or pore water pressure measurement during undrained shear.

Upon completion of saturation (typically overnight), the sample was consolidated by increasing the confining cell water pressure and allowing the sample pore water to drain. Coring disturbance was partially removed by consolidating each sample to a stress between 3 and 9 times σ_{vm}'. The ratio of consolidation stress, σ_c', to σ_{vm}' was varied in order to observe its effects on S_{nc} and on the effective internal friction angle, ϕ'. The pore pressure drainage valve was closed after the sample was fully consolidated and the sample was axially loaded at a constant rate of strain of approximately 0.35 cm/hr. Axial strain, axial loads, and pore water pressure were automatically logged at specific intervals.

TABLE 2-5

Estimates Of σ_e' For Slope Stability Analysis

CRUISE	CORE	DEPTH (m)	σ_e' (kPa) Assumption 1	σ_e' (kPa) Assumption 2
L5-83-HW	GC2	shallow	615	615
L5-83-HW	GC2	40	615	0
L5-83-HW	GC3	shallow	245	245
L5-83-HW	GC3	40	245	0
L9-84-CP	GC4	shallow	323	323
L9-84-CP	GC4	40	323	0
L9-84-CP	GC7	shallow	308	308
L9-84-CP	GC7	40	308	0
L9-84-CP	GC8	shallow	399	399
L9-84-CP	GC8	40	399	0

Samples were trimmed and consolidated in the same manner for the cyclic triaxial tests. When consolidation was complete, each sample was loaded with a 0.1 Hz sinusoidally varying axial load creating almost full stress reversals at a specified percentage of the undrained static shear strength.

Test plots for static and cyclic triaxial compression tests are presented in Appendices 2-4 and 2-5, respectively. Some cyclic test plots show selected cycles to present a clearer representation of the data.

The general behavior of Horizon Guyot sediment during undraining static triaxial compression testing is represented on the three graphs in Figure 2-4. The plotted parameters are $q = (\sigma_1' - \sigma_3')/2$, $p' = (\sigma_1' + \sigma_3')/2$, and delta u = change in excess pore water pressure (in excess of hydrostatic) where $\sigma_1' - \sigma_3'$ is the deviator stress, σ_1' is the vertical principal effective stress, and σ_3' is the horizontal principal effective stress.

The graph of q versus p' through the course of a test is the effective stress path (Fig. 2-4). Each point on the stress path represents the highest point on a Mohr's circle at a specific time during the test and is effectively a plot of maximum shear stress versus average confining stress. A stress path gives insight into the engineering behavior of the tested sample during shear. If the stress path curves to the left, positive excess pore pressure is developed indicating contractive behavior. If it bends to the right, negative excess pore pressure is developed indicating expansive (dilatant) behavior.

Effective stress paths for samples having the same OCR and sediment type should be similar if the NSP approach is valid. In Figure 2-5, stress paths for 4 triaxial compression tests on Horizon Guyot samples are presented. Each effective stress path is similar, indicating contractive behavior, and defines a similar internal friction angle, ϕ', where $\phi' = \sin^{-1}(q/p')$ with p' and q taken at the point of maximum σ_1'/σ_3', even though they were consolidated to different multiples of maximum past stress (3 to 9 times σ_{vm}') before shear. A reduction of ϕ' due to grain crushing has been reported in other studies for sediment with fragile tests. For example, Valent (1979, p. 152) noted that consolidation stress as low as 30 kPa reduced ϕ' for some Caribbean Sea calcareous ooze from 34.5 to 28 degrees. The similarity of Horizon Guyot sediment effective stress paths indicates that the NSP approach is valid, the sediment is dominated by contractive behavior during shear if in a normally consolidated state, but exhibits dilatant behavior if in a heavily overconsolidated state. Grain crushing was not a significant factor in sediment behavior during shear at consolidation stress levels up to 1828 kPa.

Static triaxial compression tests were conducted on two adjacent samples from core GC7 to determine if the Horizon Guyot sediment was cemented (e.g. a composite structure of grains held together by a calcium carbonate binder). Triaxial test TH11 was conducted using a high pressure system in order to consolidate the sample far into the normally consolidated range (consolidation stress = 1807 kPa) prior to shearing where cementation bonds would be broken. In comparison, the adjacent sample was consolidated in test TE280 to the in place overburden stress (12.4 kPa) prior to shearing, well below its maximum past stress ($\sigma_{vm}' = 413$ kPa), so that any existing cementation bonds would be preserved. Triaxial test TE280, run at the low confining stress, had a ϕ' value 2°-lower-than that of test TH11. Wissa and others (1965),

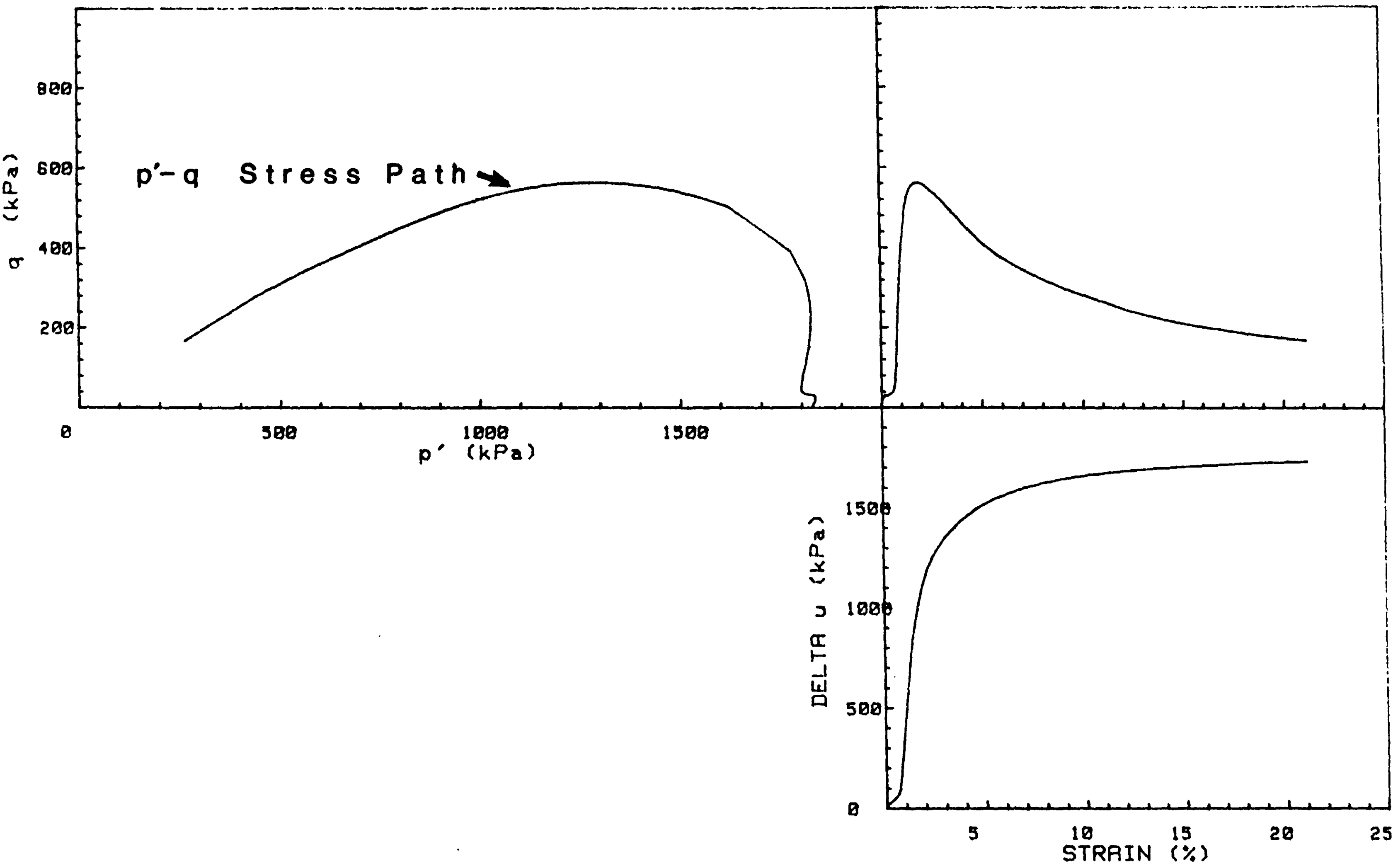

L9-84-CP		INCREMENT (cm)	112-120
CORE NO.	GC4	TEST NO.	TH9
SIG1c'(kPa)	1828.2		
SIG3c'(kPa)	1828.2		
INDUCED OCR	1.0		

Figure 2-4. Representative static triaxial test plots.

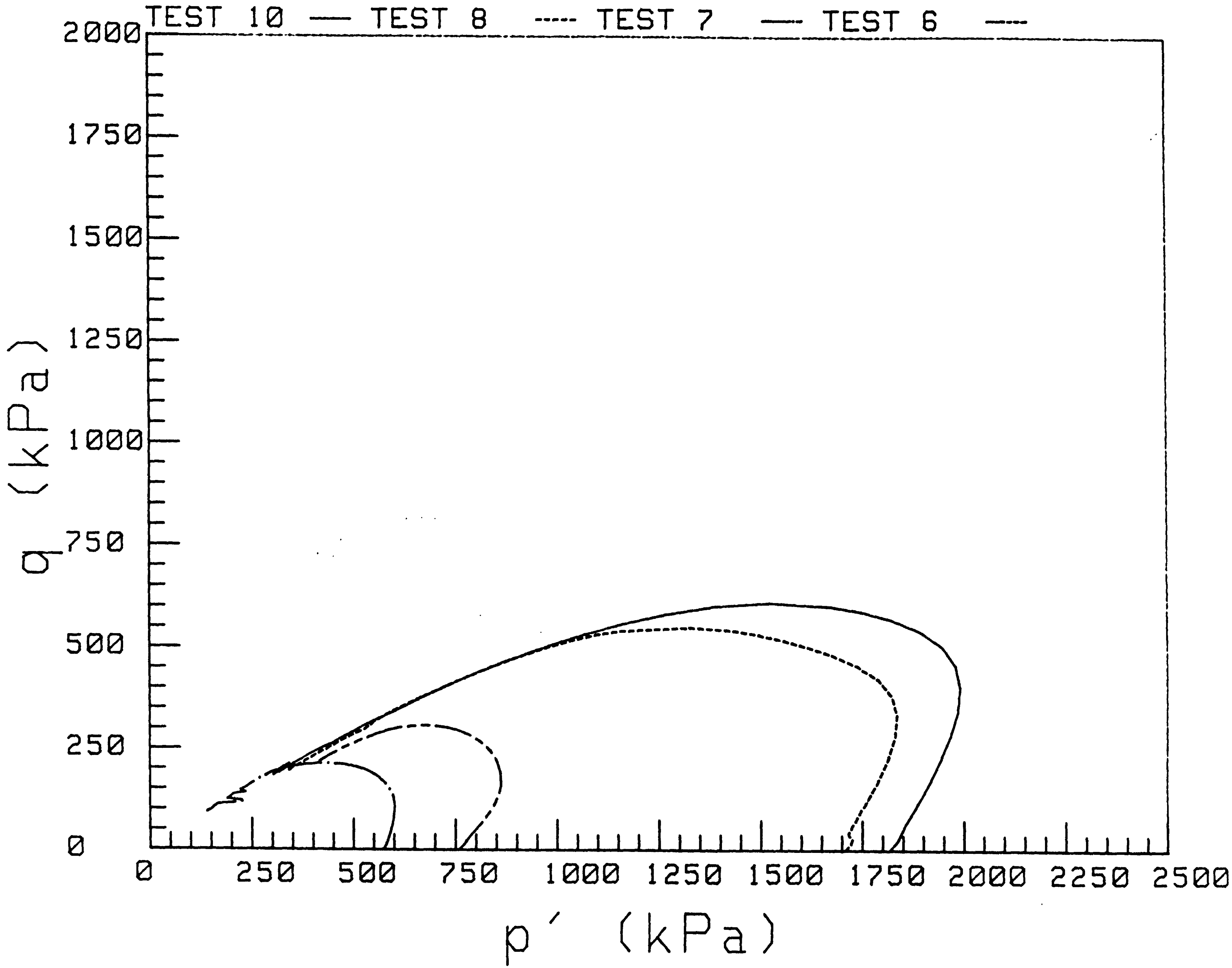

Figure 2-5. Stress paths from four static triaxial compression tests.

conducted similar tests on artificially cemented samples, found as much as a 12° increase in ϕ' for the cemented samples. Therefore, if the Horizon Guyot samples were cemented, the value of ϕ' for test TE280 would probably be higher than that for the normally consolidated samples (test TH11).

Wissa and others (1965) also found that cementation increased the value of the cohesion intercept of the Mohr-Coulomb failure envelope. The stress paths generated from static triaxial compression testing of Horizon Guyot sediment at high strains appear to follow the Mohr-Coulomb failure envelope (Fig. 2-6). For cemented sediment, a tangent drawn to the stress path in this "high-strain" region would have a non-zero cohesion intercept at its intersection with the ordinate, q (Wissa and others, 1965). A tangent drawn to the stress path of test TE280 (Fig. 2-6) indicates that the cohesion intercept of Horizon Guyot sediment is 0, again implying that cementation is not present in the sediment.

Slope Stability Analysis

Lee and Schwab (1983) and Lee and Edwards (1986) present a simplified methodology for evaluating the stability of submarine slopes given the types of geotechnical parameters derived in the previous sections. The method uses the following equation to determine relative stability:

$$k_c = (\rho'/\rho)\ U\ A_c A_r S_{nc}\ [(\sigma_{vo}' + \sigma_e')/\sigma_{vo}']^m - (\rho'/\rho) \sin \alpha \qquad (4)$$

where k_c is a pseudo-static earthquake acceleration required to induce failure (in g's), ρ is the sediment bulk density, U is the degree of consolidation (equal to 1 for slowly deposited sediment such as that on Horizon Guyot), and α is the average slope angle. This equation was derived from the infinite-slope stability theory (Morgenstern, 1967) and NSP generalizations (Ladd and Foott, 1974). The term k_c is a measure of relative stability given a uniform seismic environment. The lower the value of k_c, the less stable a given slope would be during an earthquake. Schwab and Lee (1983) and Lee and Edwards (1985) determined characteristic values of k_c corresponding to the transition between observed failed and unfailed slopes. For the highly seismically active coasts of California and Alaska, the value of k_c was 0.14 g. A similar study of a failed carbonate slope off the less-seismically active southeast coast of Oahu produced a k_c value of 0.07 g (employing assumption 2 regarding σ_e' as discussed above; Winters and Lee, 1982). Although the seismicity of Horizon Guyot has not been determined as part of this study, it is probably less than that of California or Alaska, and more like that of Oahu.

To evaluate k_c for the Horizon Guyot sediment cap, the following values were used: $\rho = 1.5$ g/cc and $\rho' = 0.5$ g/cc (Table 2-1); $A_c = 0.80$ (as discussed above); $A_r = 0.85$ (as discussed above); $U = 1.0$ (as discussed above); $S_{nc} = 0.35$ (Table 2-3, average value); $\sigma_{vo}' = \rho' \times 40$ m $= 200$ kPa, assuming a failure plane at a subbottom depth of 40 m, the greatest subbottom depth of slumping observed on USGS seismic-reflection profile 20 (see Chapter I, Fig. 1-8); $\sigma_e' = 399$ kPa using assumption 1 (average for core GC8 from which A_r was derived) or $\sigma_e' = 0$ kPa using assumption 2 (Table 2-5); $m = 0.8$ (as discussed above); and $\alpha = 1.6^\circ$ to 4° (see Chapter I and Lonsdale and others, 1972).

Four values of k_c are calculated and tabulated below:

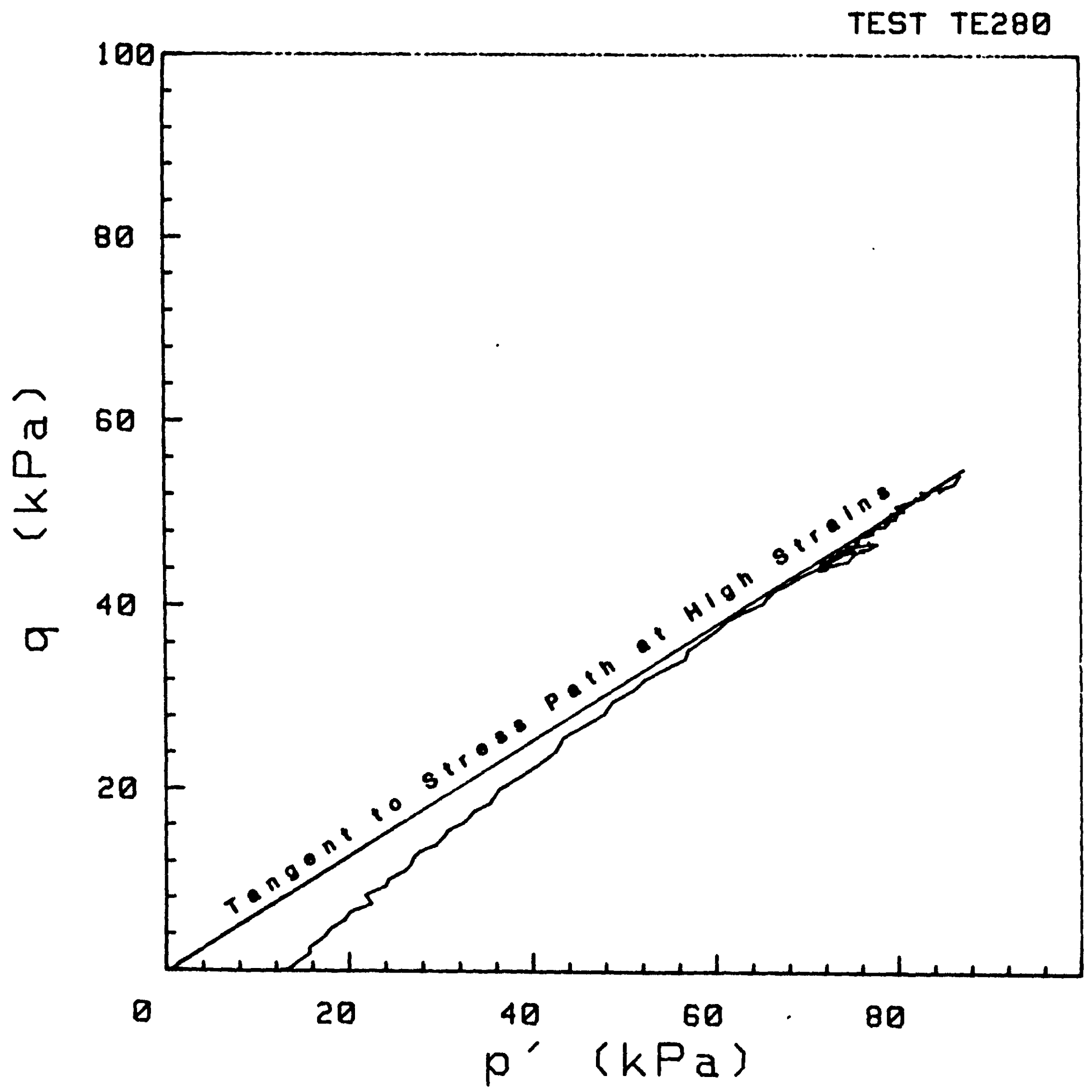

Figure 2-6. Static triaxial compression test q-p' plot for low consolidation stress level, test TE 280.

(A) $k_c = 0.182$ g (assumption 1, $\alpha = 1.6^o$)
(B) $k_c = 0.168$ g (assumption 1, $\alpha = 4.0^o$)
(C) $k_c = 0.070$ g (assumption 2, $\alpha = 1.6^o$)
(D) $k_c = 0.056$ g (assumption 2, $\alpha = 4.0^o$).

The values of k_c obtained using assumption 2 are comparable to those for the failed slope off Oahu. Therefore, if we can neglect the significant overconsolidation of the near-surface sediment and assume that it is lost with burial, the sediment cap of Horizon Guyot is likely to be unstable during infrequent earthquakes. If assumption 1 is valid, however, the average slopes are likely stable. The level of shaking needed to cause slope failure if assumption 1 is valid would be greater than that causing failure off California or Alaska. Perhaps localized failure could occur under the conditions of assumption 1 if bottom current activity eroded a particularly steep local slope prior to an earthquake.

We have shown that interparticle cementation probably is not a cause of surficial overconsolidation in Horizon Guyot sediment. Therefore, the high values of OCR obtained from consolidation testing is either a result of sediment erosion, in which case assumption 1 would apply, or a result of densification by bottom currents. In the latter case the currents would repeatedly move particles relative to each other and gradually produce a more dense surficial configuration. After these "densified" sediment were buried below the level of current-generated movement, they would begin to approach an apparent state of normal consolidation (assumption 2). There is insufficient evidence to select either assumption 1 or 2 at this point. The sediment cap of Horizon Guyot may or may not be stable during seismic loading.

The sediment cap of Horizon Guyot is almost certainly stable during static loading. To represent static loading, k_c is taken as 0 and A_r as 1. Thus, Equation 4 reduces to:

$$A_c \; U \; S_{nc} \; [(\sigma_{vo}' + \sigma_e')/\sigma_{vo}']^m = \sin \alpha \text{ (at failure)}. \qquad (5)$$

For the values given above, sin α (at failure) = 0.67 for assumption 1 and 0.28 for assumption 2. These normalized terms are sediment resistance factors whereas sin $\alpha = 0.028$ to 0.070 are normalized gravitational downslope driving factors for 1.6^o and 4.0^o sea floor declivities, respectively. Therefore, the factor of safety (resisting force/driving force) against static gravitational failure is 4 to 10 for assumption 2 and higher for assumption 1.

Conclusions

(1) The near-surface calcareous ooze that caps Horizon Guyot is fairly heavily overconsolidated.
(2) The overconsolidation is likely not a result of cementation but may result either from erosion or reworking of sediment by bottom currents.
(3) Grain crushing does not appear to be a significant factor at the stress levels used in this testing program.
(4) The sediment cap is probably stable during static loading.
(5) The sediment cap may be unstable during earthquake loading if the overconsolidation was produced by current reworking or if localized undercutting by bottom currents occur.
(6) The sediment cap will be stable during earthquakes if overconsolidation was produced by erosion or if localized undercutting does not occur.

Nomenclature

A_c - A strength correction factor applied to account for the in-place anisotropic stress state of a sample.
A_r - A cyclic strength correction factor applied to account for strength degradation during cyclic loading.
AVE MAX q - Same as $\tau_{cyc.ave.max}$.
C_c - The compression index, defined as the slope of the virgon curve of an e-log p' consolidation plot.
CE - The prefix for a constant rate of strain (CRS) consolidation test number.
D - Prefix for a cyclic triaxial test number.
Delta u - Change in excess pore water pressure (kPa)
e - Void Ratio
g - Acceleration due to gravity, 9.81 m/sec^2.
G_s - Grain specific gravity.
k_c - The pseudo-static earthquake acceleration required to induce a slope failure.
m - A normalized strength parameter that relates the normalized strength of an overconsolidated sediment to its OCR.
NSP - The normalized strength parameter approach, based on the assumption that strength parameters normalized by their consolidation stress are constant for a given sediment with a given OCR.
OCR - The overconsolidation ratio ($\sigma'_{vm}/\sigma'_{vo}$).
p' - The average normal effective stress acting on a sample ($\sigma_1'+\sigma_3'$)/2.
q - Shear stress acting on a sample ($\sigma_1'-\sigma_3'$)/2.
SIG 1'$_c$ - The vertical principal stress applied to a triaxial test sample prior to shear.
SIG 3'$_c$ - The horizontal principal stress applied to a triaxial test sample prior to shear.
S_{nc} - The ratio of the static undrained shear strength of a normally consolidated sediment to its consolidation stress.
STATIC q_f - Strength of a sample obtained from a static triaxial test at a given consolidation stress.
S_{ur} - The undrained cyclic shear strength corrected for cyclic and anisotropic loading conditions.
S_{us} - The undrained static shear strength.
TE - Prefix for a static test number.
U - The degree of consolidation.
w - Water Content expressed as a percentage of dry weight.
W_w - Weight of water.
W_s - Weight of dried sediment and salt.
α - The slope angle (degrees).
ε - Axial strain (degrees).
ϕ' - The Mohr-Coulomb angle of effective shear resistance, or internal friction angle.
ρ - The bulk density of a sediment.
ρ' - The bouyant (submerged) density of a sediment ($\rho-\rho_w$).
ρ_w - The density of seawater (1.025 g/cc).
σ'_1 - The maximum principal effective stress applied at any point during a triaxial test.
σ'_3 - The minimum principal effective stress applied at any point during a triaxial test.
σ'_c - The consolidation stress exerted on a triaxial test sample.
σ'_e - The excess in-place consolidation stress ($\sigma'_{vm}-\sigma'_{vo}$).

σ'_{vo} - The in-place vertical effective stress exerted by the weight of overburden material.

σ'_{vm} - The maximum vertical effective stress that a sediment has ever experienced.

τ_{cyc} - The average single amplitude cyclic stress applied to a sample during a cyclic triaxial test.

$\tau_{cyc.ave.max.}$ - The average single amplitude cyclic compressive stress applied to a sample during a cyclic triaxial test.

$\tau_{cyc.ave.min.}$ - The average single amplitude cyclic tensile stress applied to a sample during a cyclic triaxial test.

APPENDIX 2-1: TEST LOG INDEX PROPERTIES AND SHEAR STRENGTH

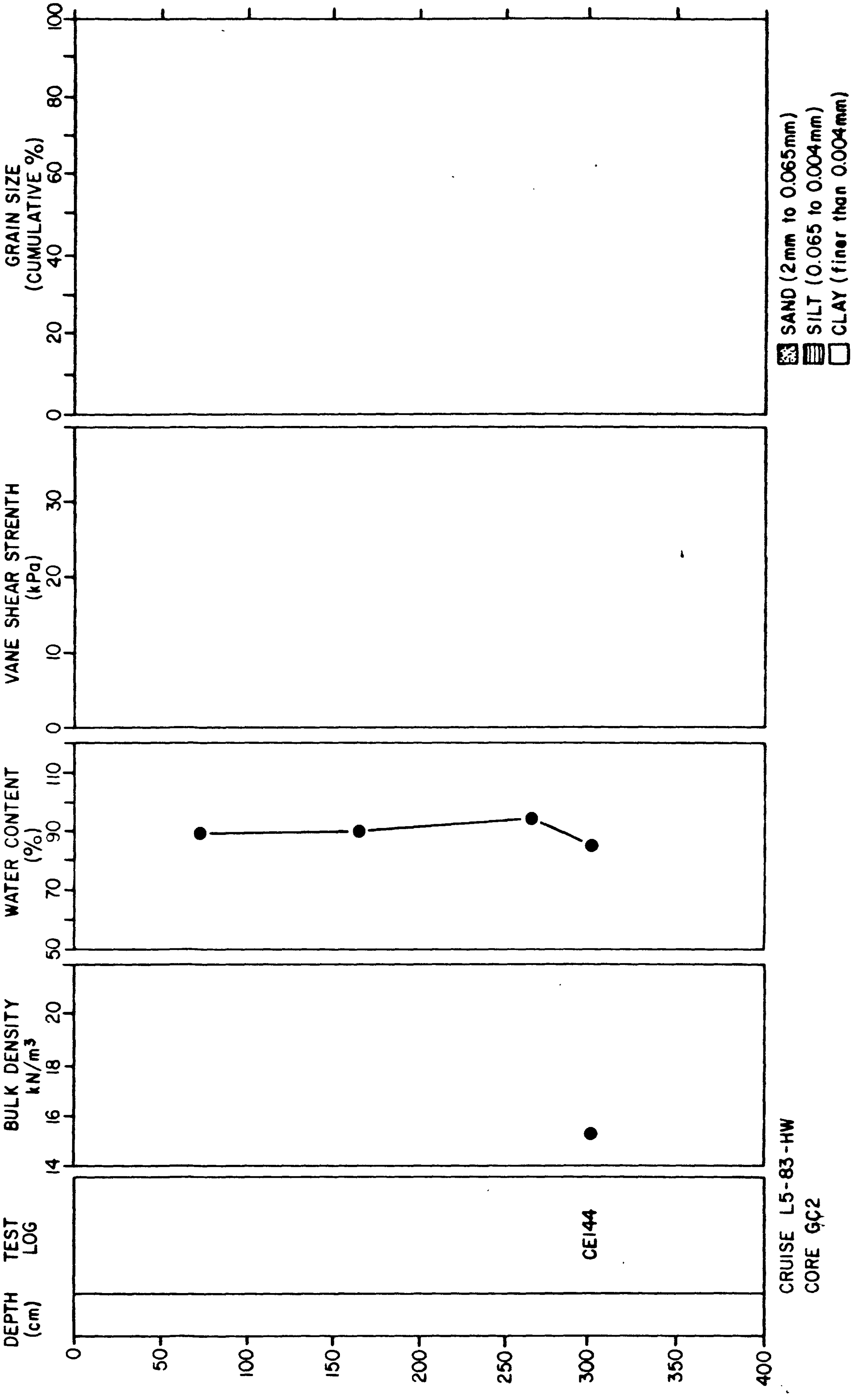
DEPTH (cm)
0
50
100
150
200
250
300
350
400
TEST LOG
CE144
BULK DENSITY kN/m³
14
16
18
20
WATER CONTENT (%)
50
70
90
110
VANE SHEAR STRENTH (kPa)
0
10
20
30
GRAIN SIZE (CUMULATIVE %)
0
20
40
60
80
100
▨ SAND (2mm to 0.065mm)
▤ SILT (0.065 to 0.004mm)
☐ CLAY (finer than 0.004mm)
CRUISE L5-83-HW
CORE GC2

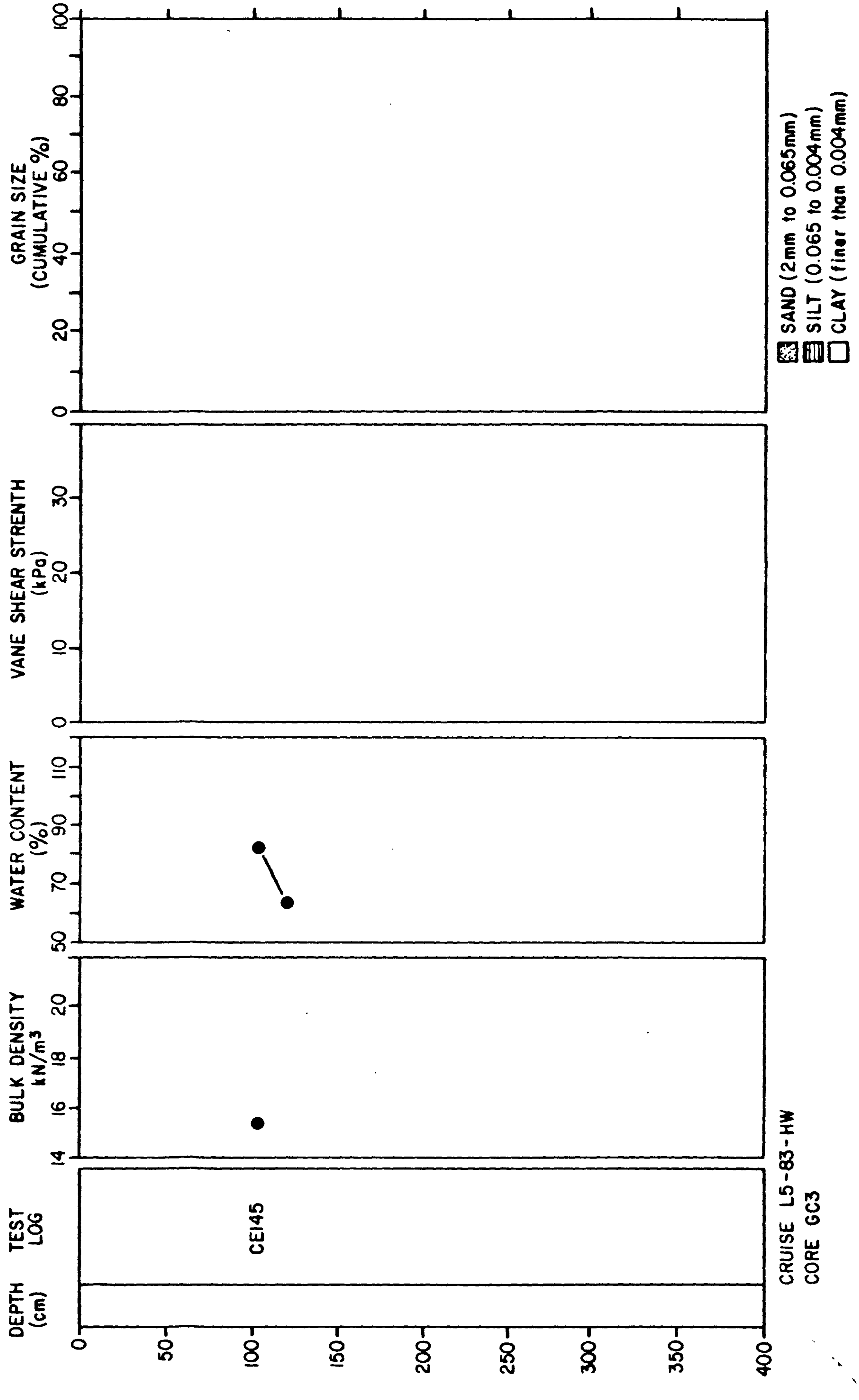
DEPTH (cm)
0
50
100
150
200
250
300
350
400
TEST LOG
CE145
BULK DENSITY kN/m³
14
16
18
20
WATER CONTENT (%)
50
70
90
110
VANE SHEAR STRENTH (kPa)
0
10
20
30
GRAIN SIZE (CUMULATIVE %)
0
20
40
60
80
100
▨ SAND (2mm to 0.065mm)
☰ SILT (0.065 to 0.004mm)
☐ CLAY (finer than 0.004mm)
CRUISE L5-83-HW
CORE GC3

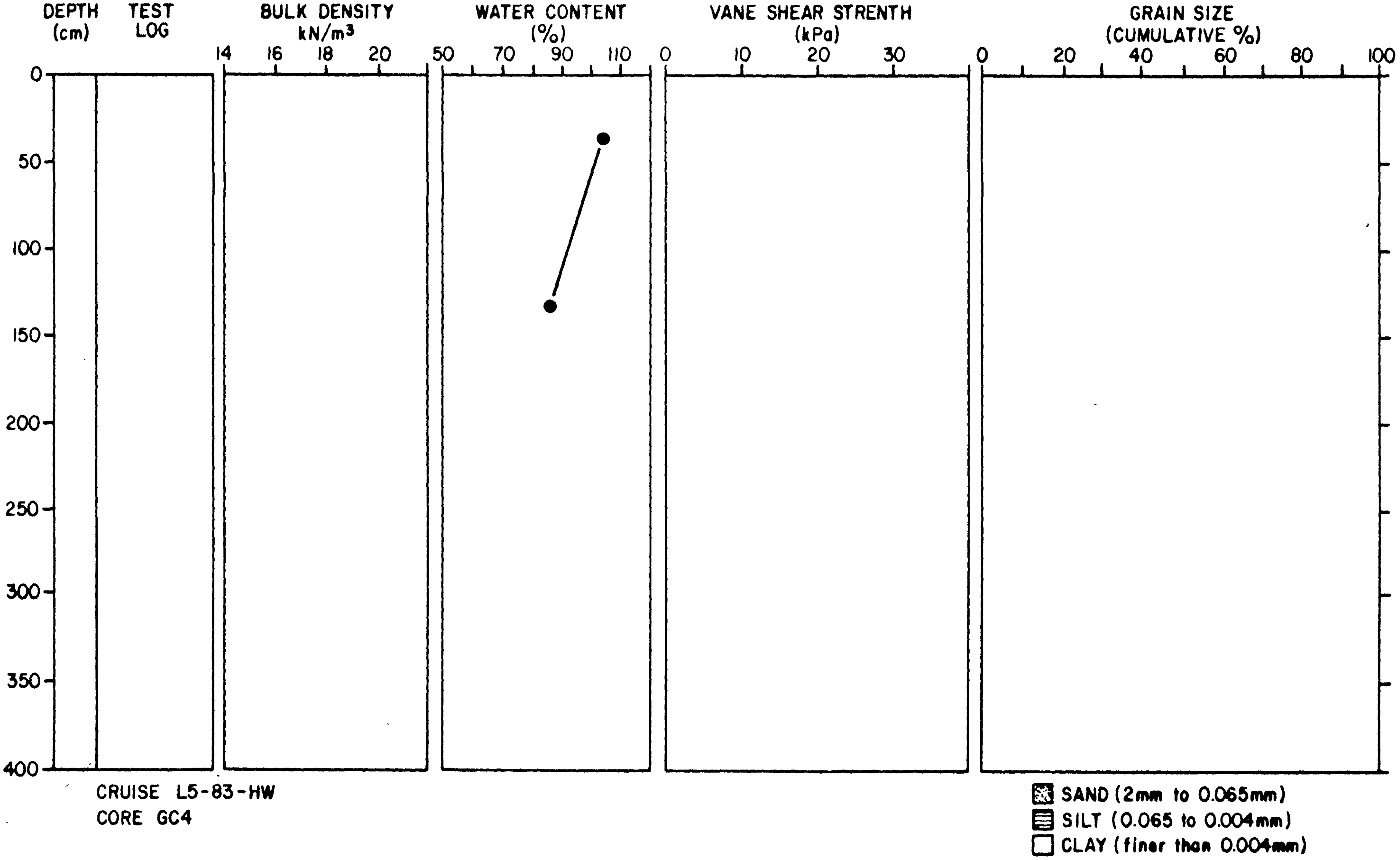
DEPTH (cm)
TEST LOG
BULK DENSITY kN/m³
14
16
18
20
WATER CONTENT (%)
50
70
90
110
VANE SHEAR STRENTH (kPa)
0
10
20
30
GRAIN SIZE (CUMULATIVE %)
0
20
40
60
80
100
0
50
100
150
200
250
300
350
400
CRUISE L5-83-HW
CORE GC4
▨ SAND (2mm to 0.065mm)
▤ SILT (0.065 to 0.004mm)
☐ CLAY (finer than 0.004mm)

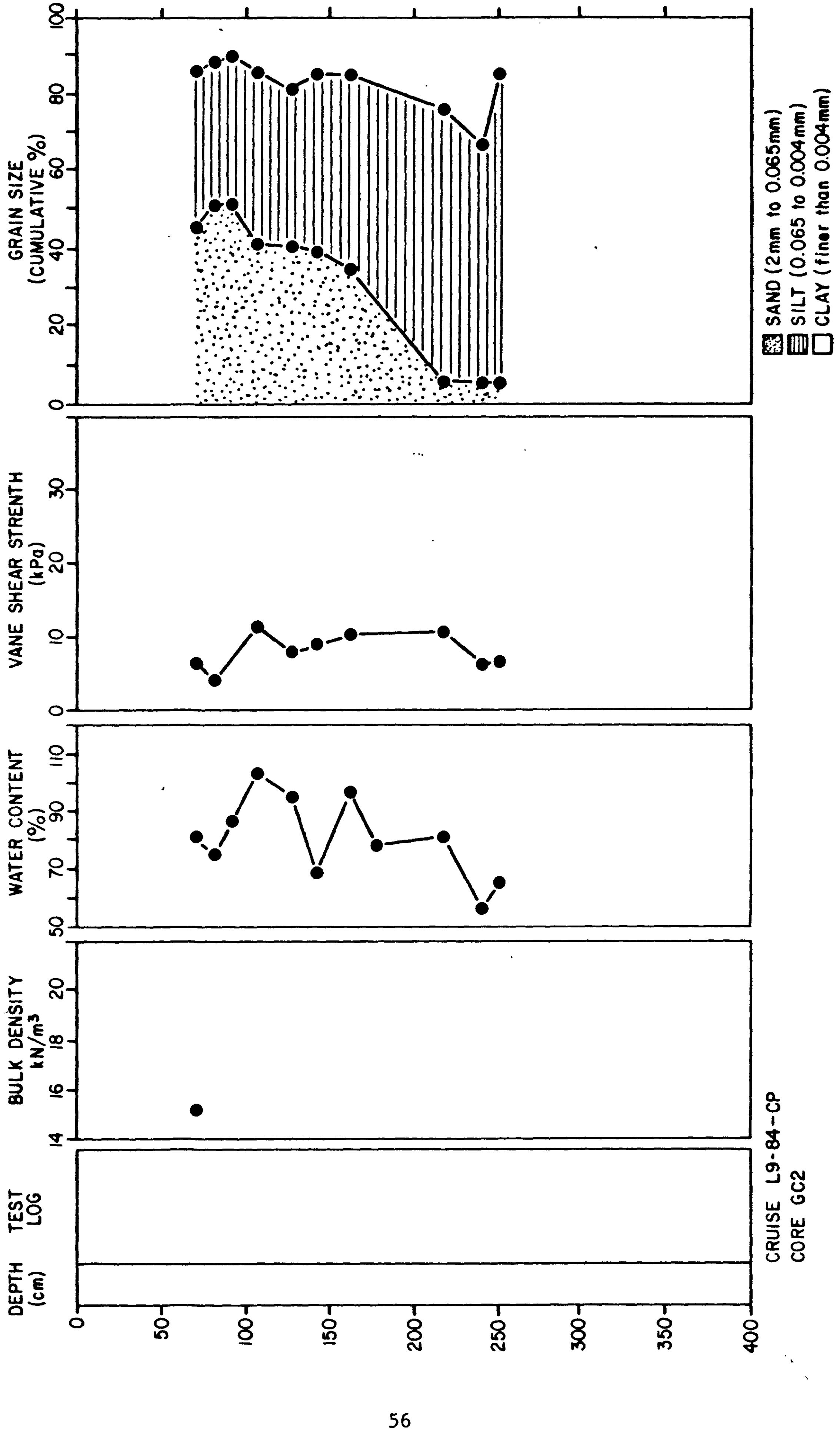

DEPTH (cm)
0
50
100
150
200
250
300
350
400
TEST LOG
BULK DENSITY kN/m³
14
16
18
20
WATER CONTENT (%)
50
70
90
110
VANE SHEAR STRENTH (kPa)
0
10
20
30
GRAIN SIZE (CUMULATIVE %)
0
20
40
60
80
100
▨ SAND (2mm to 0.065mm)
▤ SILT (0.065 to 0.004mm)
☐ CLAY (finer than 0.004mm)
CRUISE L9-84-CP
CORE GC2

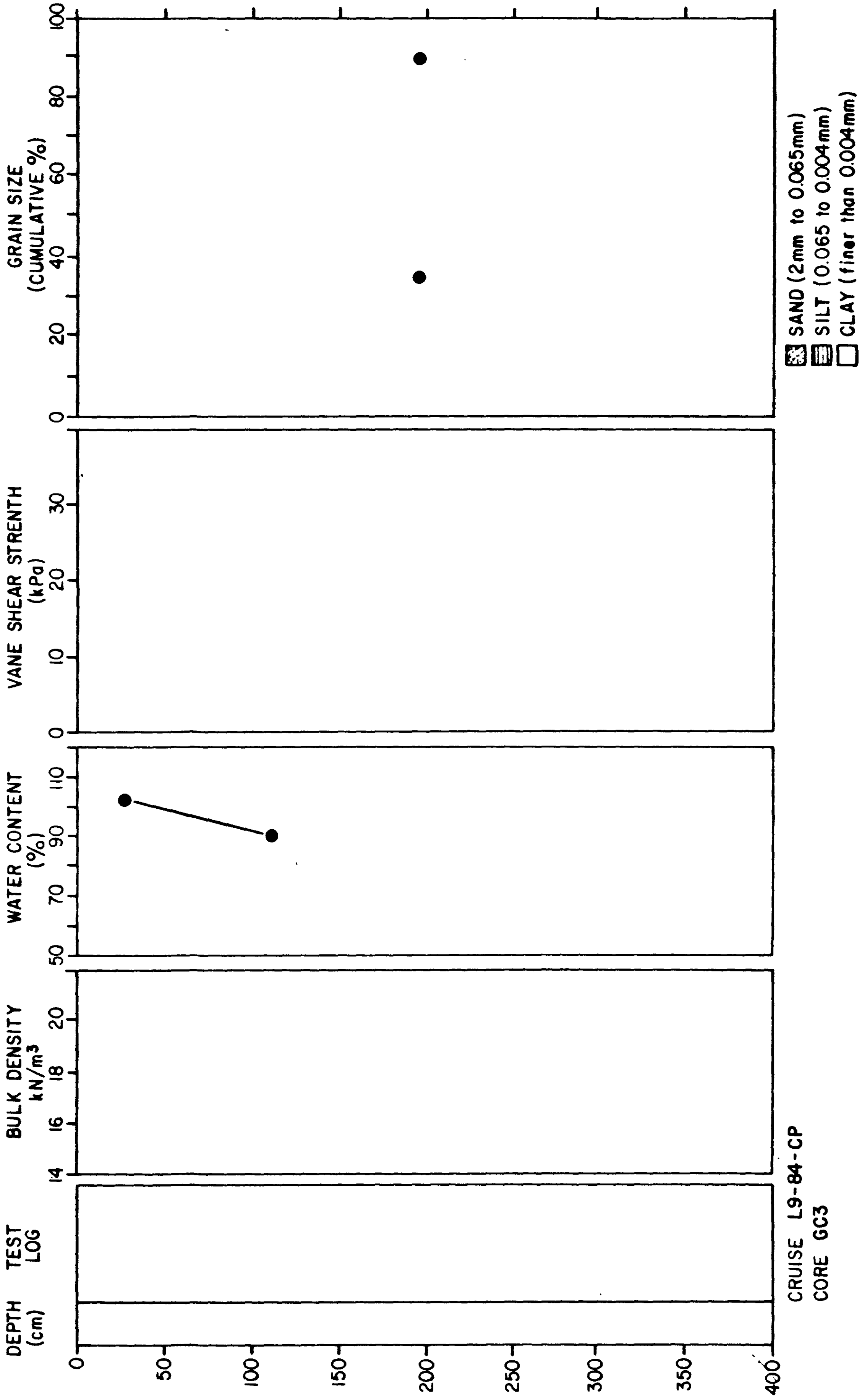
DEPTH (cm)
TEST LOG
BULK DENSITY kN/m³
WATER CONTENT (%)
VANE SHEAR STRENTH (kPa)
GRAIN SIZE (CUMULATIVE %)
0
50
100
150
200
250
300
350
400
14
16
18
20
50
70
90
110
0
10
20
30
0
20
40
60
80
100
SAND (2mm to 0.065mm)
SILT (0.065 to 0.004mm)
CLAY (finer than 0.004mm)
CRUISE L9-84-CP
CORE GC3

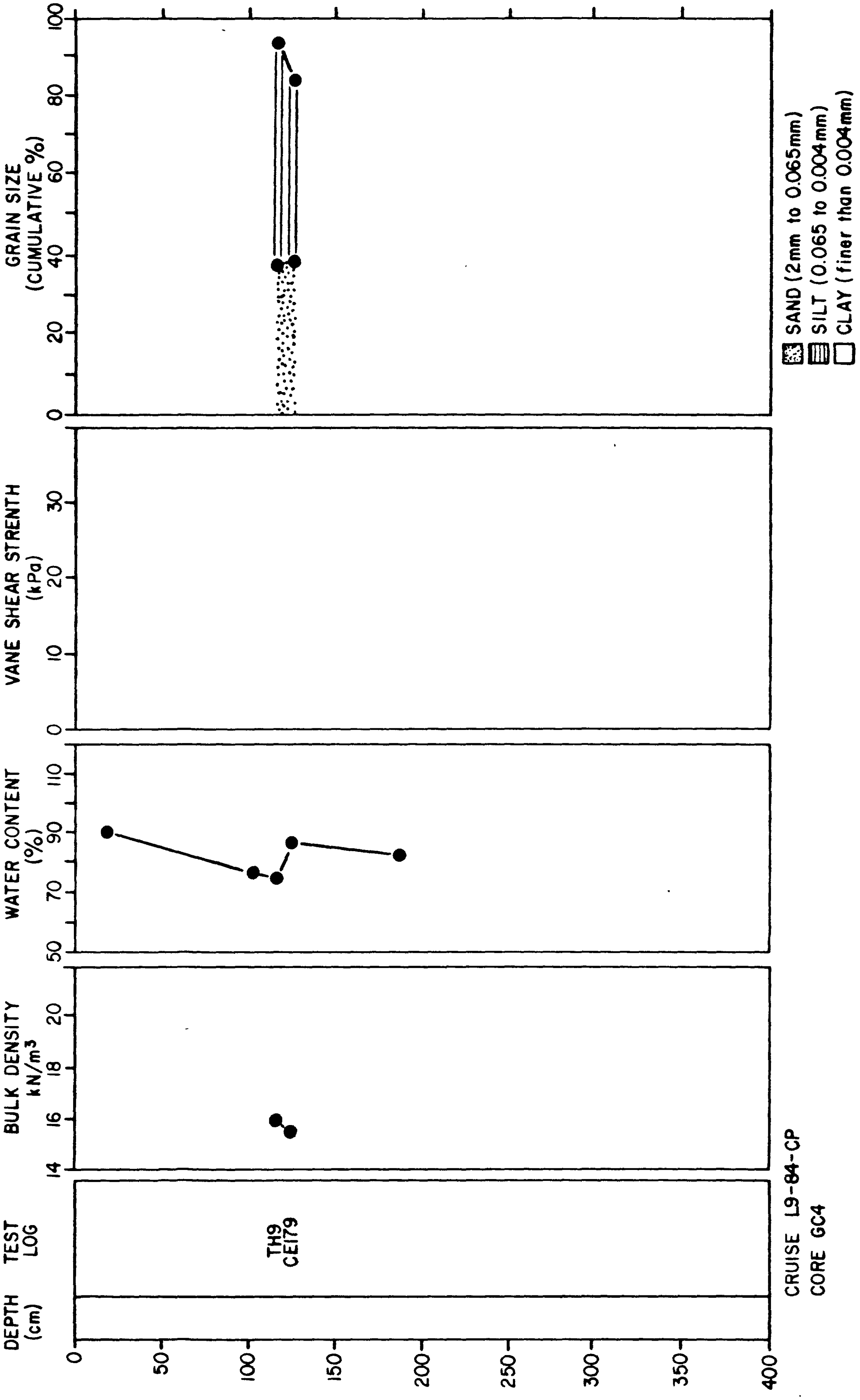
DEPTH (cm)
TEST LOG
TH9
CE179
BULK DENSITY kN/m³
14
16
18
20
WATER CONTENT (%)
50
70
90
110
VANE SHEAR STRENTH (kPa)
0
10
20
30
GRAIN SIZE (CUMULATIVE %)
0
20
40
60
80
100
0
50
100
150
200
250
300
350
400
CRUISE L9-84-CP
CORE GC4
▨ SAND (2mm to 0.065mm)
▤ SILT (0.065 to 0.004mm)
☐ CLAY (finer than 0.004mm)

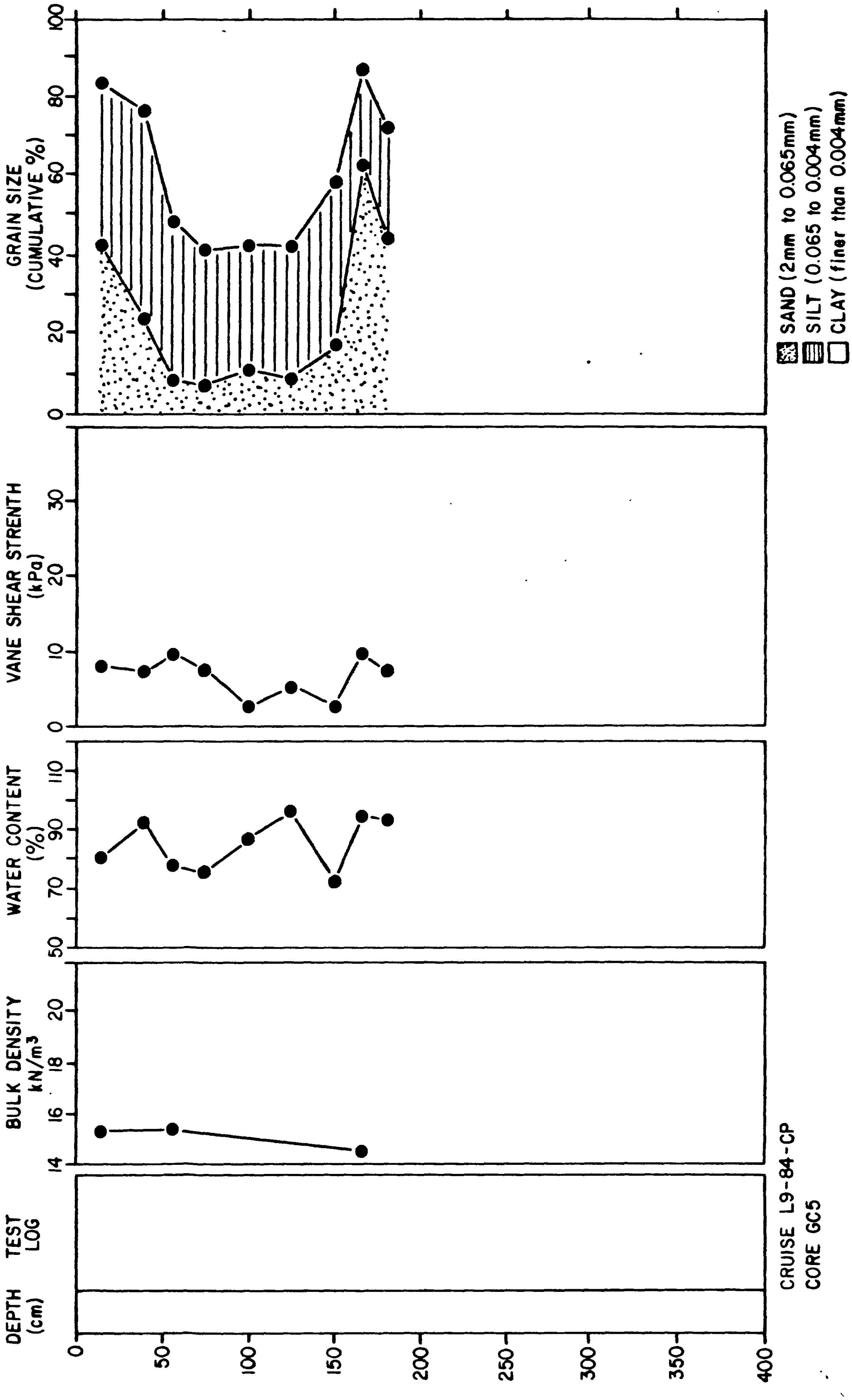
DEPTH (cm)
TEST LOG
BULK DENSITY kN/m³
14
16
18
20
WATER CONTENT (%)
50
70
90
110
VANE SHEAR STRENTH (kPa)
0
10
20
30
GRAIN SIZE (CUMULATIVE %)
0
20
40
60
80
100
0
50
100
150
200
250
300
350
400
CRUISE L9-84-CP
CORE GC5
▨ SAND (2mm to 0.065mm)
▤ SILT (0.065 to 0.004mm)
☐ CLAY (finer than 0.004mm)

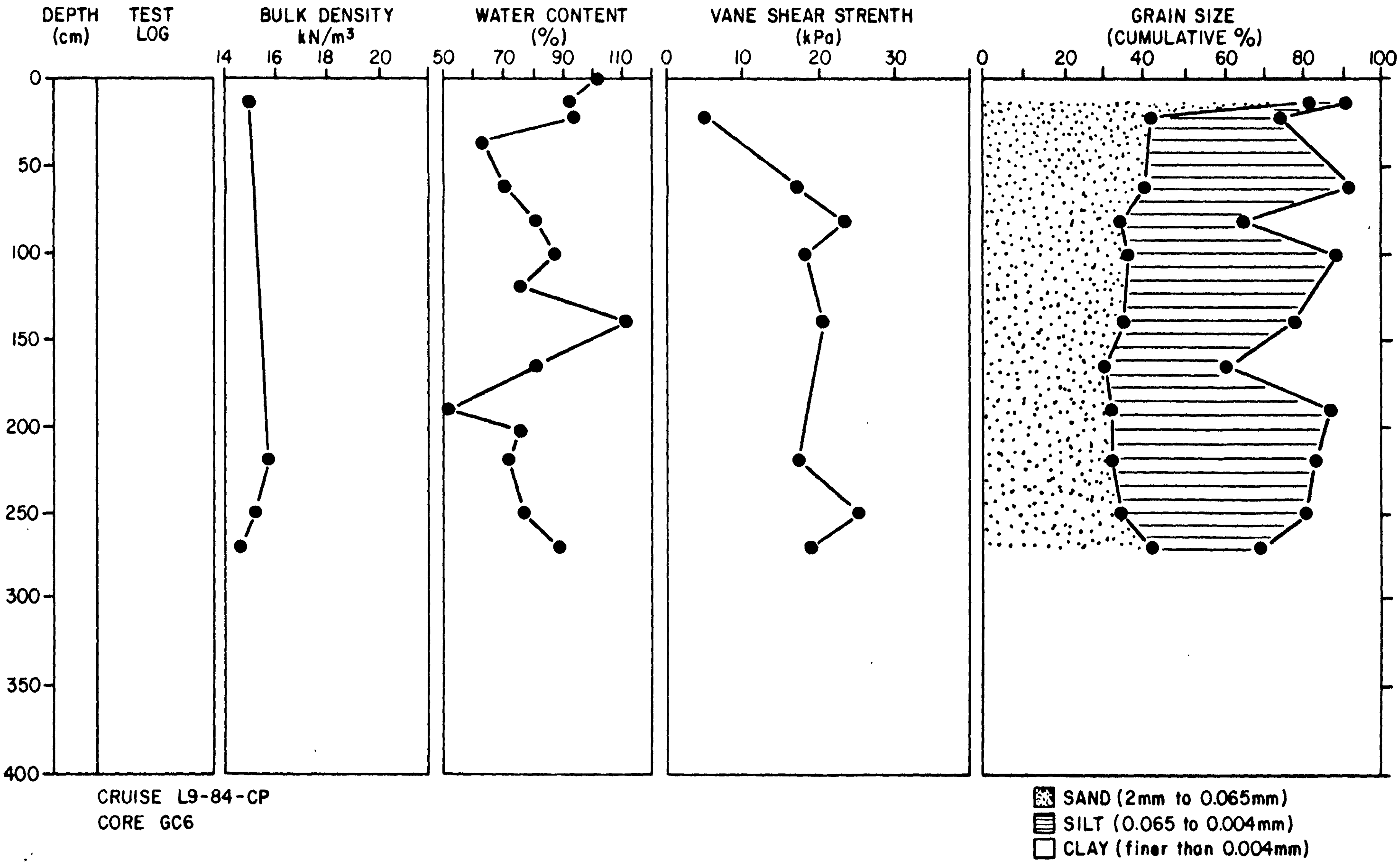

CRUISE L9-84-CP
CORE GC6

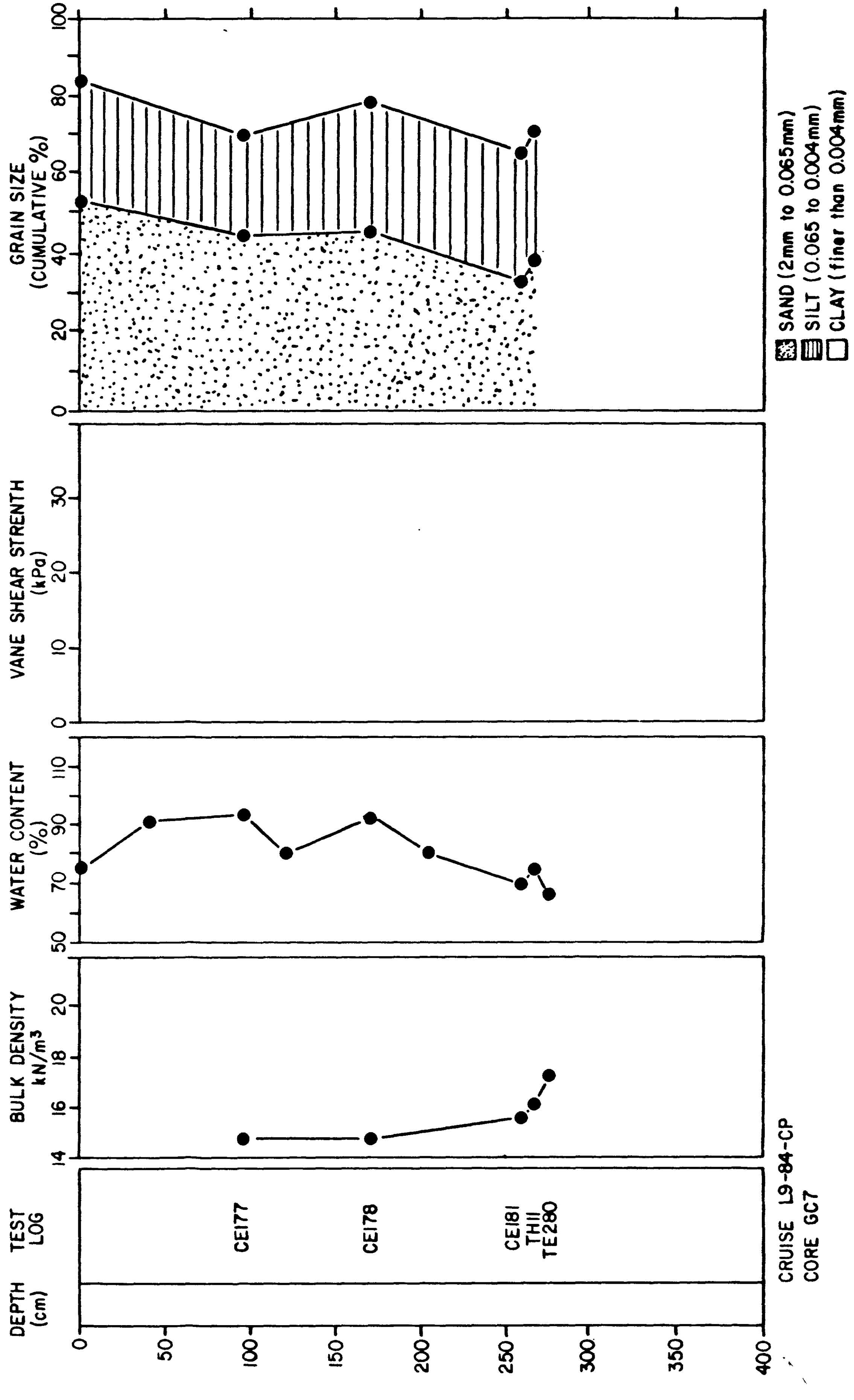DEPTH (cm)
0
50
100
150
200
250
300
350
400
TEST LOG
CE177
CE178
CE181
TH11
TE280
BULK DENSITY kN/m³
14
16
18
20
WATER CONTENT (%)
50
70
90
110
VANE SHEAR STRENTH (kPa)
0
10
20
30
GRAIN SIZE (CUMULATIVE %)
0
20
40
60
80
100
SAND (2mm to 0.065mm)
SILT (0.065 to 0.004mm)
CLAY (finer than 0.004mm)
CRUISE L9-84-CP
CORE GC7

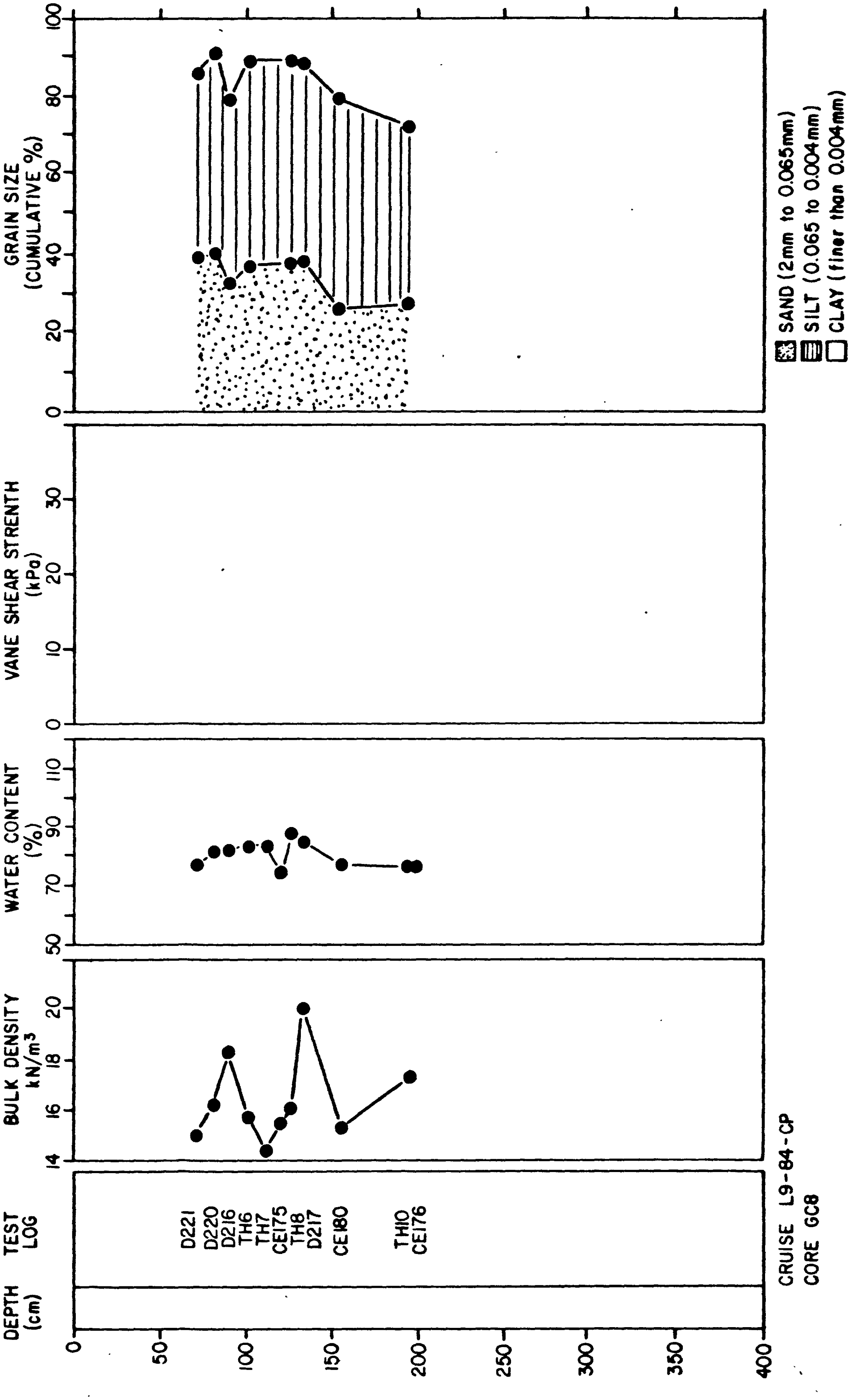

CRUISE L9-84-CP
CORE GC8

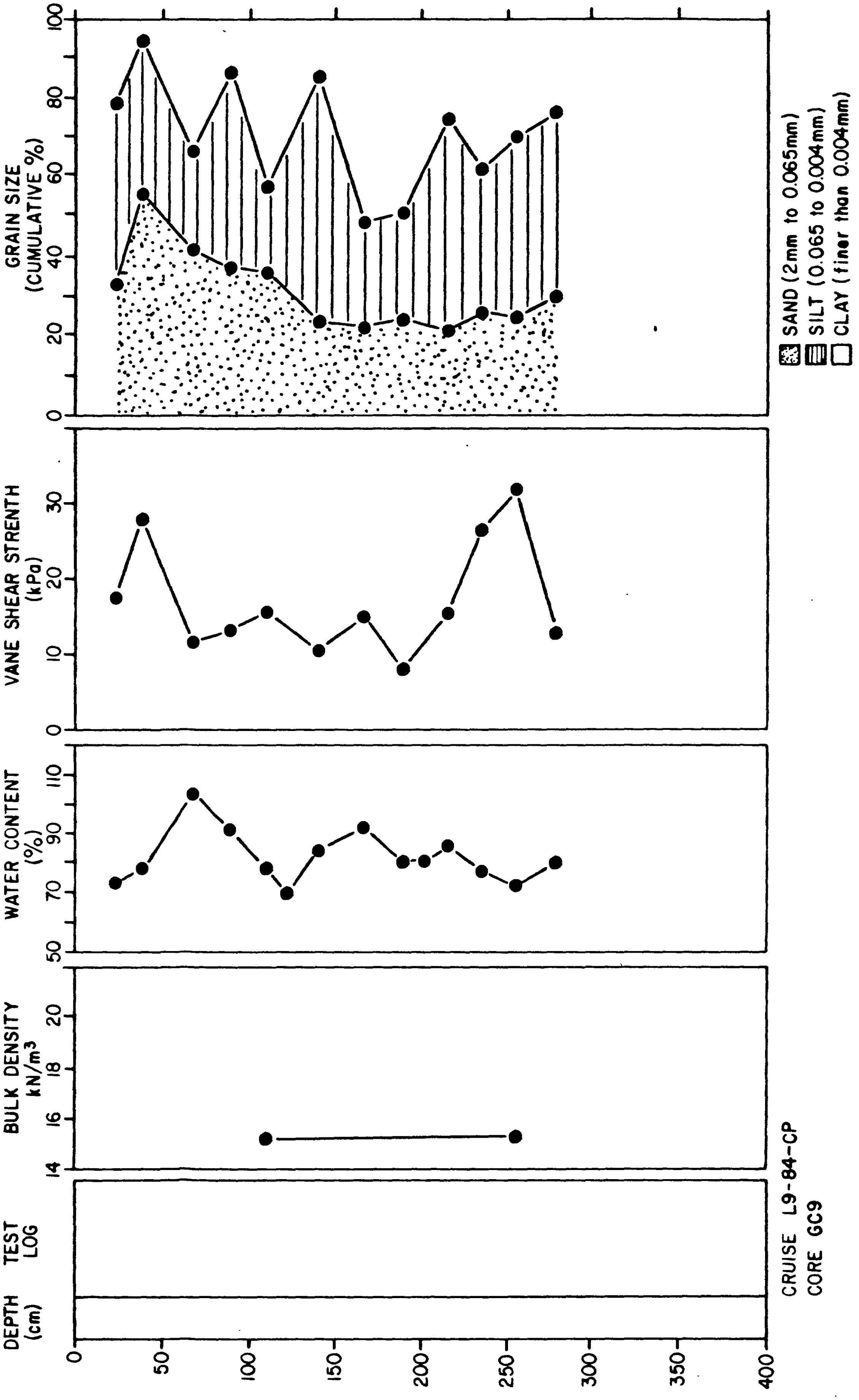
DEPTH (cm)
TEST LOG
BULK DENSITY kN/m³
14
16
18
20
WATER CONTENT (%)
50
70
90
110
VANE SHEAR STRENGTH (kPa)
0
10
20
30
GRAIN SIZE (CUMULATIVE %)
0
20
40
60
80
100
0
50
100
150
200
250
300
350
400
CRUISE L9-84-CP
CORE GC9
▨ SAND (2mm to 0.065mm)
▤ SILT (0.065 to 0.004mm)
☐ CLAY (finer than 0.004mm)

APPENDIX 2-2: GRAIN SIZE CLASSIFICATION PLOTS (CRUISE L9-84-CP).

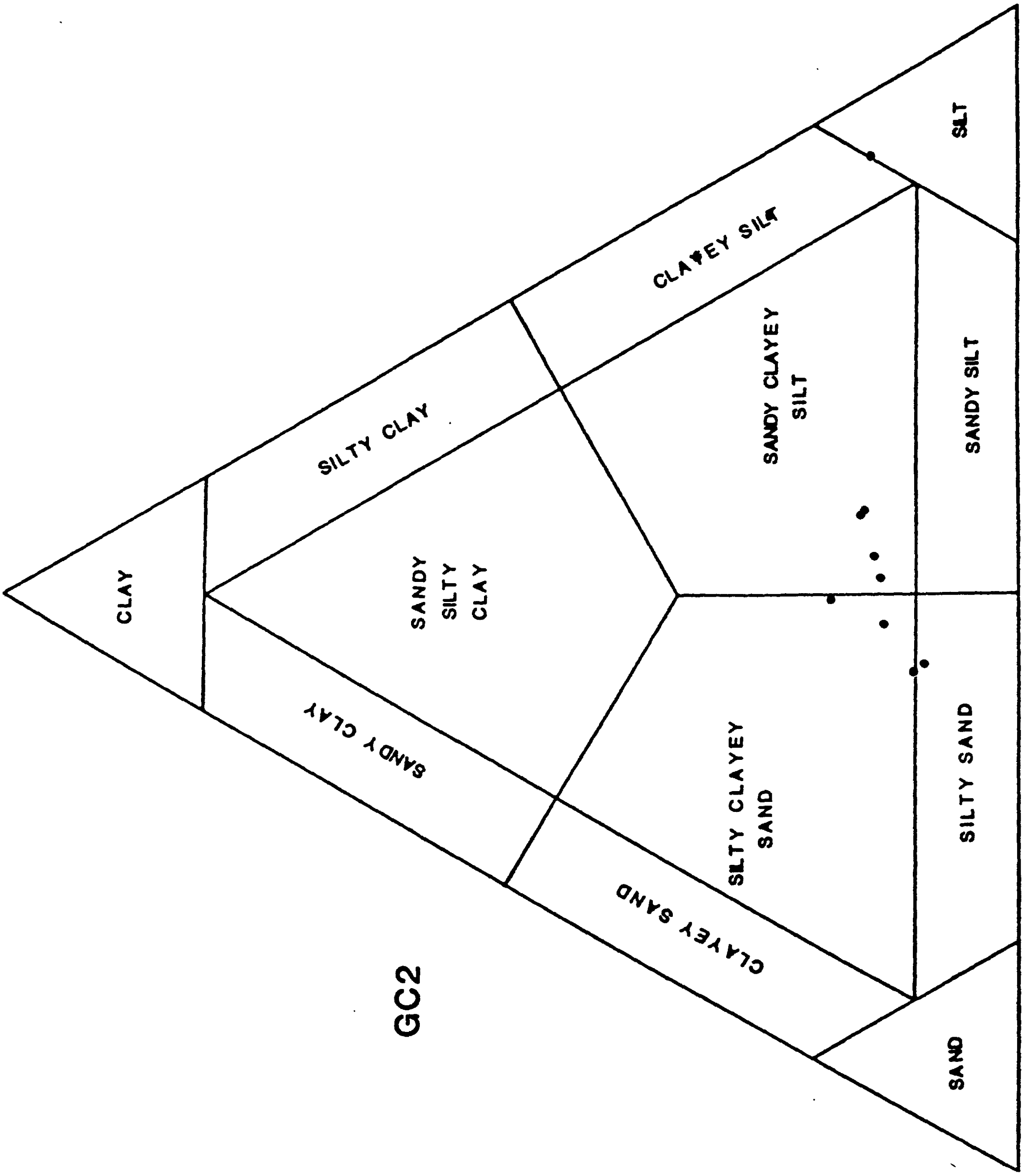
CLAY
SILTY CLAY
CLAYEY SILT
SILT
SANDY SILTY CLAY
SANDY CLAYEY SILT
SANDY SILT
SANDY CLAY
SILTY CLAYEY SAND
SILTY SAND
CLAYEY SAND
SAND

GC2

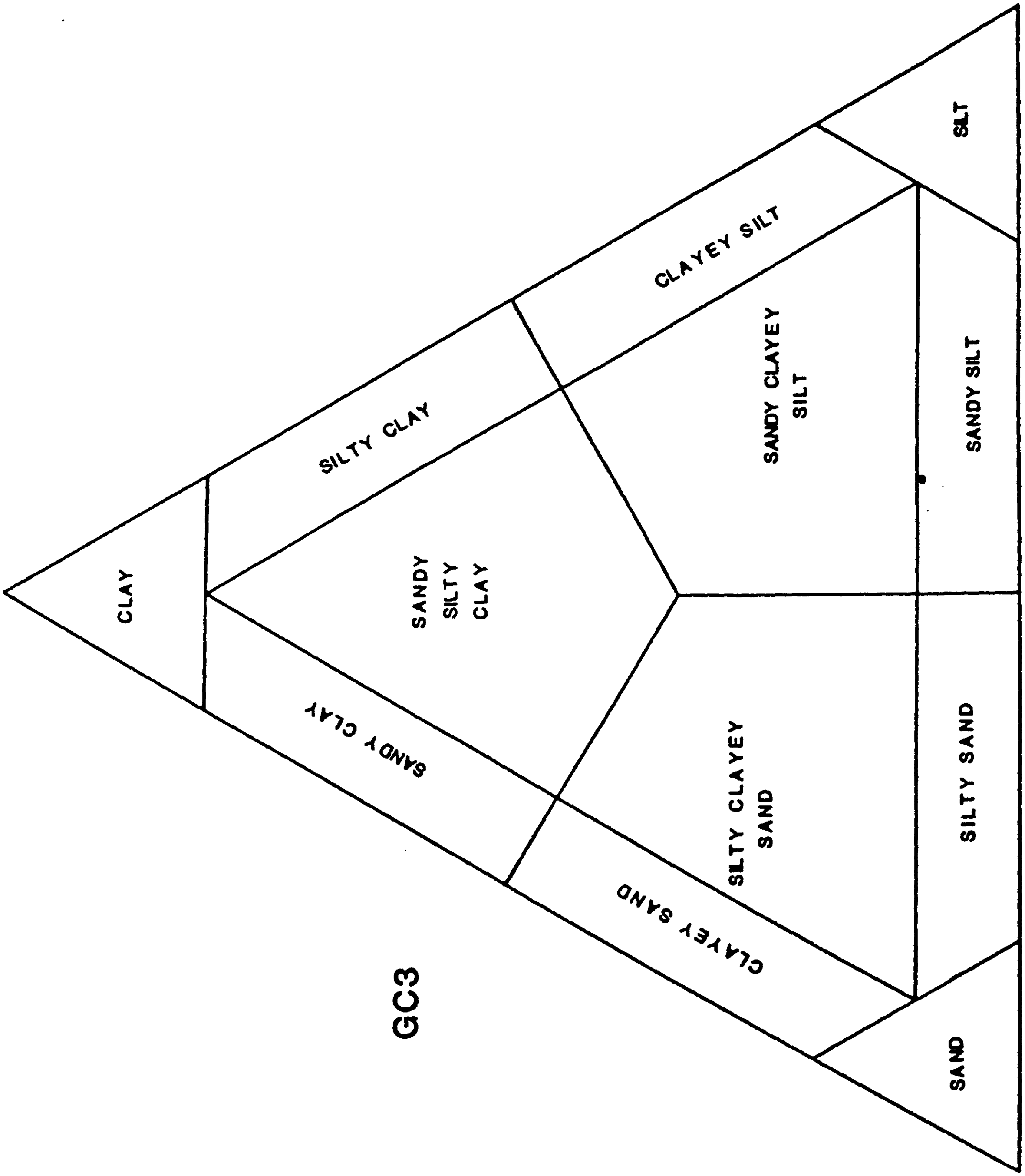
CLAY
SILTY CLAY
CLAYEY SILT
SILT
SANDY SILTY CLAY
SANDY CLAYEY SILT
SANDY SILT
SANDY CLAY
SILTY CLAYEY SAND
SILTY SAND
CLAYEY SAND
SAND

GC3

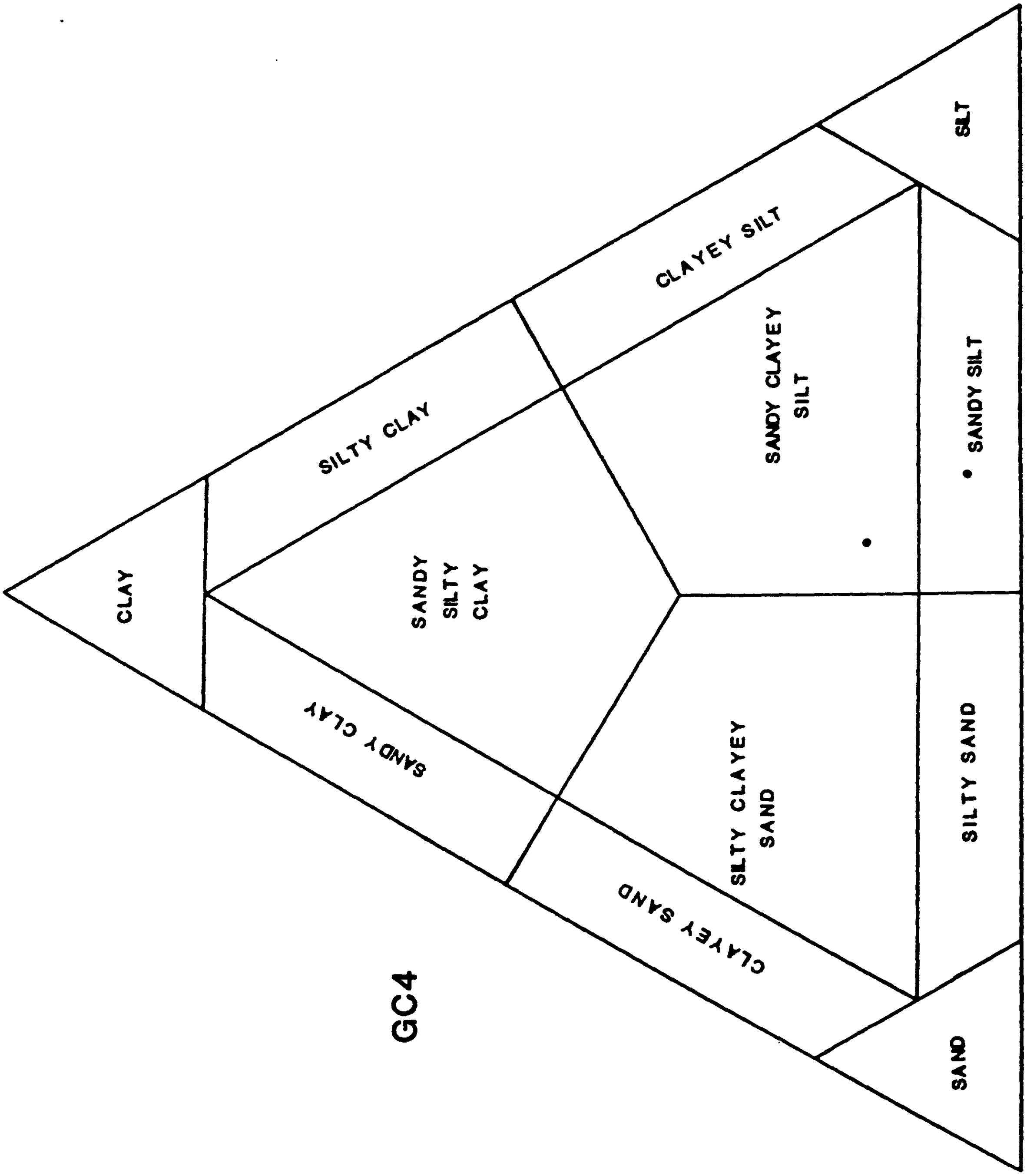
CLAY
SILTY CLAY
CLAYEY SILT
SILT
SANDY SILTY CLAY
SANDY CLAYEY SILT
SANDY SILT
SANDY CLAY
SILTY CLAYEY SAND
SILTY SAND
CLAYEY SAND
SAND

GC4

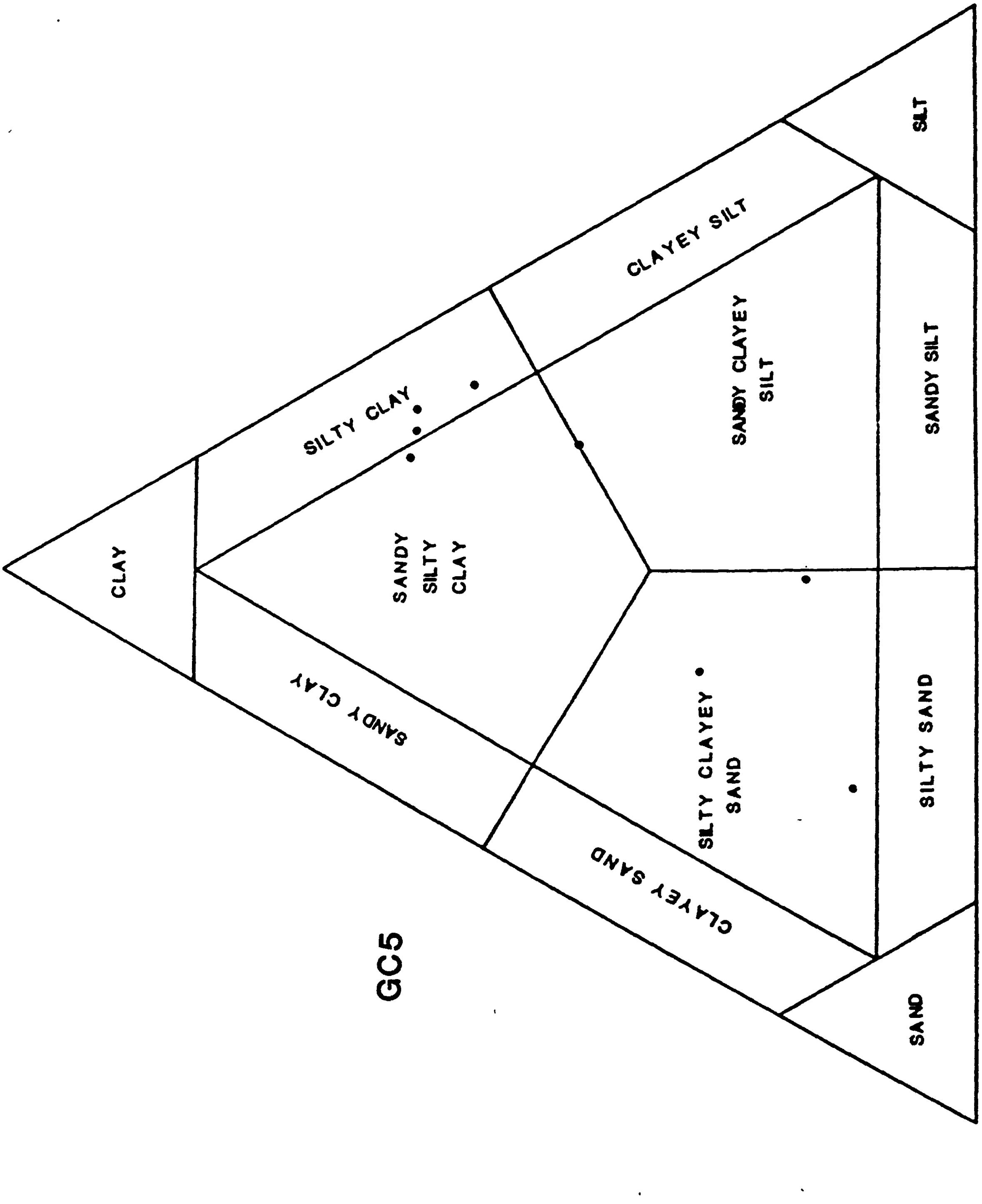
CLAY
SILTY CLAY
CLAYEY SILT
SILT
SANDY SILTY CLAY
SANDY CLAYEY SILT
SANDY SILT
SANDY CLAY
SILTY CLAYEY SAND
SILTY SAND
CLAYEY SAND
SAND

GC5

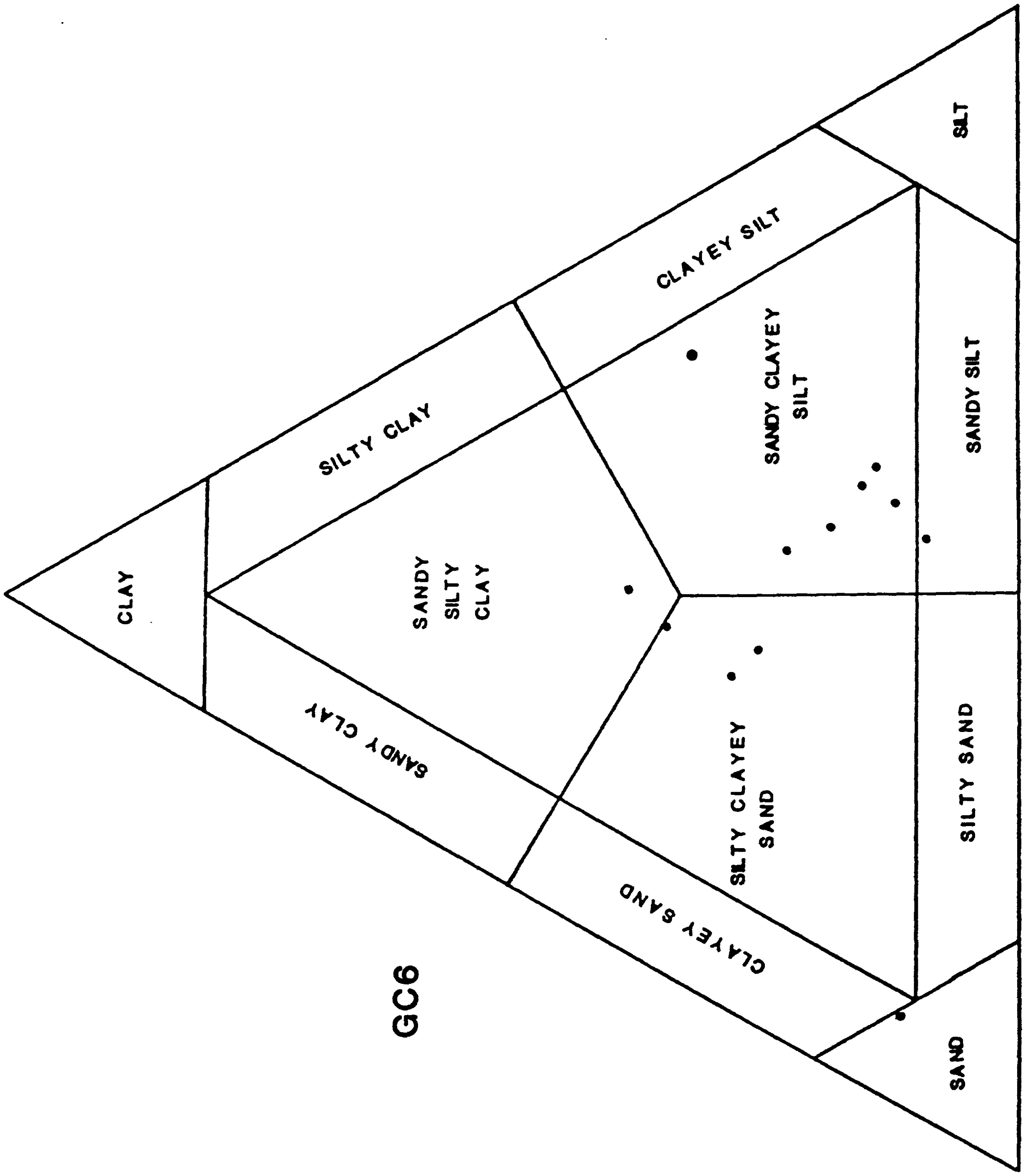
CLAY
SILTY CLAY
SANDY CLAY
SANDY SILTY CLAY
CLAYEY SILT
SANDY CLAYEY SILT
SILTY CLAYEY SAND
CLAYEY SAND
SILT
SANDY SILT
SILTY SAND
SAND

GC6

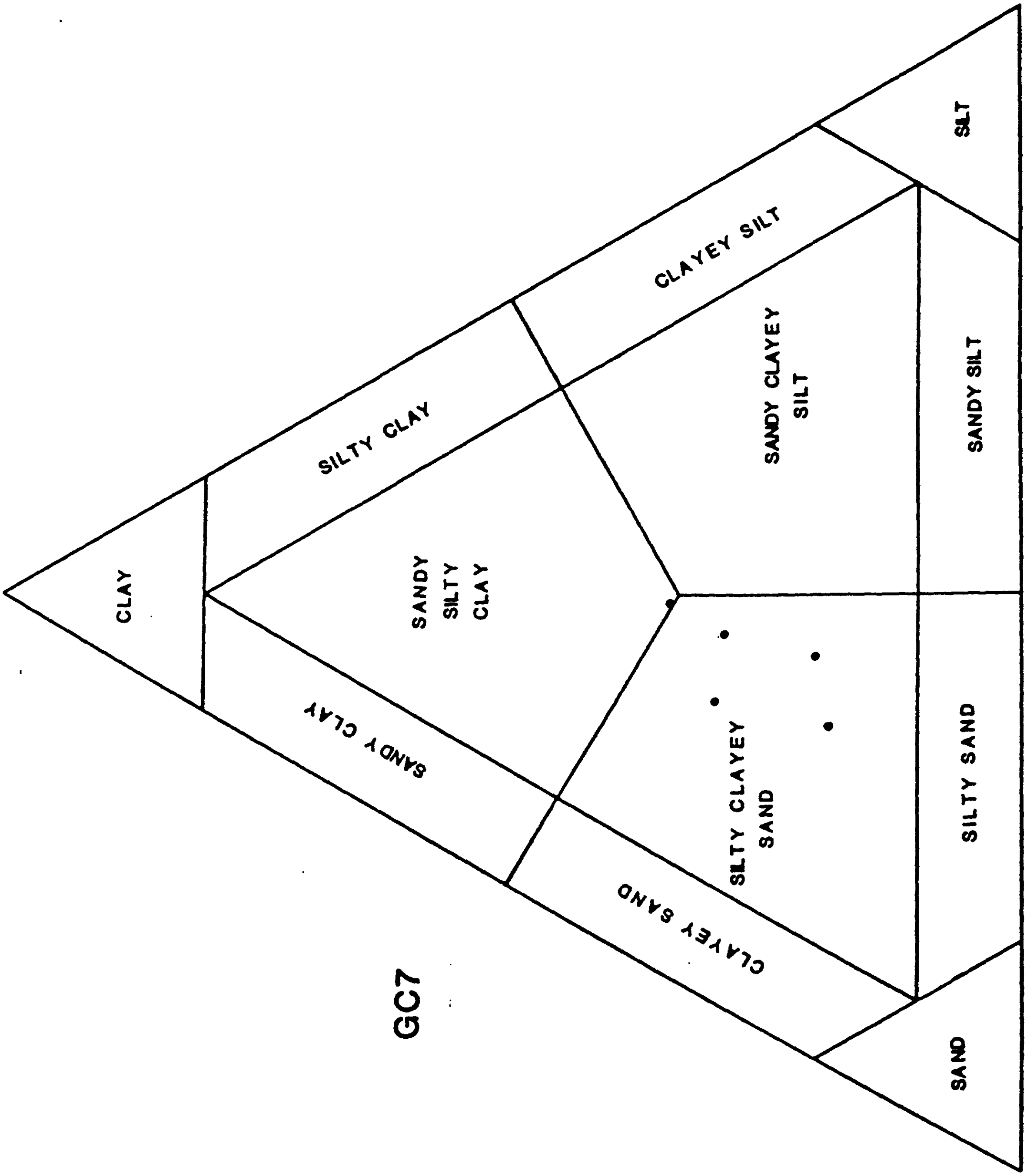
CLAY
SILTY CLAY
CLAYEY SILT
SILT
SANDY SILTY CLAY
SANDY CLAYEY SILT
SANDY SILT
SANDY CLAY
SILTY CLAYEY SAND
SILTY SAND
CLAYEY SAND
SAND

GC7

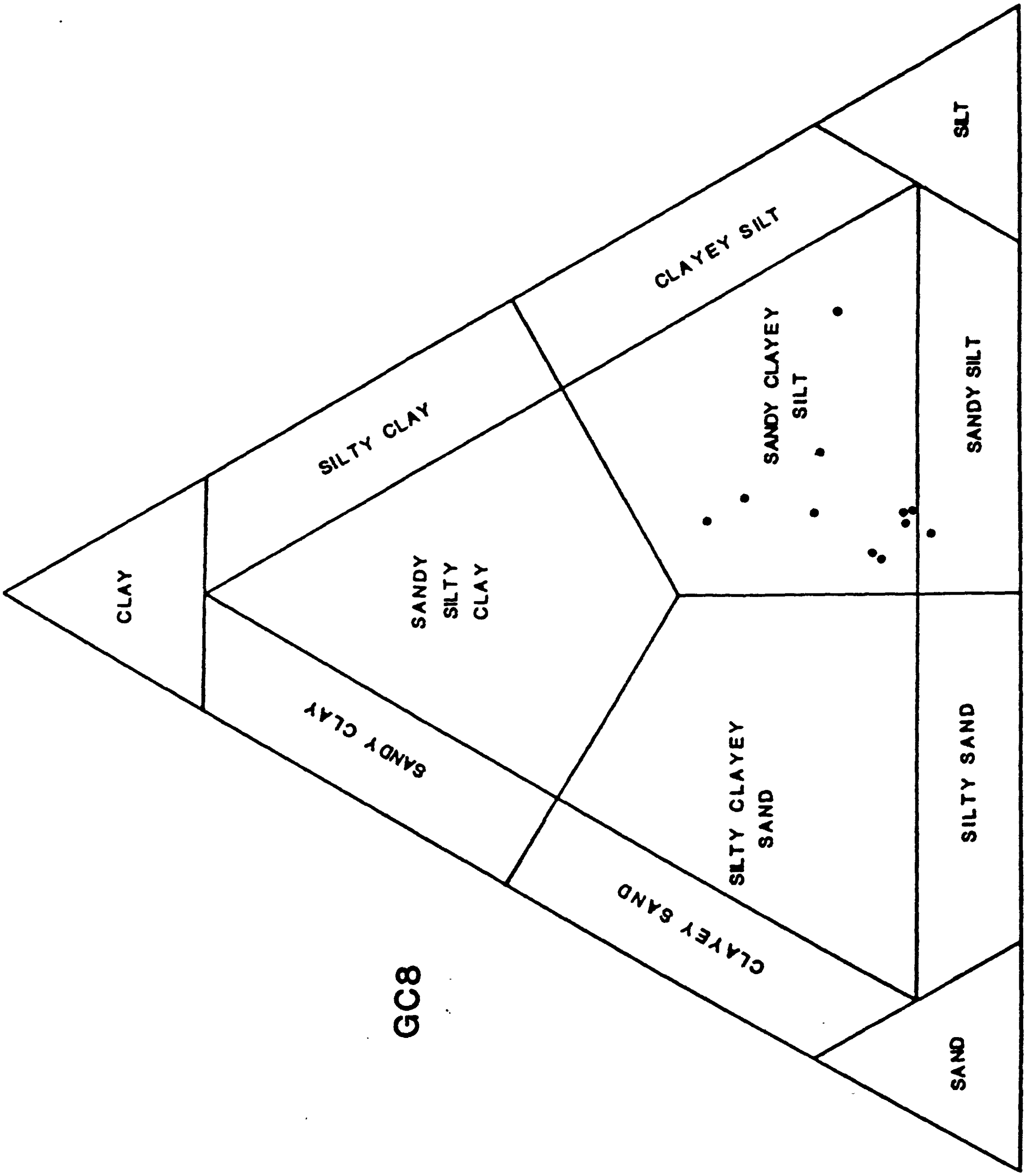
GC8
CLAY
SILTY CLAY
CLAYEY SILT
SILT
SANDY SILTY CLAY
SANDY CLAYEY SILT
SANDY SILT
SANDY CLAY
SILTY CLAYEY SAND
SILTY SAND
CLAYEY SAND
SAND

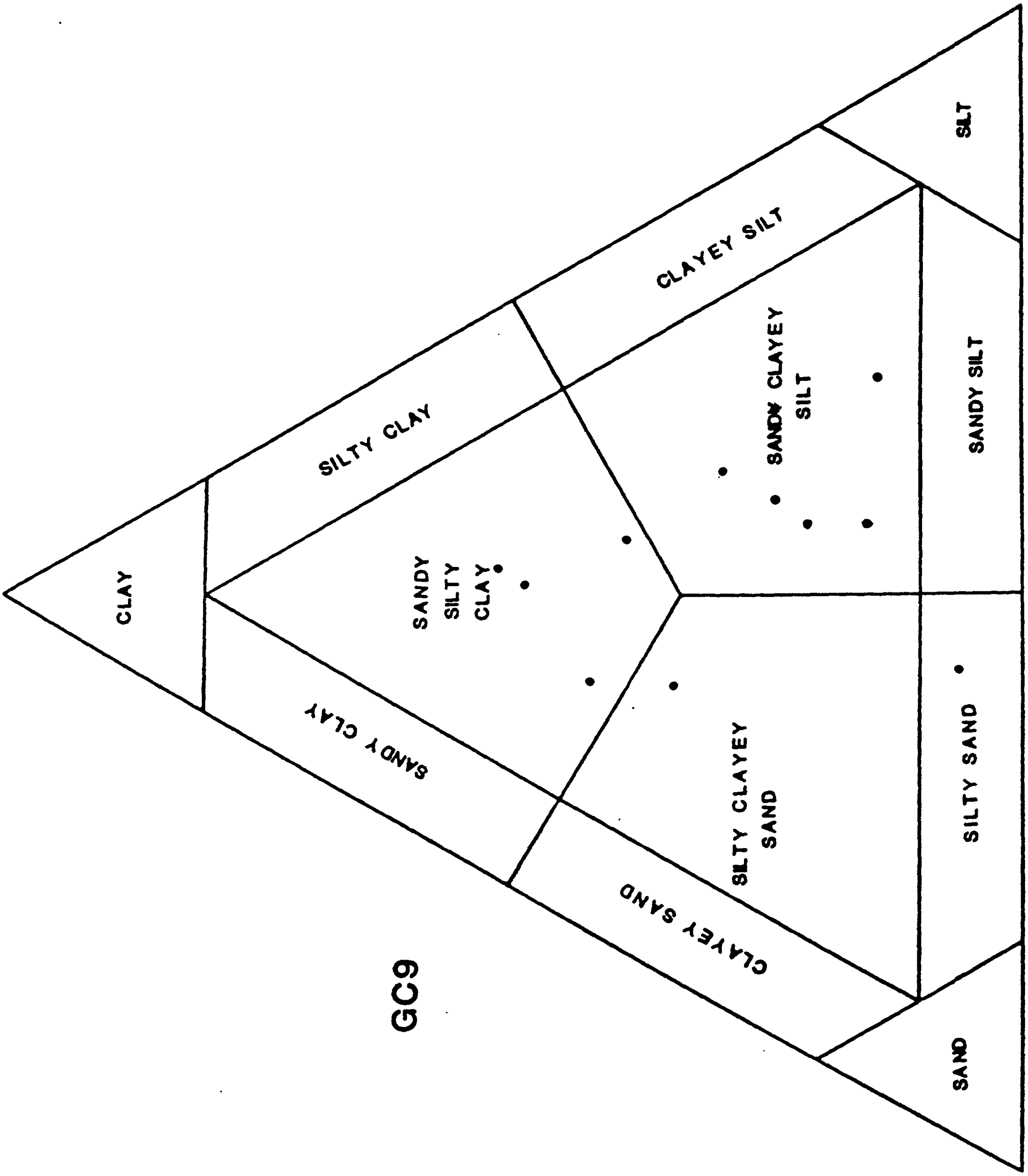
CLAY
SILTY CLAY
CLAYEY SILT
SILT
SANDY SILTY CLAY
SANDY CLAYEY SILT
SANDY SILT
SANDY CLAY
SILTY CLAYEY SAND
SILTY SAND
CLAYEY SAND
SAND

GC9

APPENDIX 2-3: CONSOLIDATION TEST PLOTS.

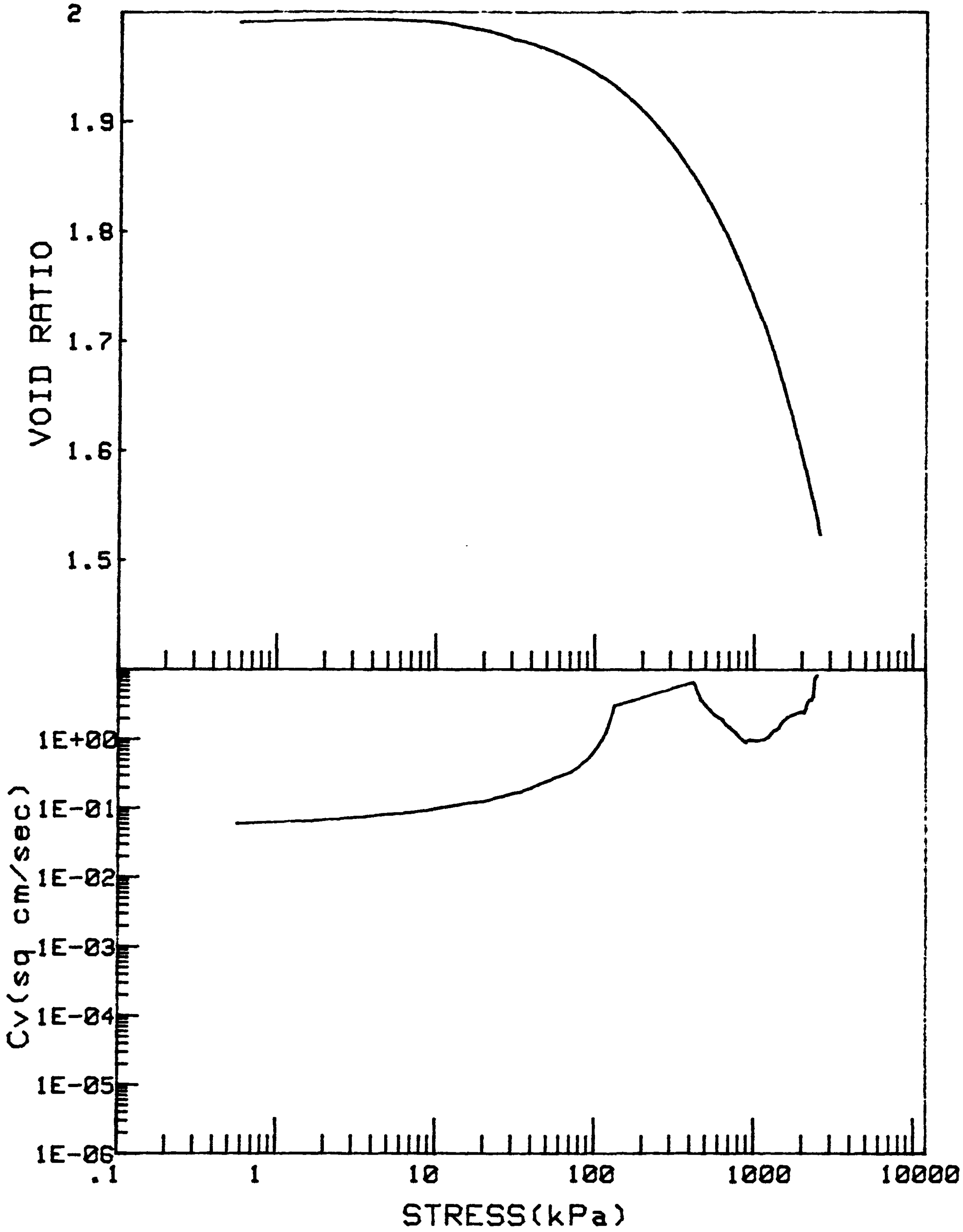

L9-84-CP		INCREMENT (cm)	156-158
CORE NO.	GC8	TEST NO.	CE180

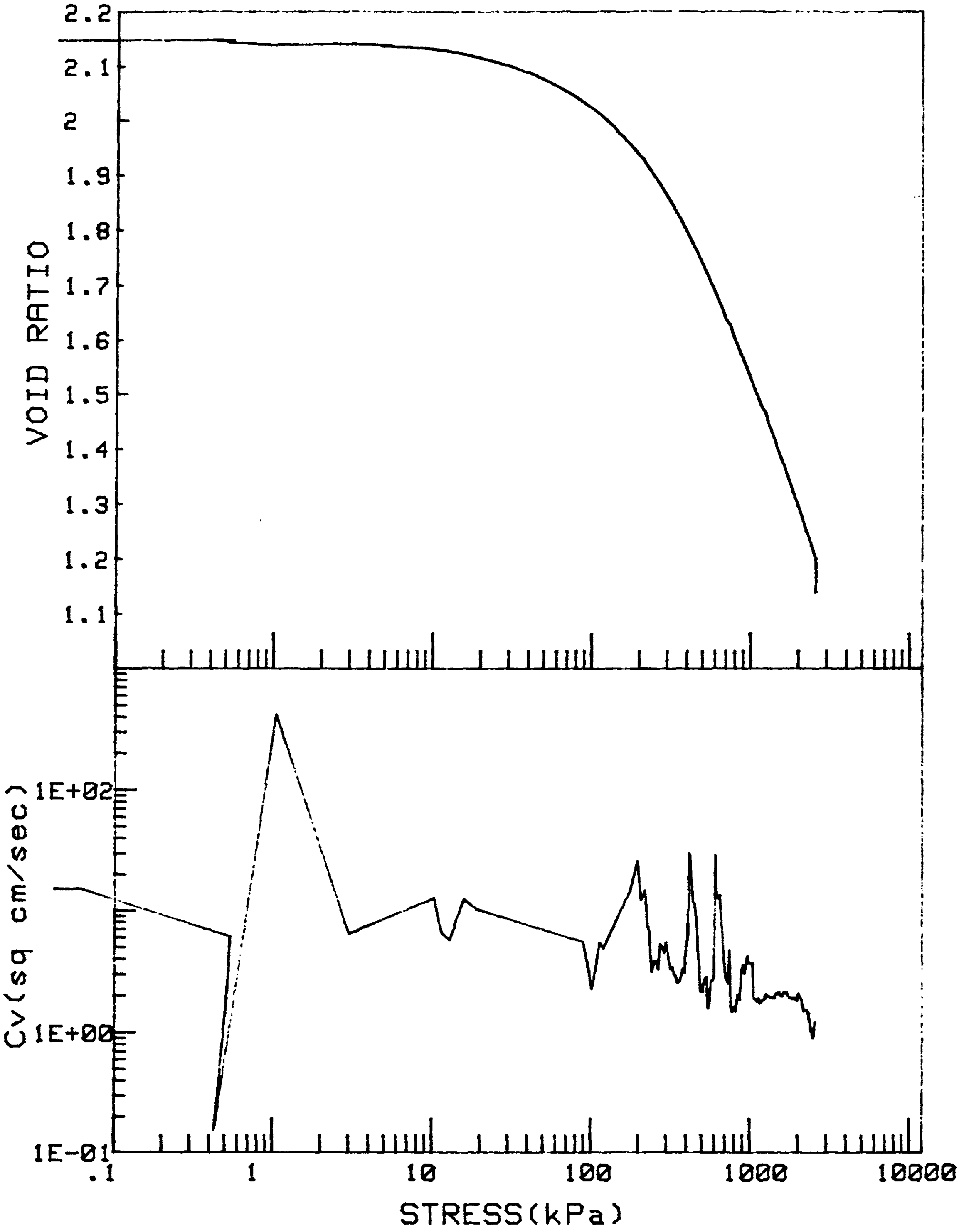

HORIZON GUYOT		INCREMENT (cm)	100-105
CORE NO.	GC 3	TEST NO.	CE145

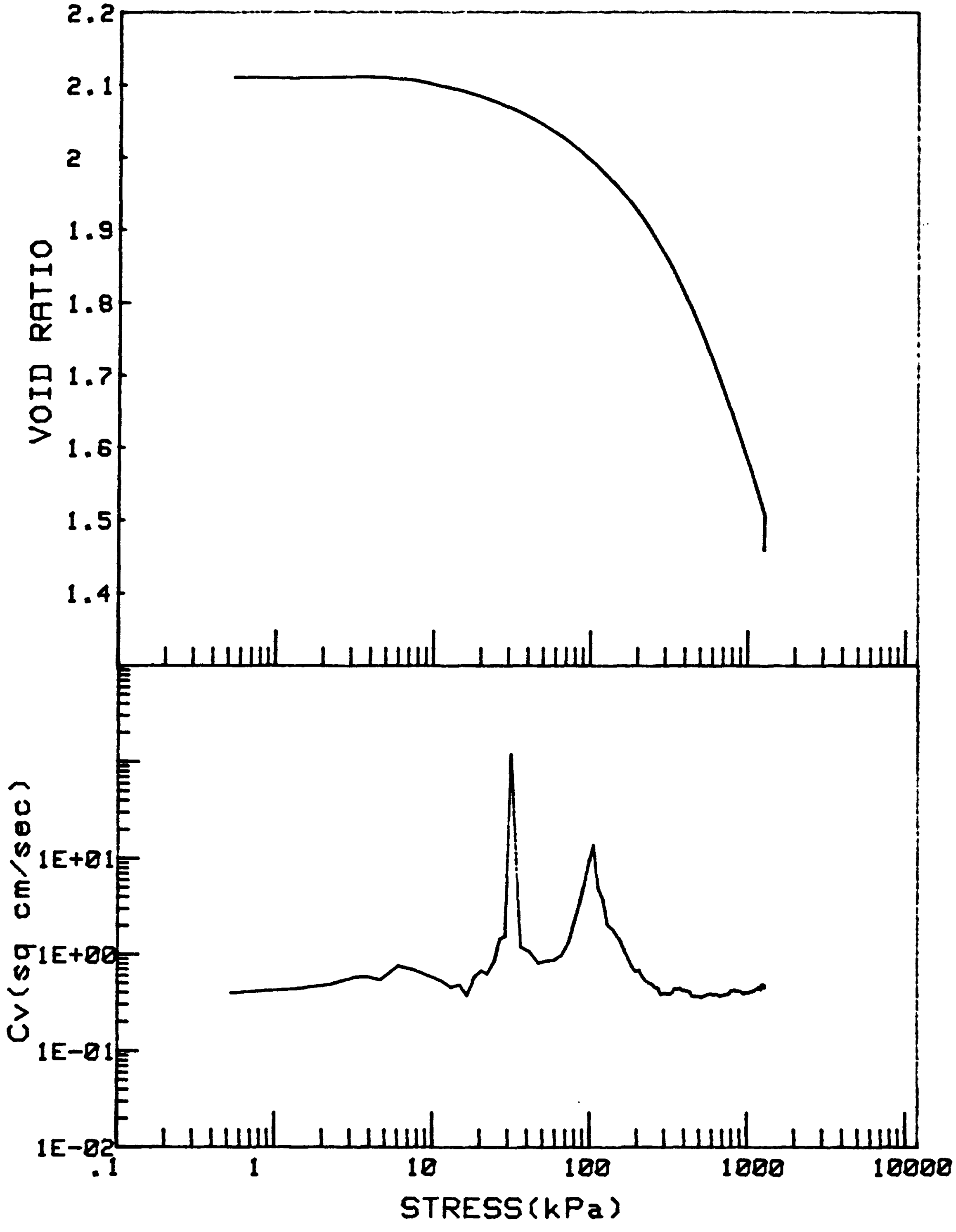

L9-84-CP		INCREMENT (cm)	115-120
CORE NO.	GC8	TEST NO.	CE175

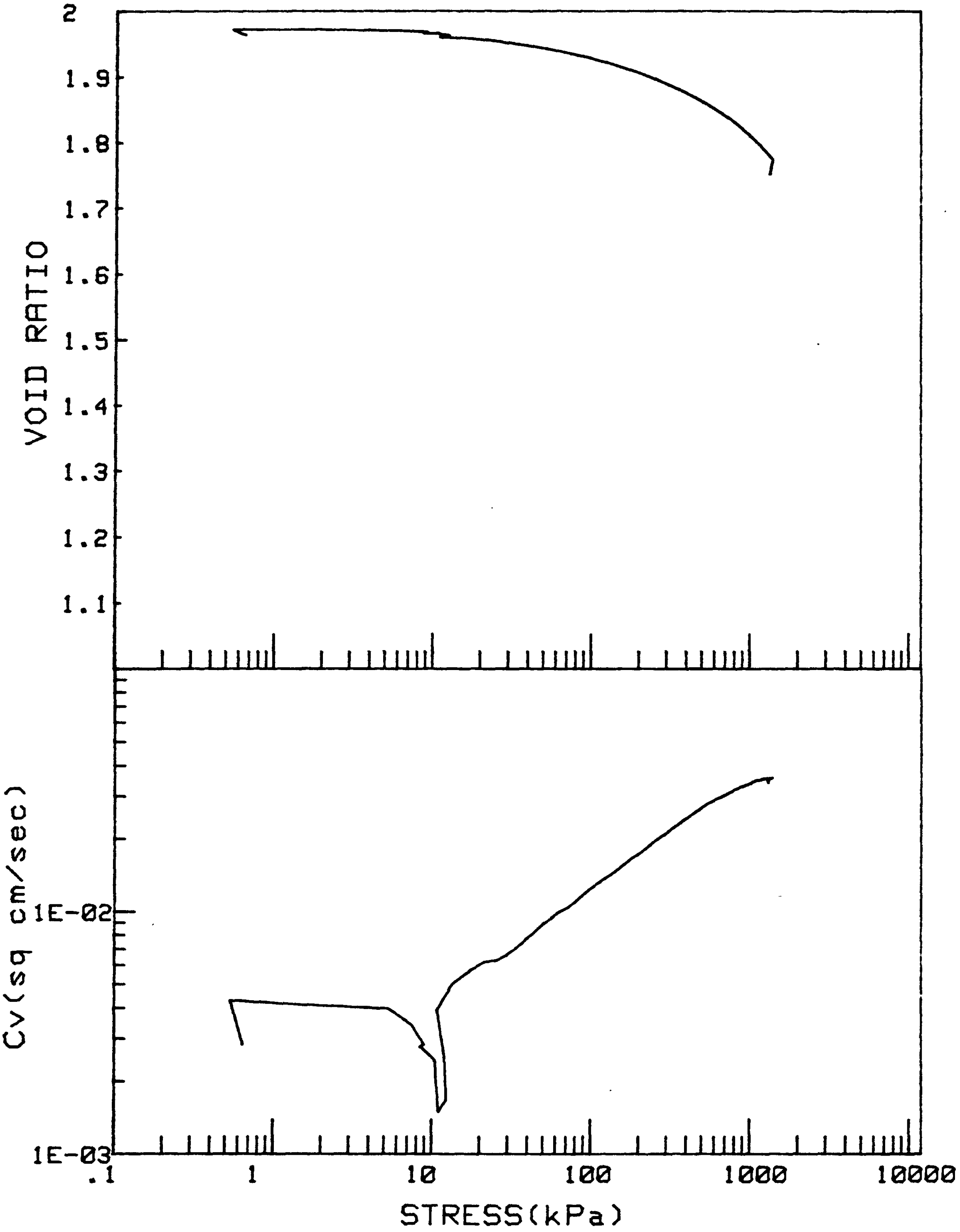

L9-84-CP		INCREMENT (cm)	200-205
CORE NO.	GC-8	TEST NO.	CE176

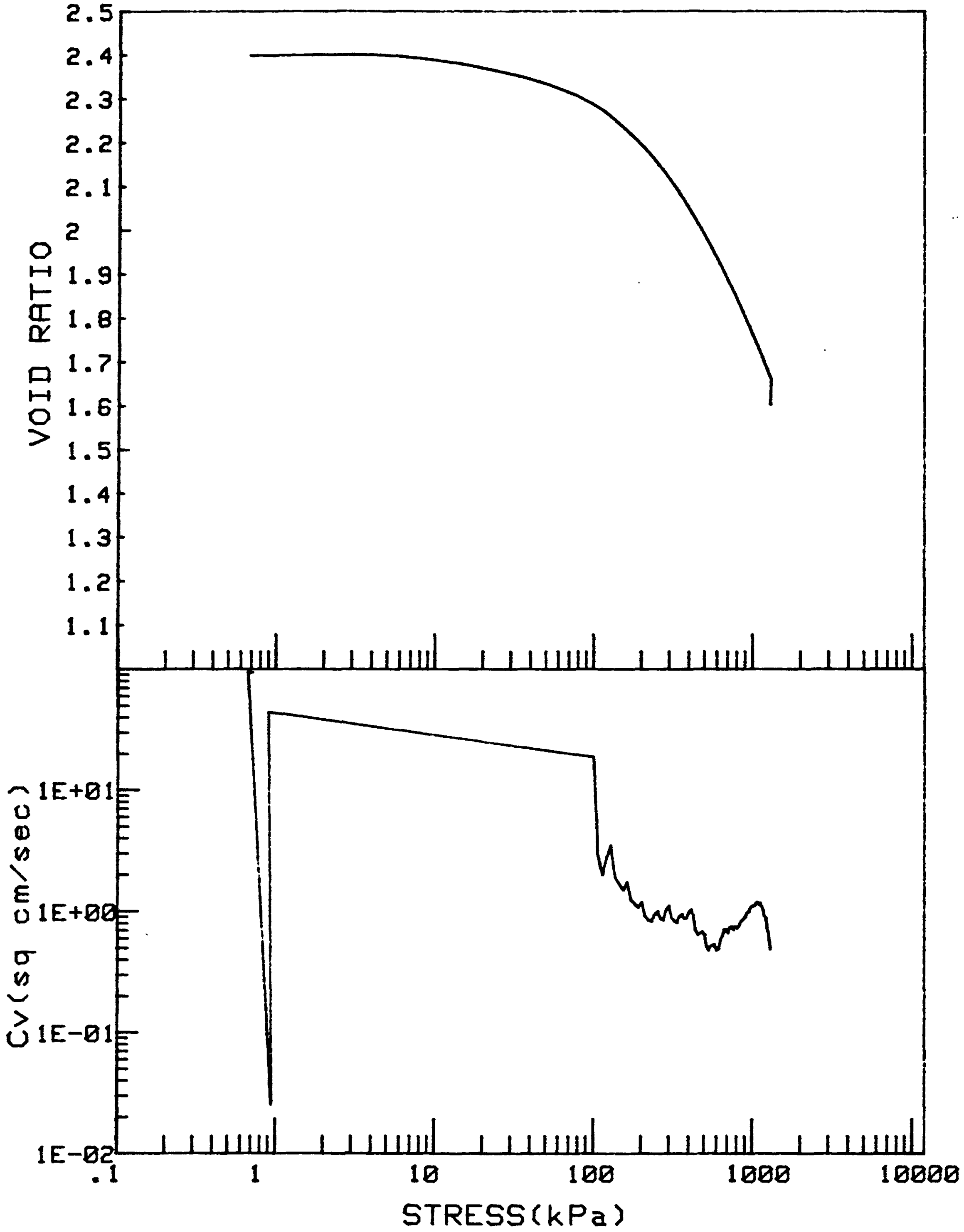

L9-84-CP		INCREMENT (cm)	90-95
CORE NO.	GC7	TEST NO.	CE177

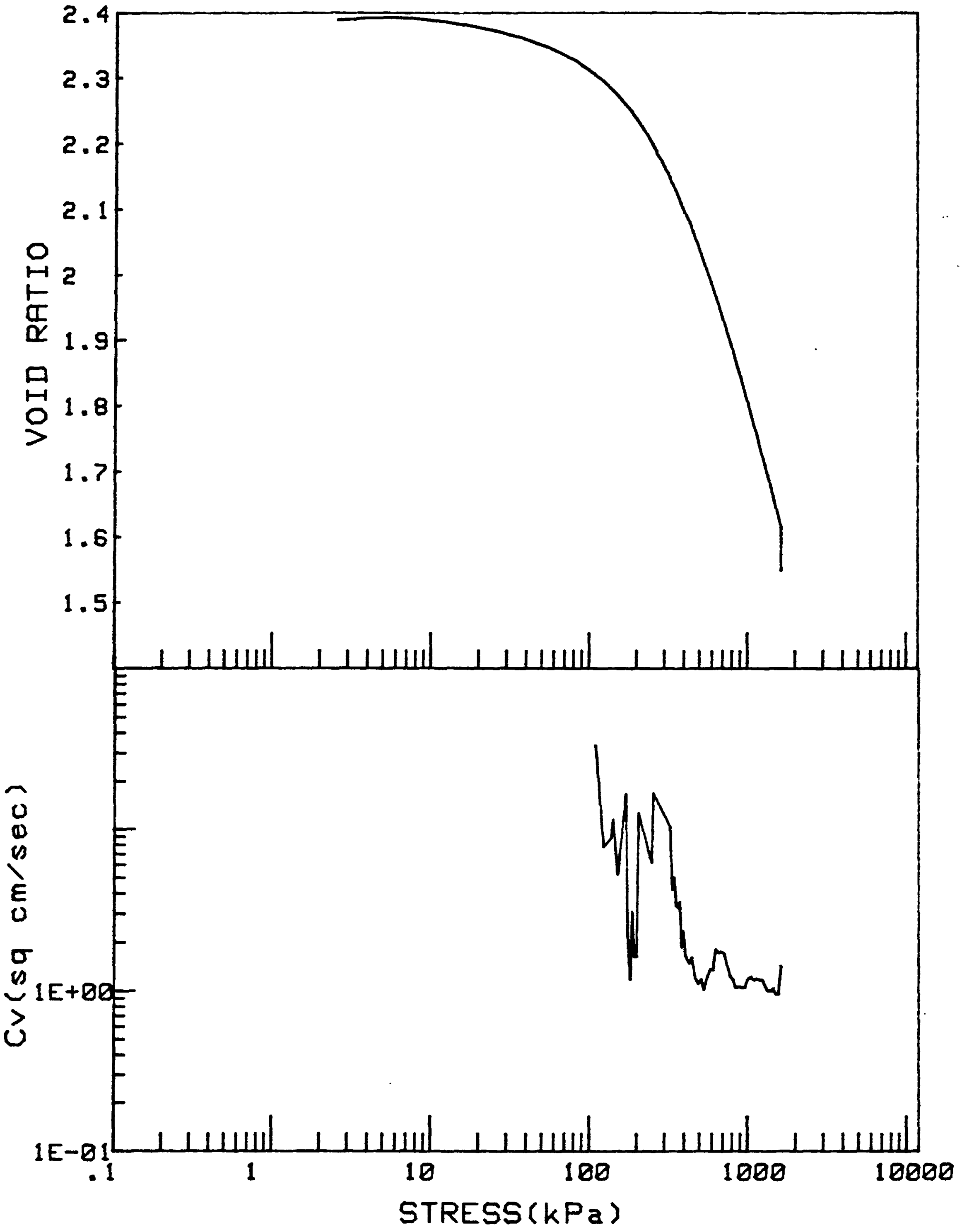

L9-84-CP		INCREMENT (cm)	170-175
CORE NO.	GC7	TEST NO.	CE178

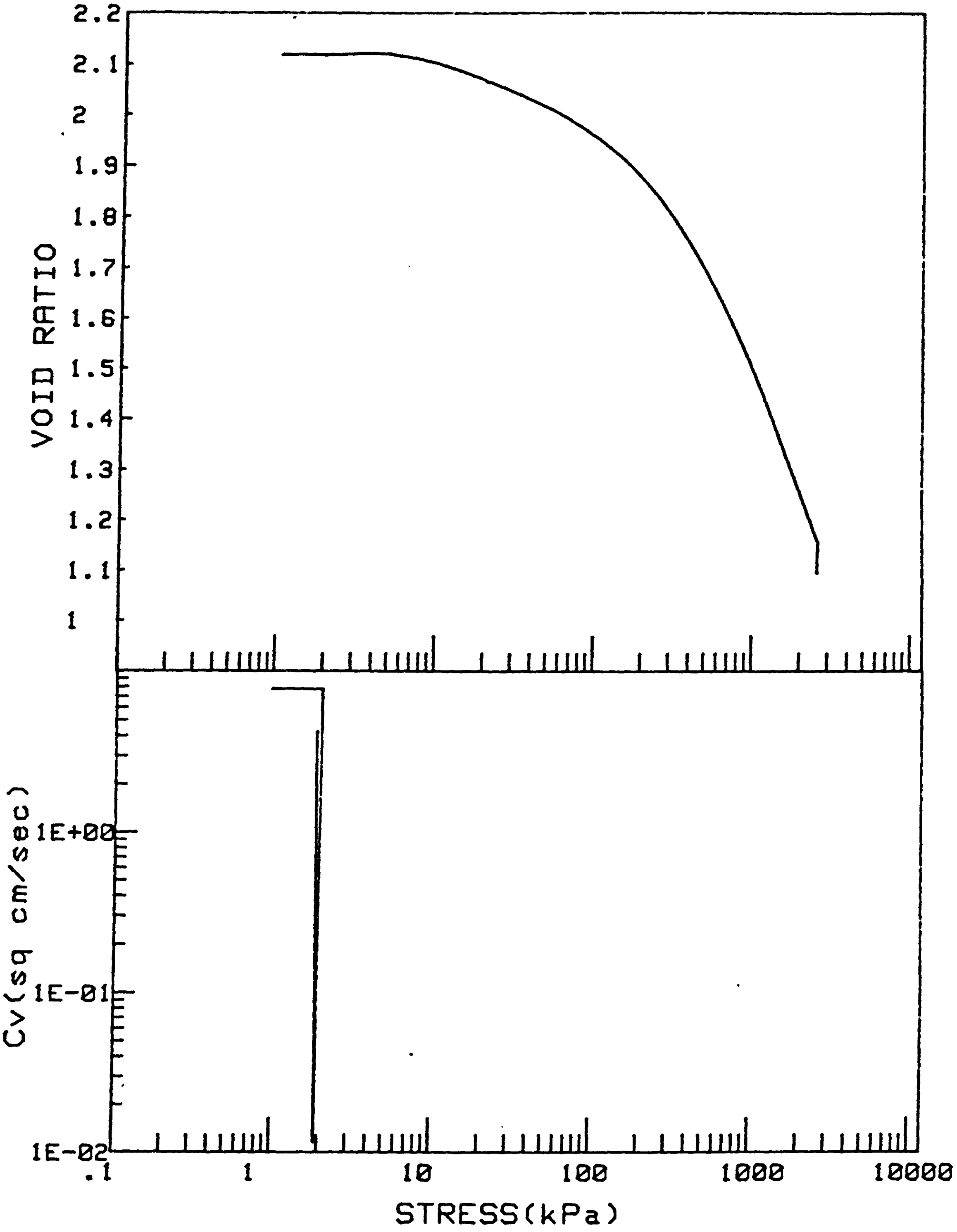

L9-84-CP		INCREMENT (cm)	122-124
CORE NO.	GC4	TEST NO.	CE179

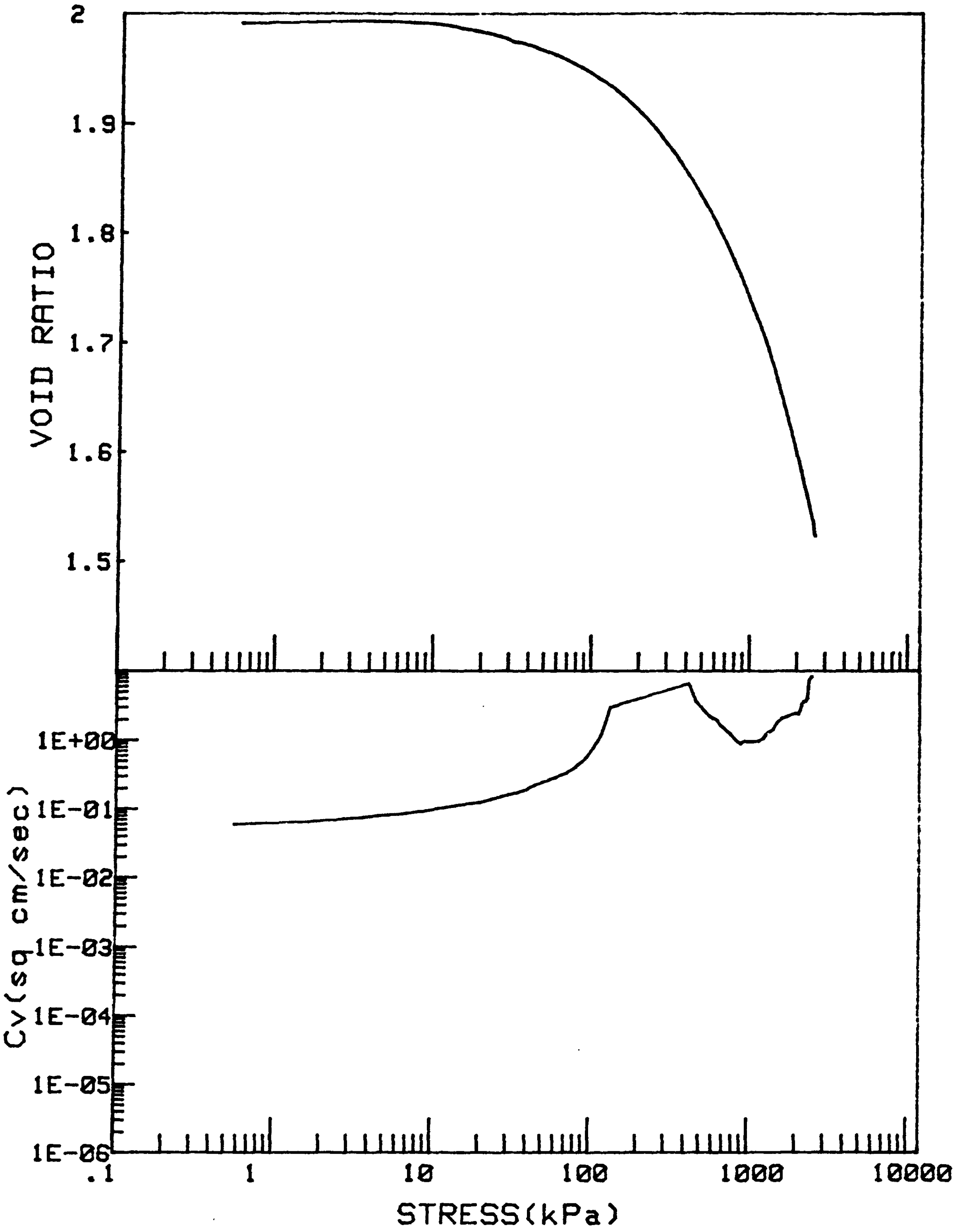

L9-84-CP		INCREMENT (cm)	156-158
CORE NO.	GC8	TEST NO.	CE180

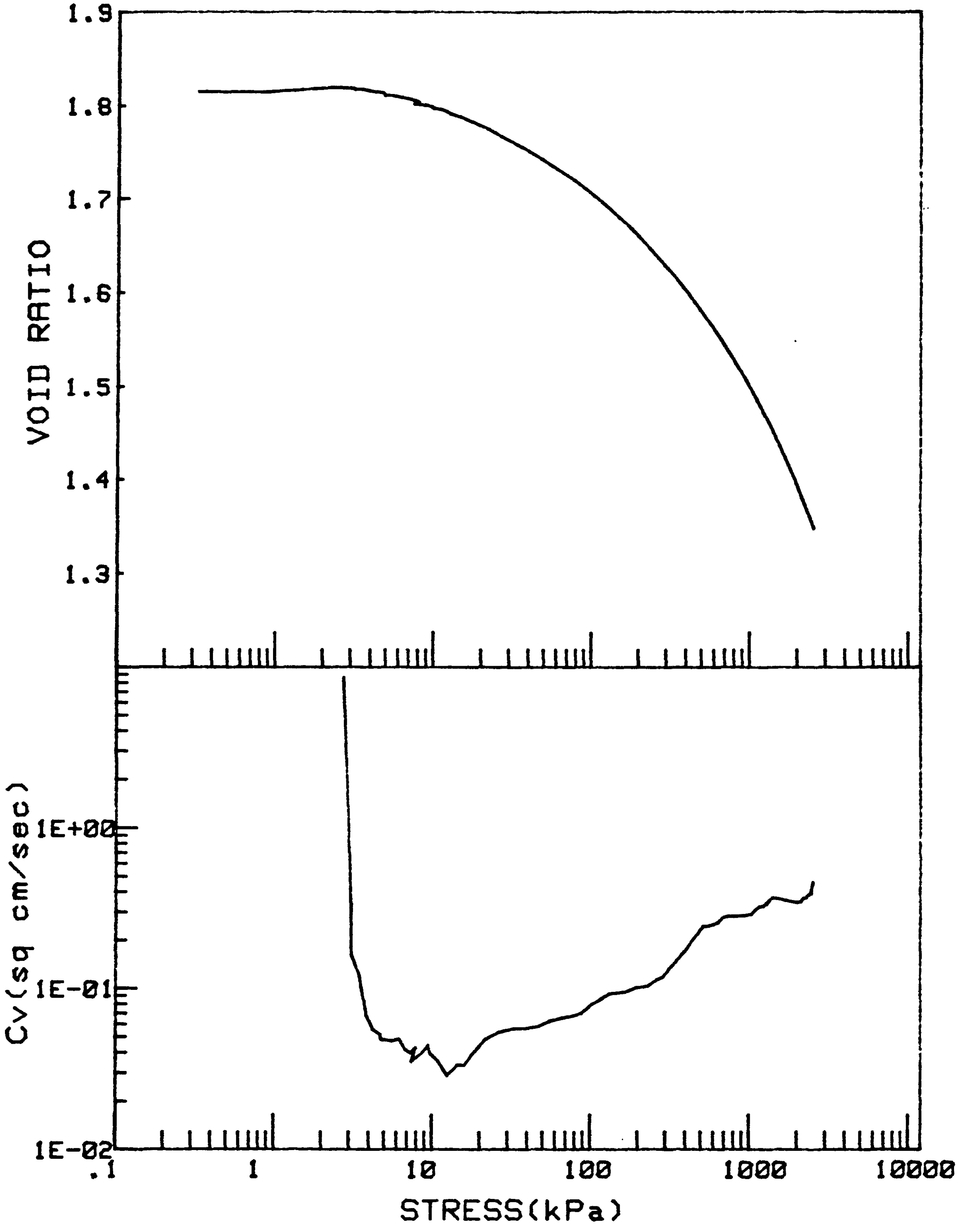

L9-84-CP		INCREMENT (cm)	261-263
CORE NO.	GC7	TEST NO.	CE181

APPENDIX 2-4: STATIC TRIAXIAL TEST PLOTS.

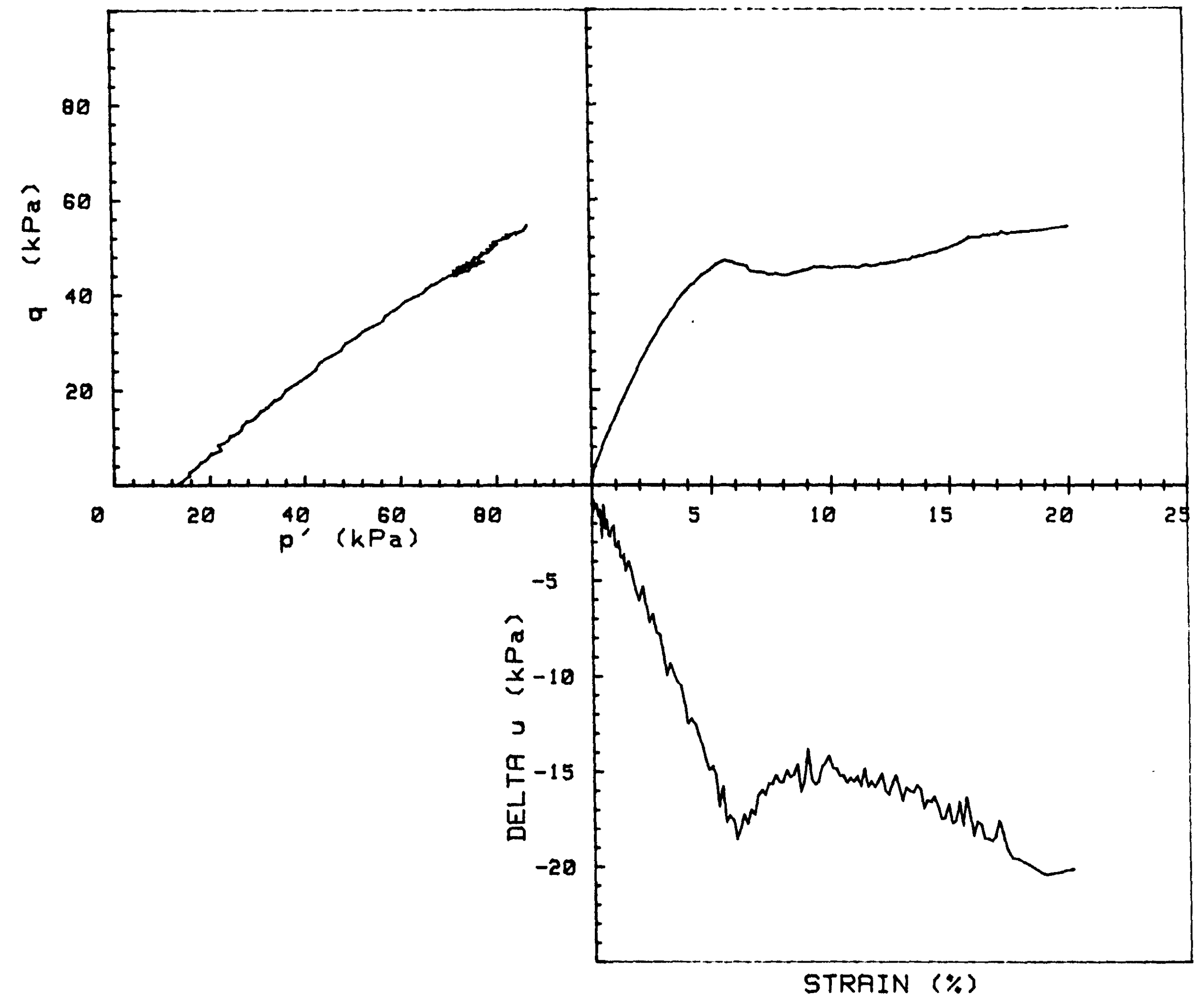

L9-84-CP		INCREMENT (cm)	273-280
CORE NO.	GC7	TEST NO.	TE280
SIG1c´(kPa)	12.4		
SIG3c´(kPa)	12.4		
INDUCED OCR	1.0		

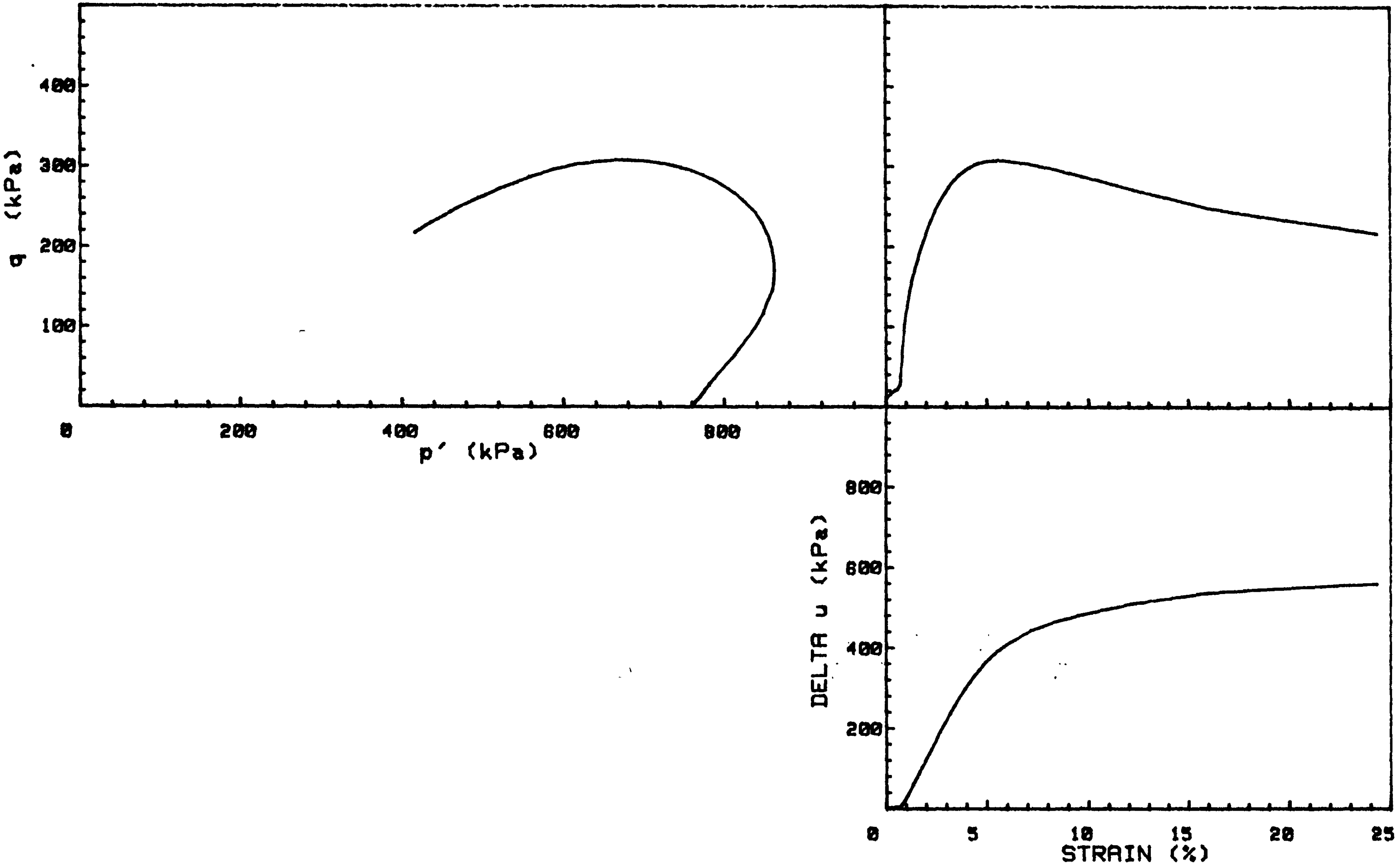

L9-84-CP		INCREMENT (cm)	95-105
CORE NO.	GC8	TEST NO.	TH6

SIG1c′(kPa) 760.1
SIG3c′(kPa) 760.1
INDUCED OCR 1.0

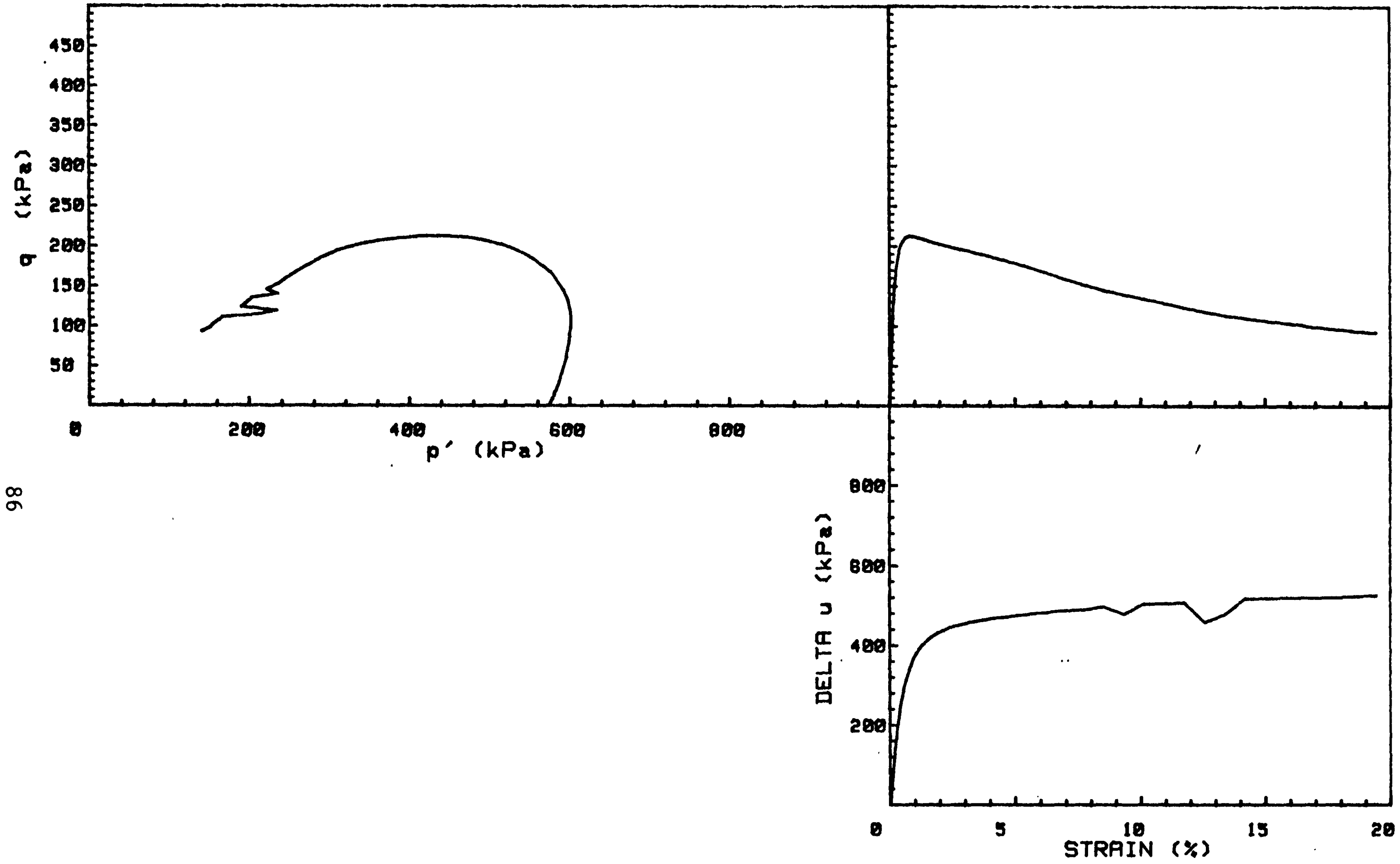

L9-84-CP		INCREMENT (cm)	105-115
CORE NO.	GC8	TEST NO.	TH7
SIG1c′(kPa)	574.1		
SIG3c′(kPa)	574.1		
INDUCED OCR	1.0		

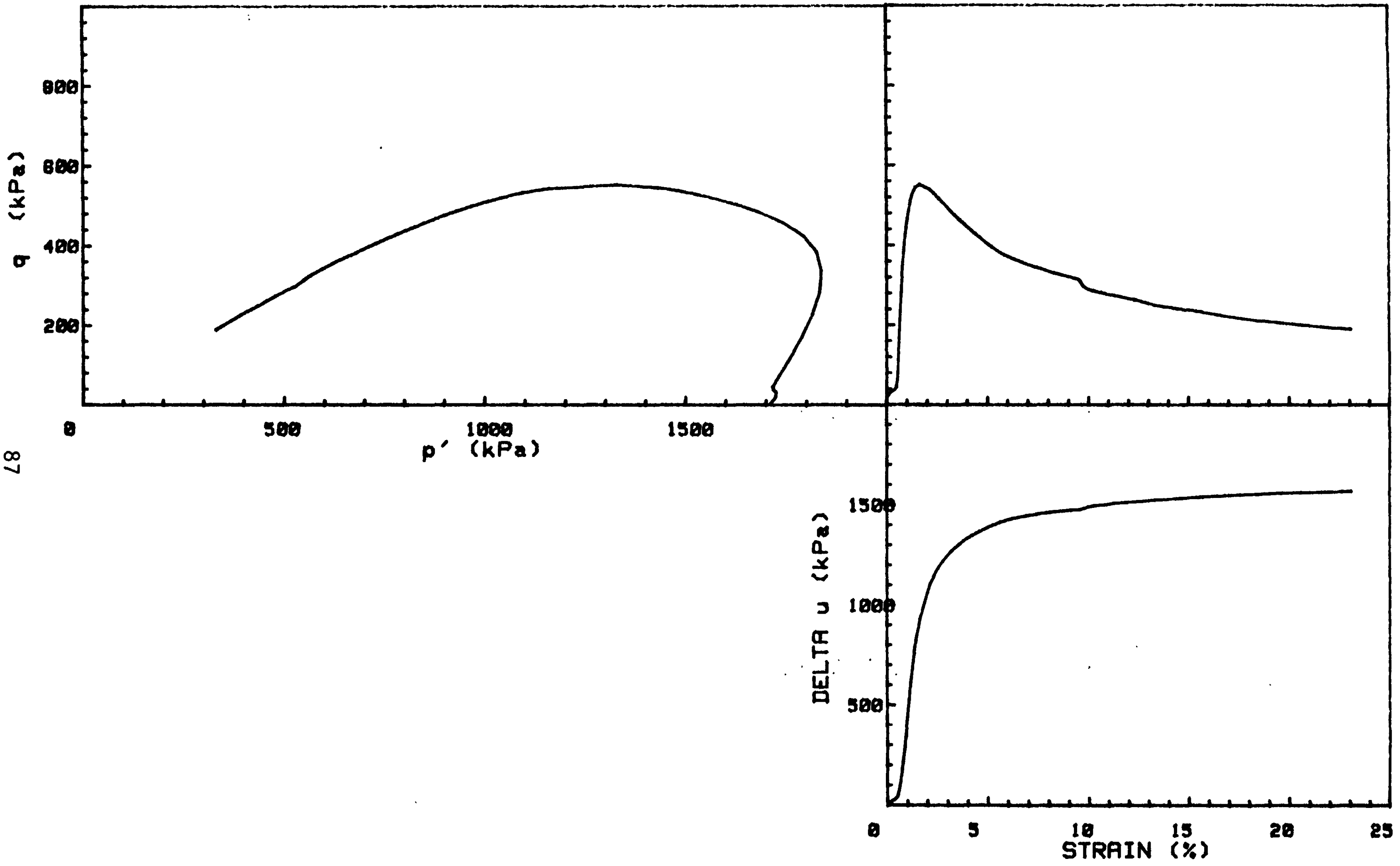

L9-84-CP		INCREMENT (cm)	121-129
CORE NO.	GC8	TEST NO.	TH8

SIG1c′(kPa) 1712.2
SIG3c′(kPa) 1712.2
INDUCED OCR 1.0

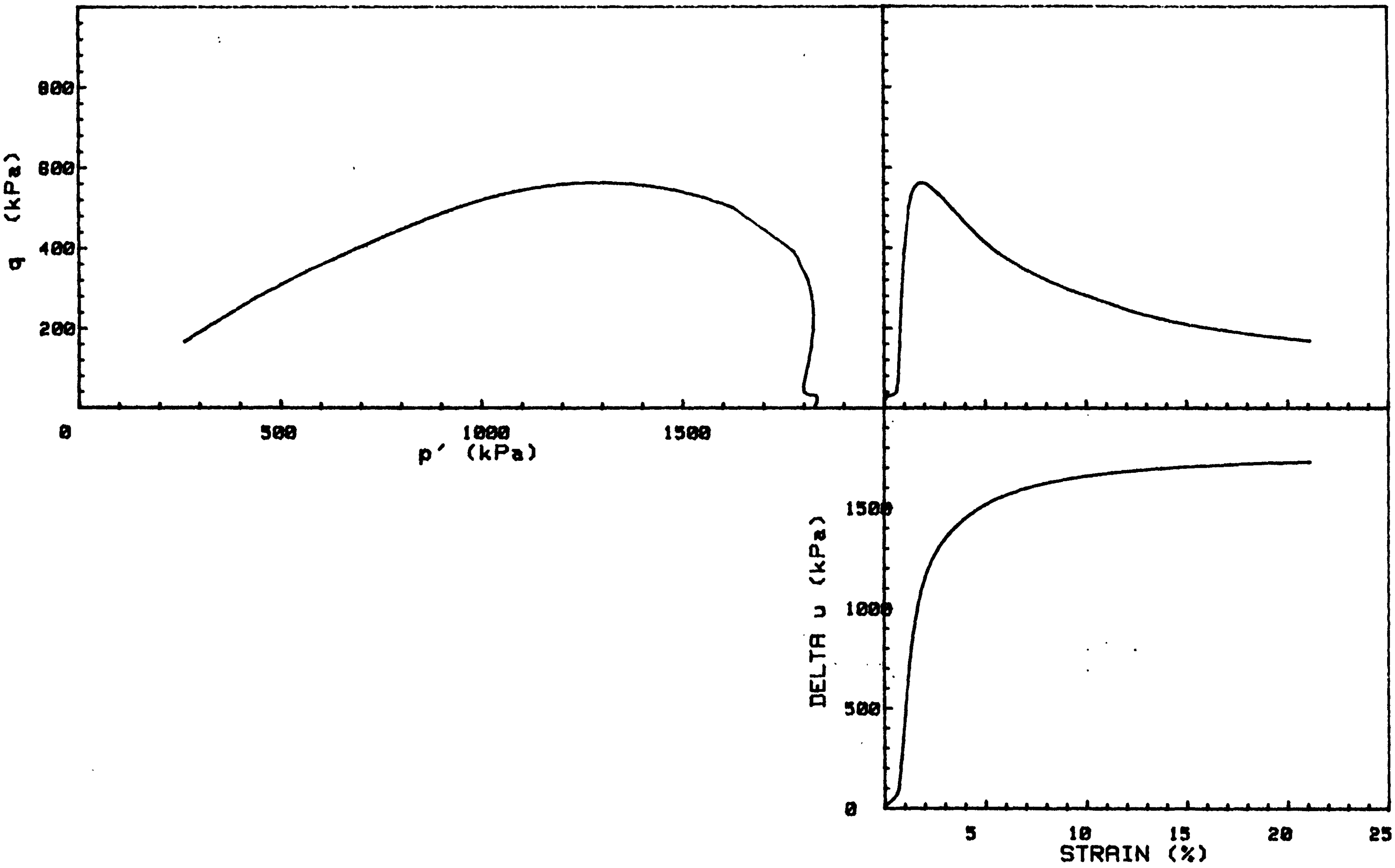

L9-84-CP		INCREMENT (cm)	112-120
CORE NO.	GC4	TEST NO.	TH9
SIG1c'(kPa)	1828.2		
SIG3c'(kPa)	1828.2		
INDUCED OCR	1.0		

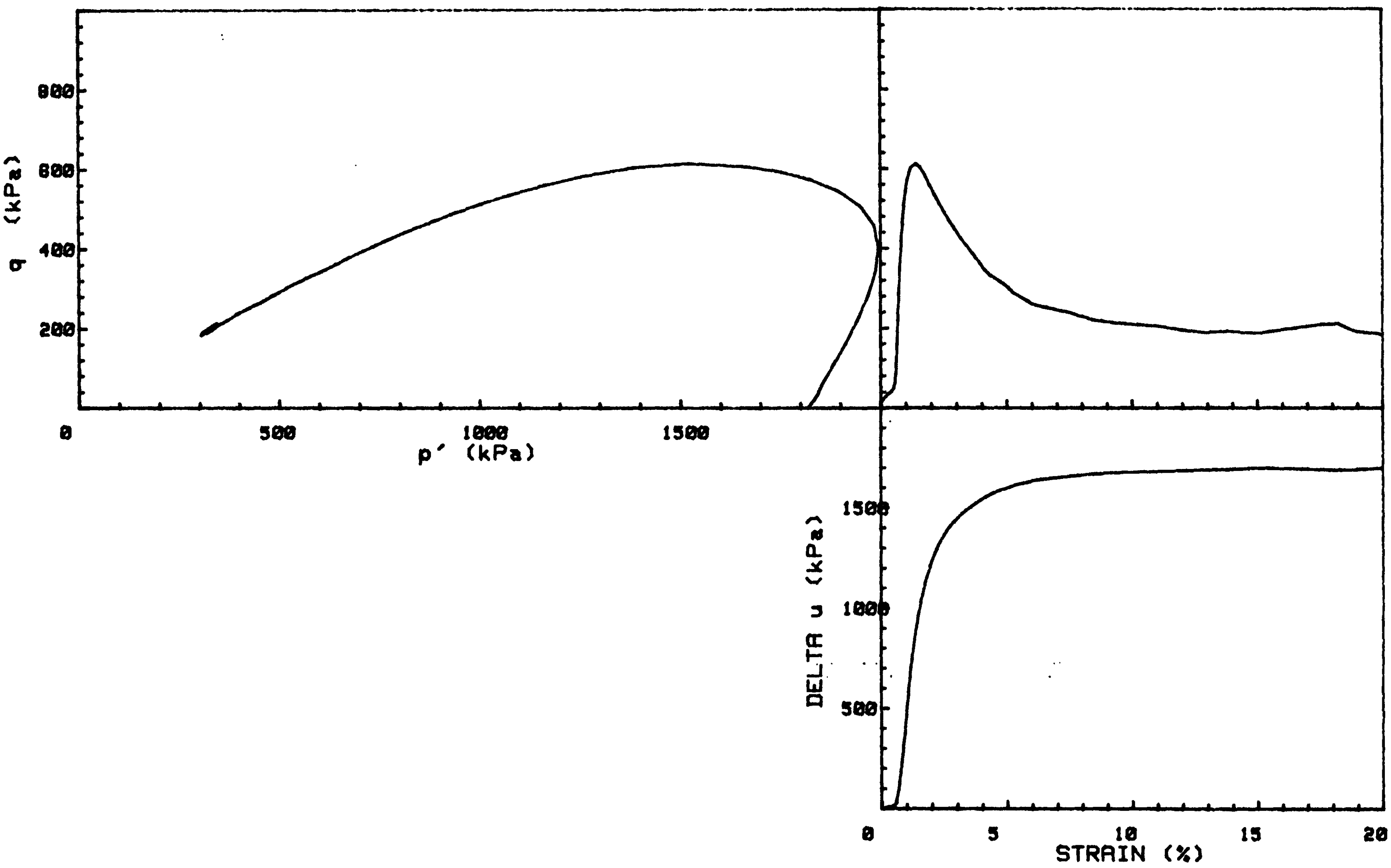

L9-84-CP		INCREMENT (cm)	193-200
CORE NO.	GC-8	TEST NO.	TH10

SIG1c′(kPa) 1818.4
SIG3c′(kPa) 1818.4
INDUCED OCR 1.0

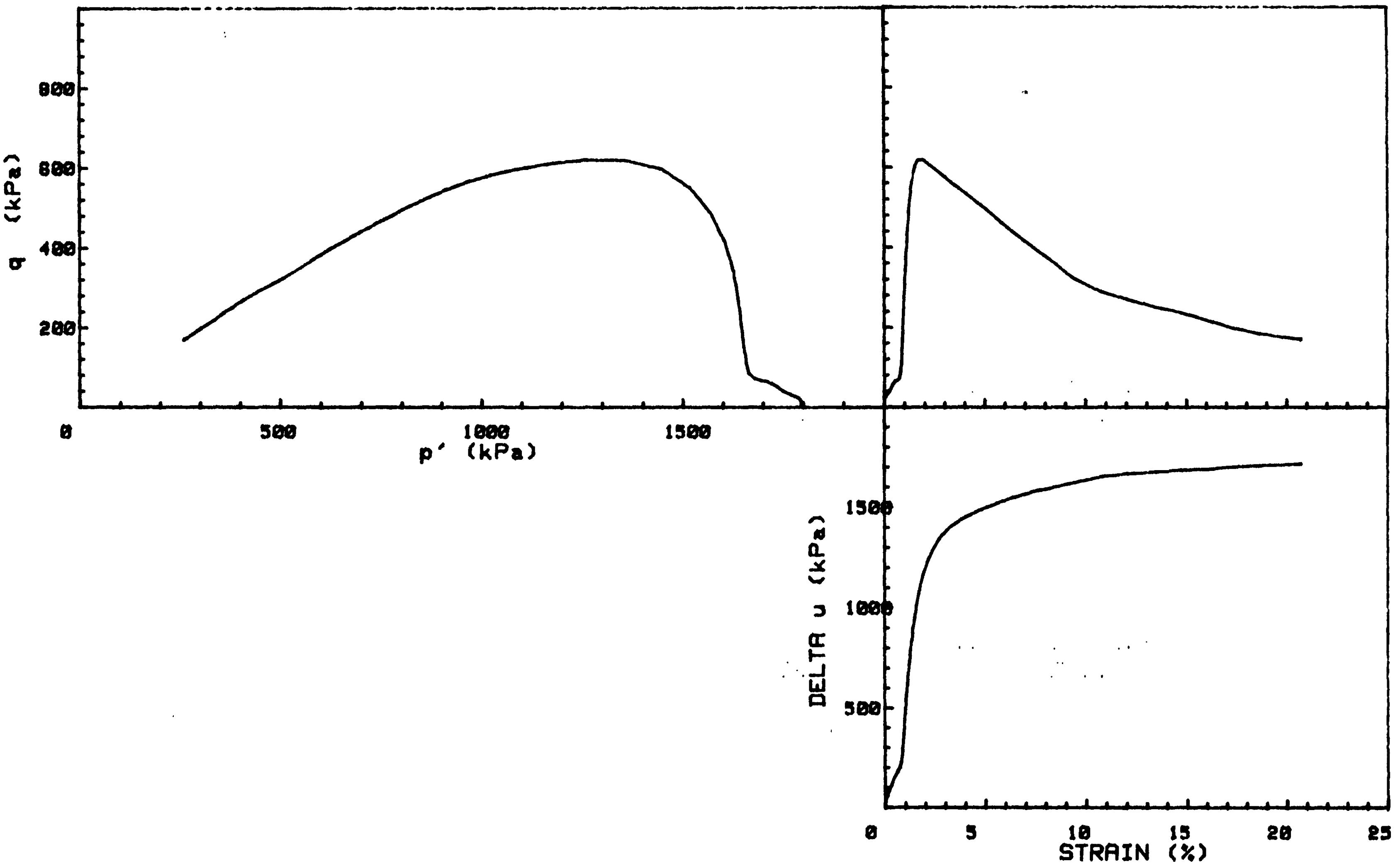

L9-84-CP		INCREMENT (cm)	264-273
CORE NO.	GC-7	TEST NO.	TH11
SIG1c′(kPa)	1807.0		
SIG3c′(kPa)	1807.0		
INDUCED OCR	1.0		

APPENDIX 2-5: CYCLIC TRIAXIAL TEST PLOTS.

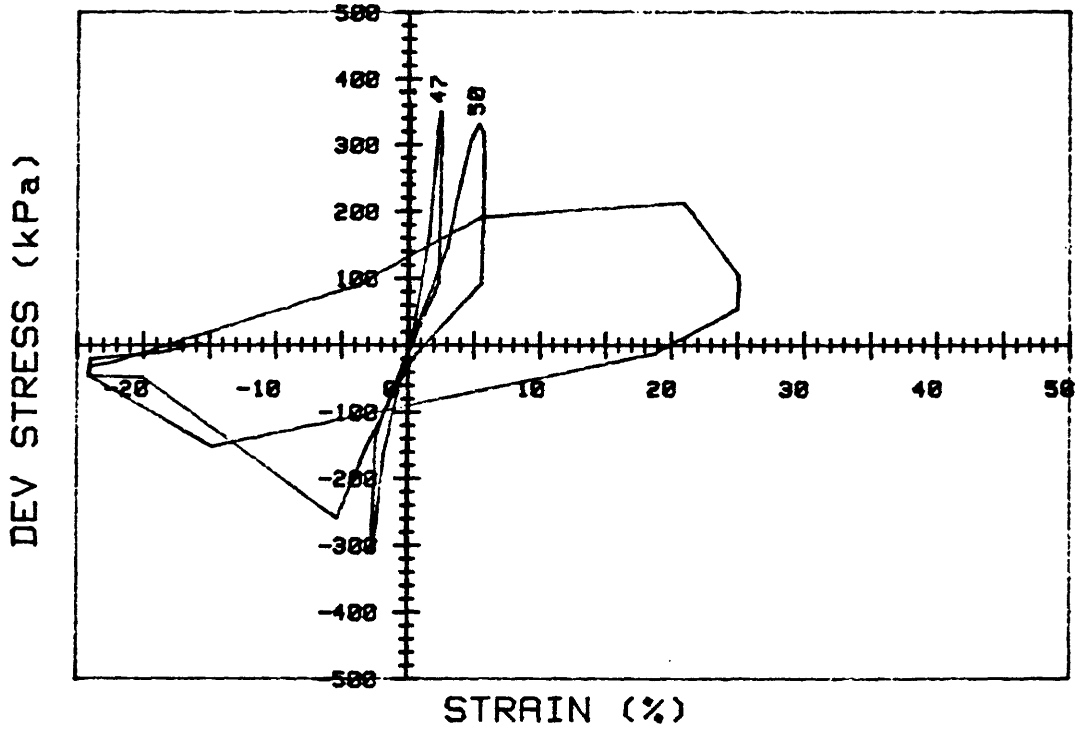

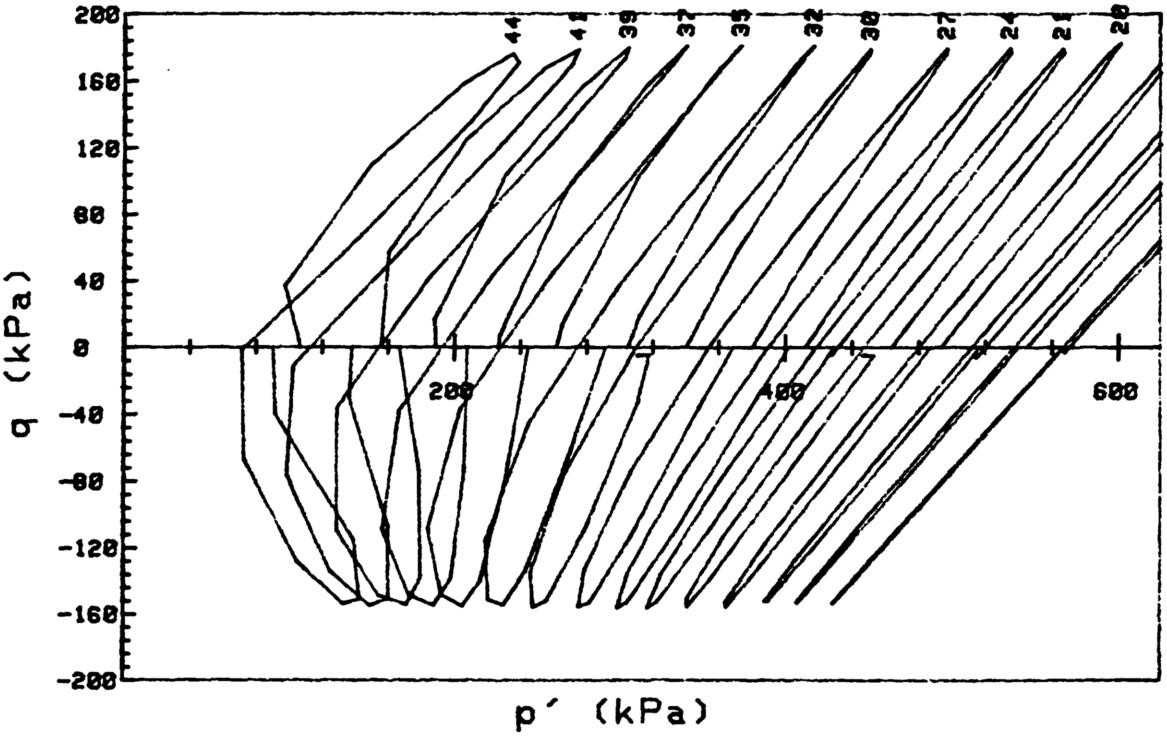

L9-84-CP		INCREMENT (cm)	86-94
CORE NO.	GC8	TEST NO.	D216
SIG1c´(kPa)	570.8	STATIC qf (kPa)	212.0
SIG3c´(kPa)	570.8	AVG MAX q (kPa)	178.6 (84.2%)
INDUCED OCR	1	AVG MIN q (kPa)	-154.5 (72.9%)

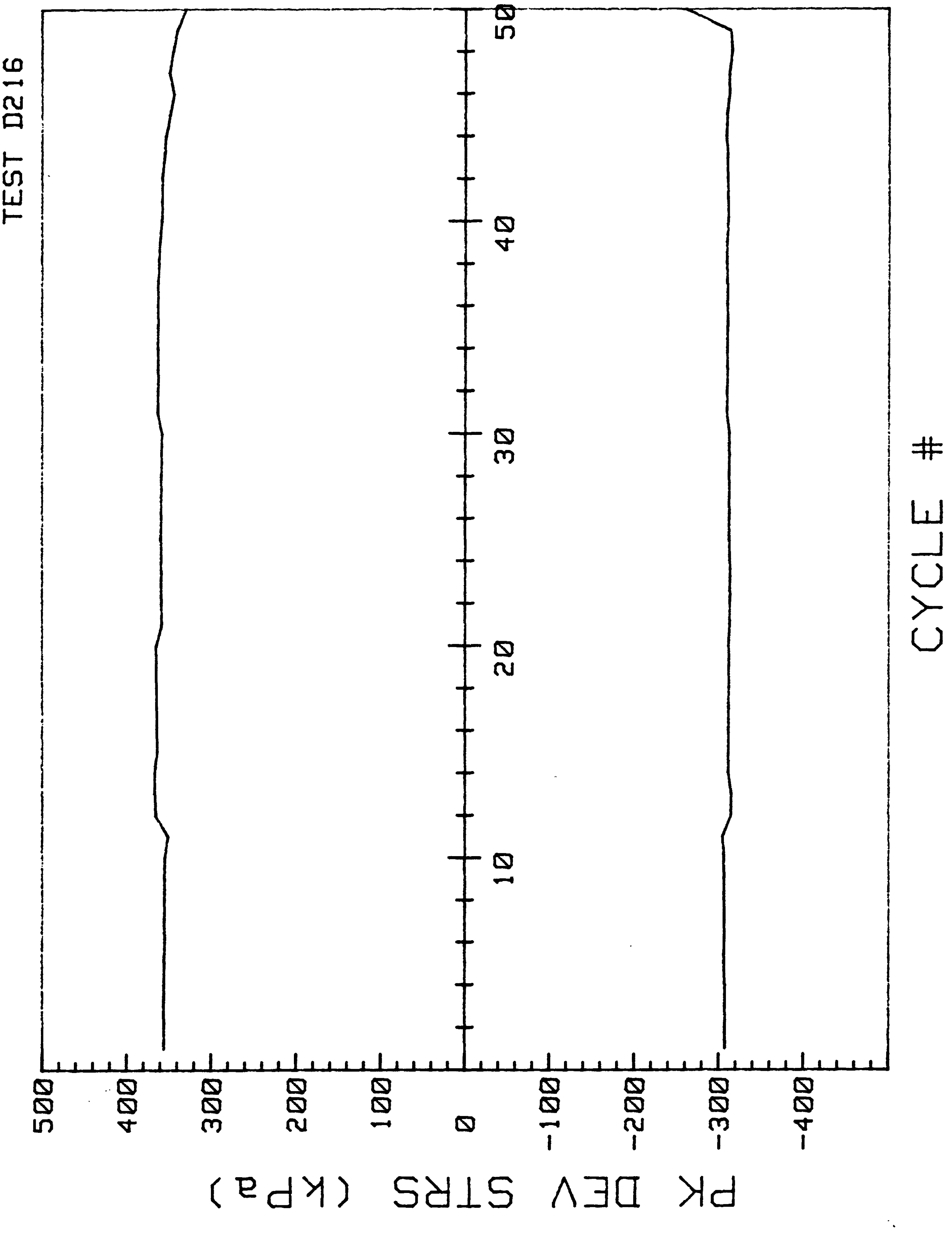
TEST D216
PK DEV STRS (KPa)
500
400
300
200
100
0
-100
-200
-300
-400
CYCLE #
10
20
30
40
50

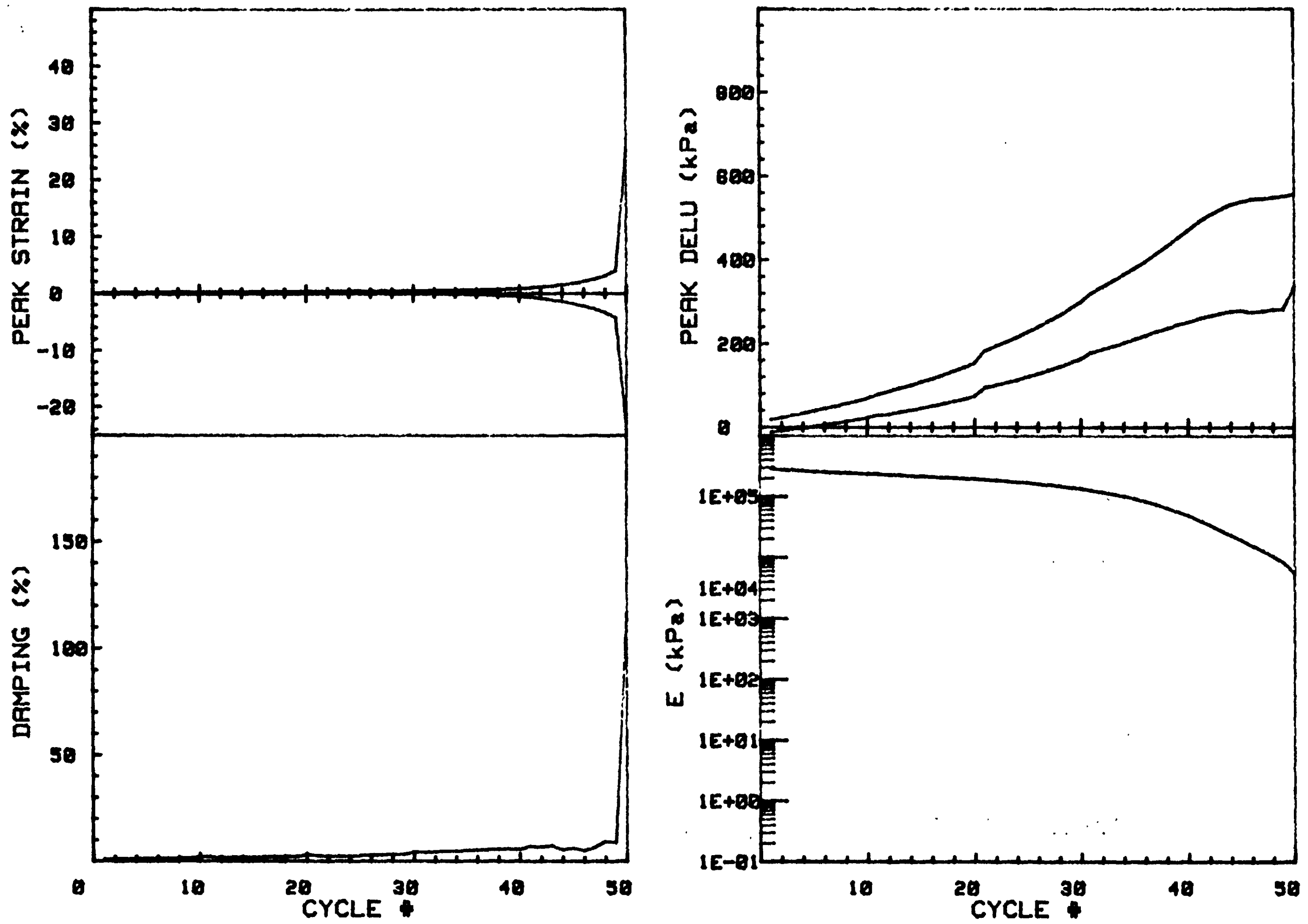

L9-84-CP		INCREMENT (cm)	86-94
CORE NO.	GC8	TEST NO.	D216
SIG1c'(kPa)	570.8	STATIC qf (kPa)	212.0
SIG3c'(kPa)	570.8	AVG MAX q (kPa)	178.6 (84.2%)
INDUCED OCR	1	AVG MIN q (kPa)	-154.5 (72.9%)

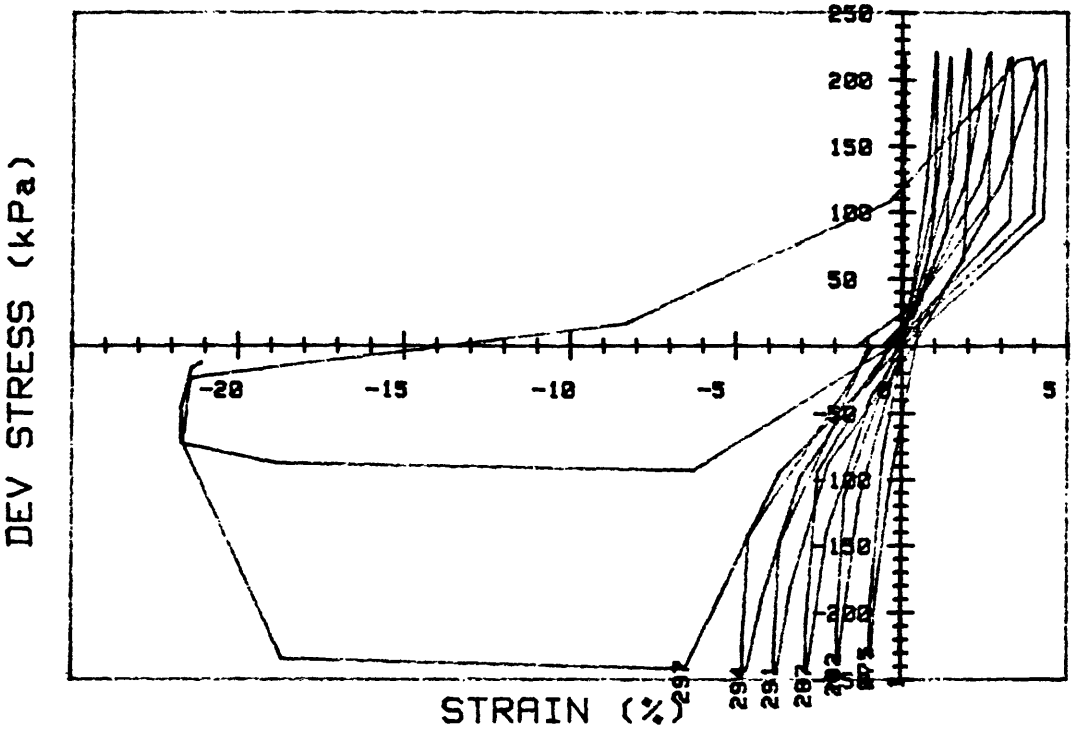

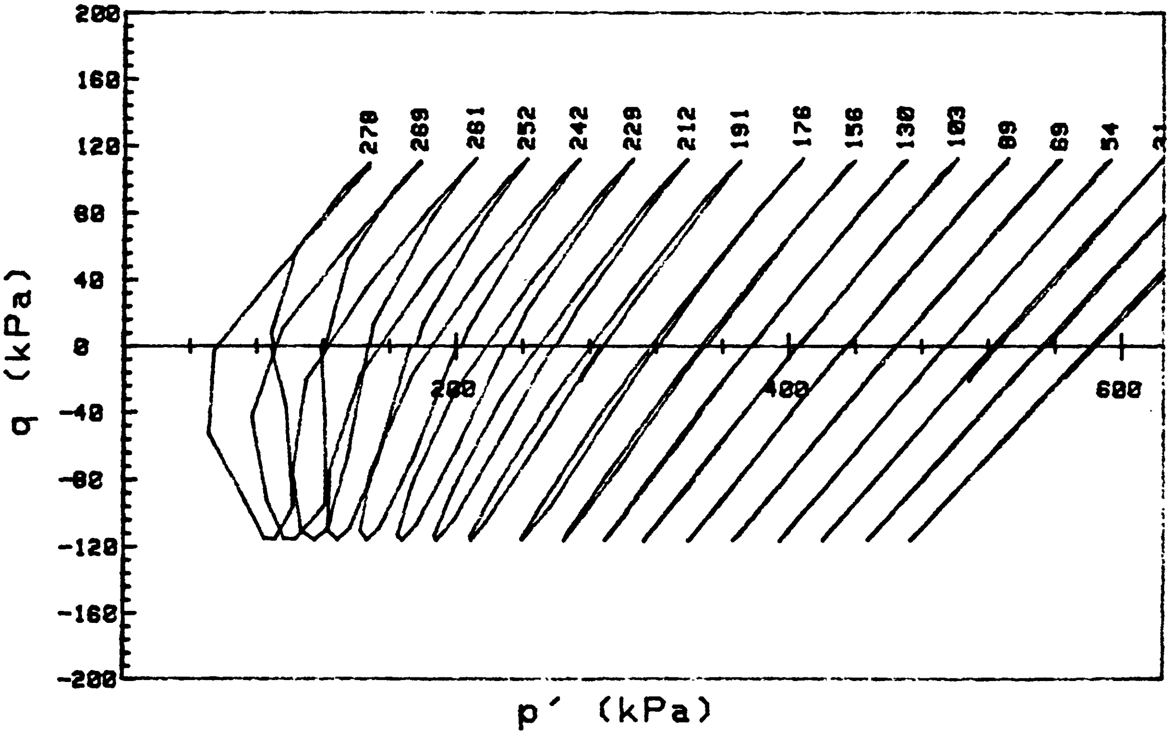

L9-84-CP		INCREMENT (cm)	129-136
CORE NO.	GC8	TEST NO.	D217
SIG1c′(kPa)	585.0	STATIC qf (kPa)	212.0
SIG3c′(kPa)	585.0	AVG MAX q (kPa)	112.1 (52.9%)
INDUCED OCR	1.0	AVG MIN q (kPa)	-116.6 (55.0%)

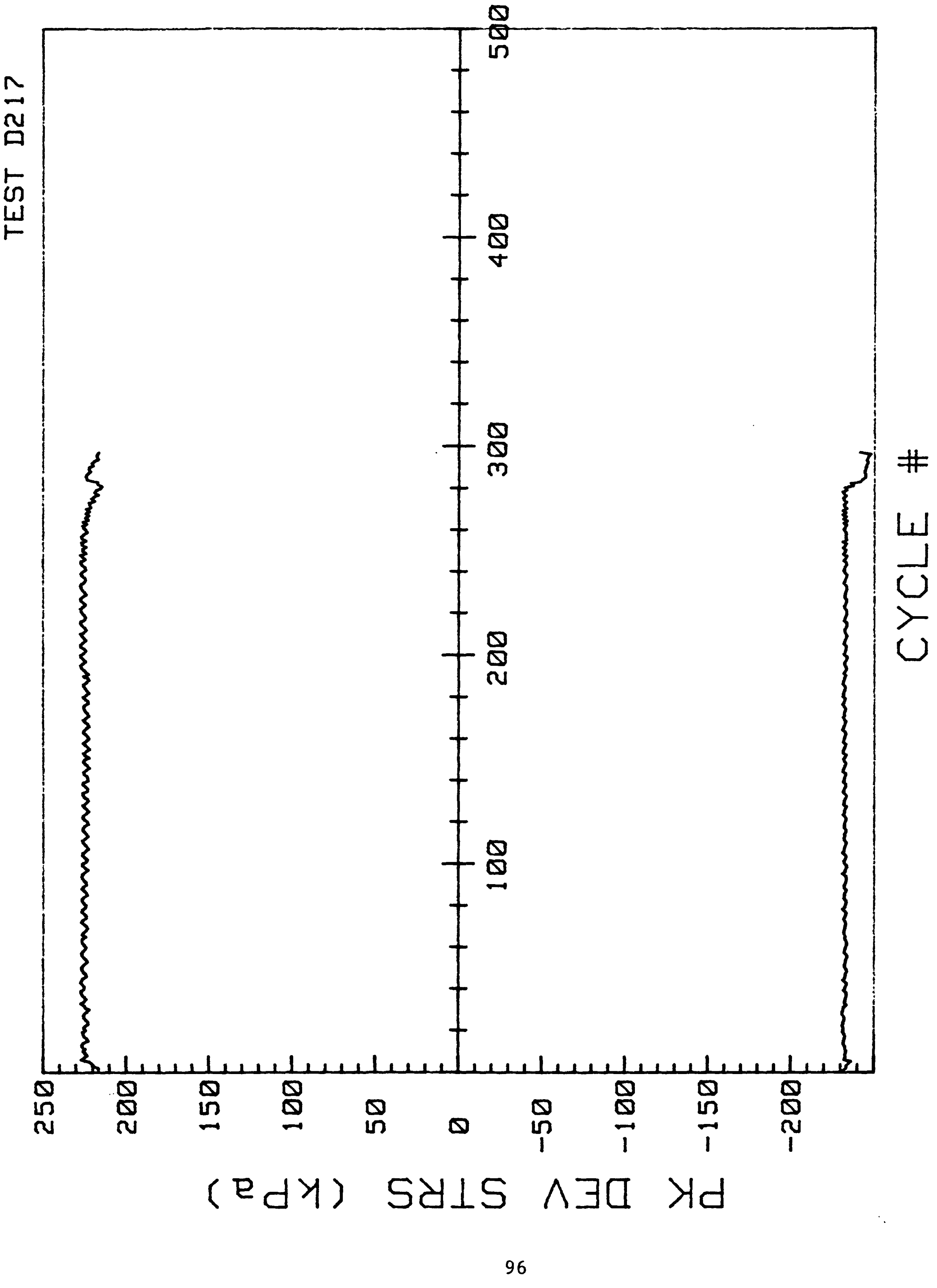
TEST D217
PK DEV STRS (kPa)
250
200
150
100
50
0
-50
-100
-150
-200
CYCLE #
100
200
300
400
500

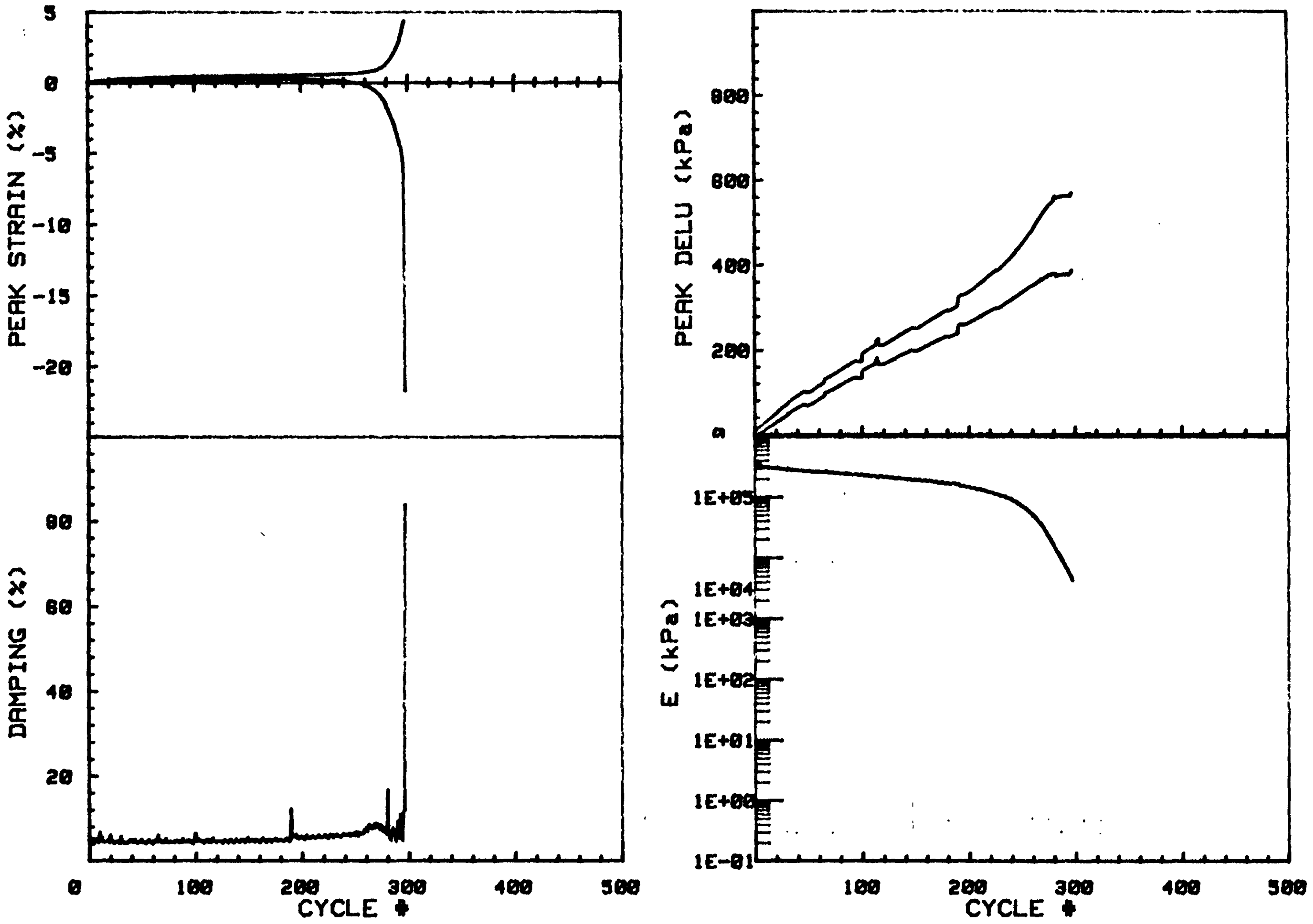

L9-84-CP		INCREMENT (cm)	129-136
CORE NO.	GC8	TEST NO.	D217
SIG1c'(kPa)	585.0	STATIC qf (kPa)	212.0
SIG3c'(kPa)	585.0	AVG MAX q (kPa)	112.1 (52.9%)
INDUCED OCR	1.0	AVG MIN q (kPa)	-116.6 (55.0%)

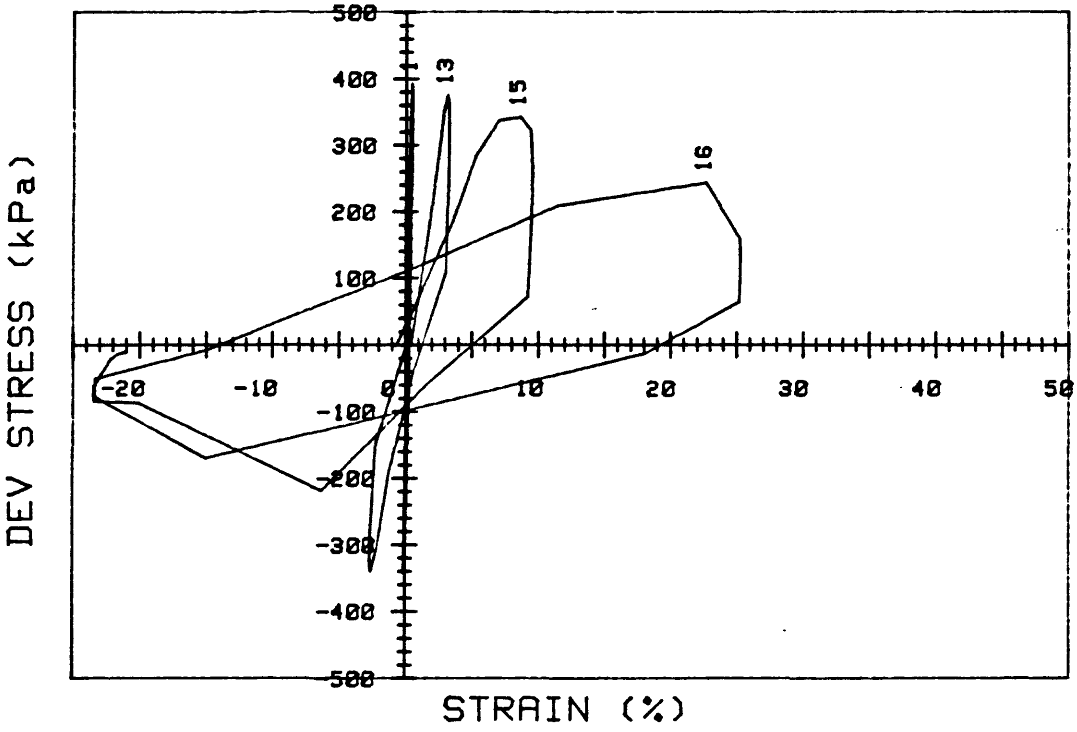

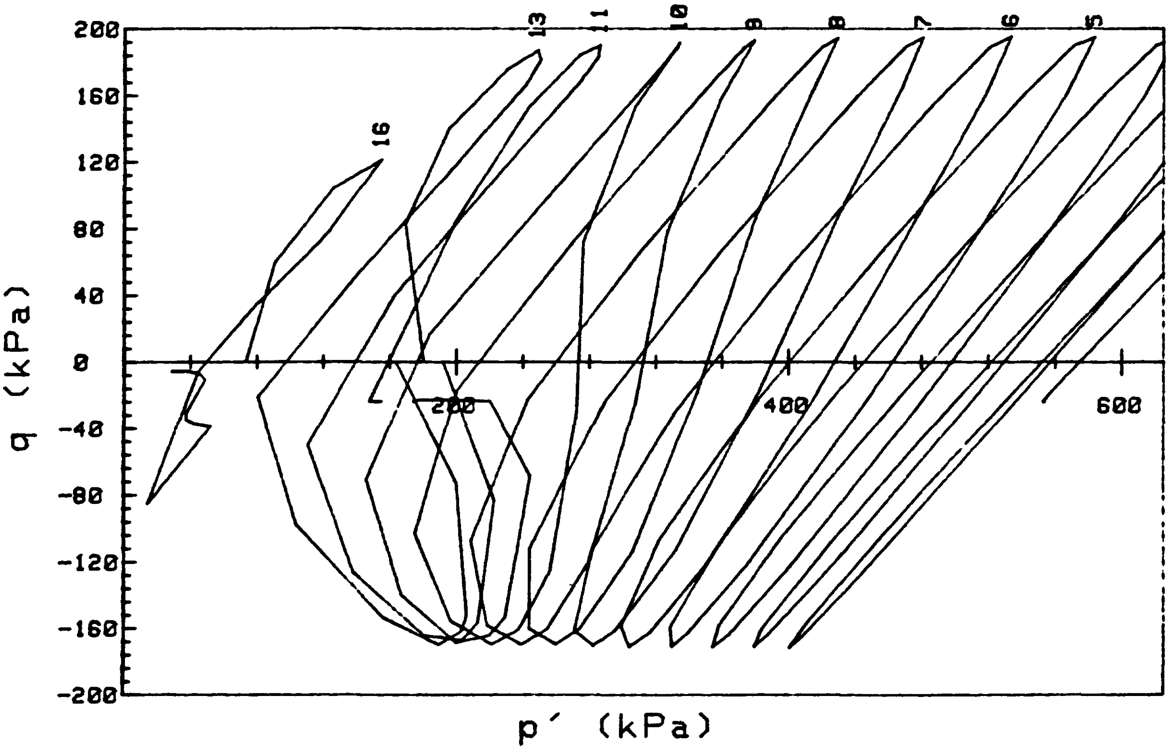

L9-84-CP		INCREMENT (cm)	76-84
CORE NO.	GC8	TEST NO.	D220
SIG1c´(kPa)	577.3	STATIC qf (kPa)	212.0
SIG3c´(kPa)	577.3	AVG MAX q (kPa)	186.6 (88.0%)
INDUCED OCR	1.0	AVG MIN q (kPa)	-161.0 (75.9%)

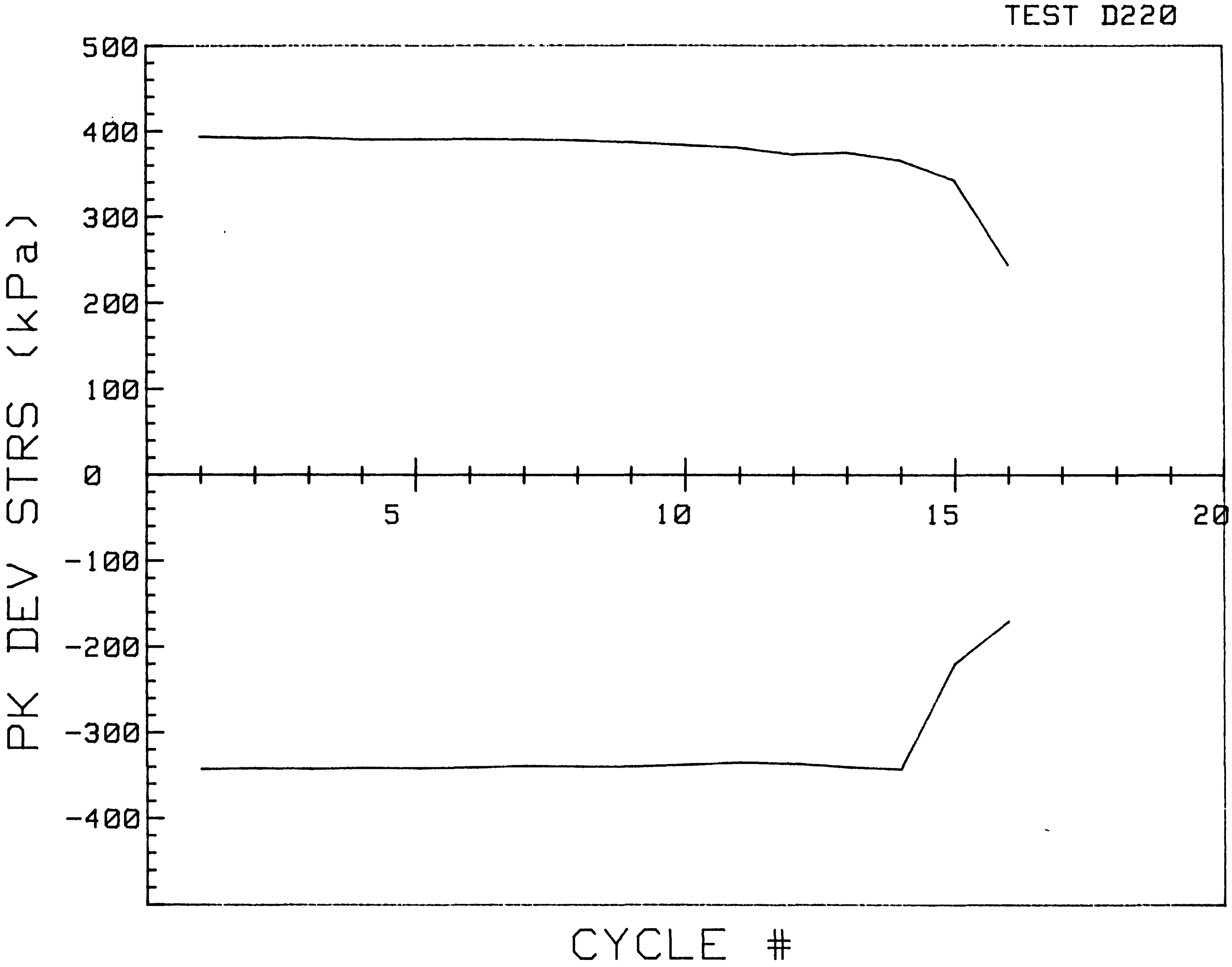
TEST D220
PK DEV STRS (kPa)
500
400
300
200
100
0
-100
-200
-300
-400
5
10
15
20
CYCLE #

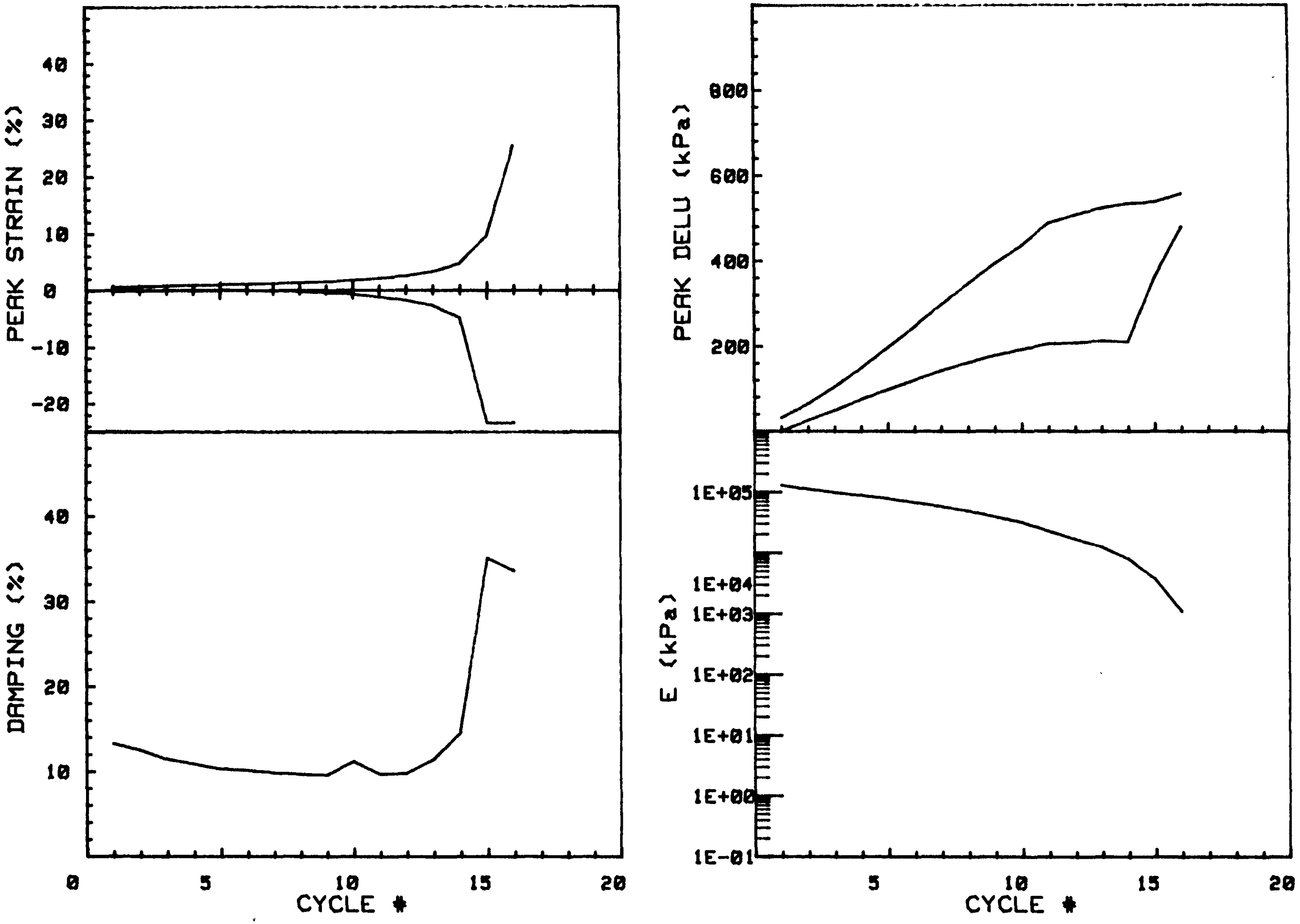

L9-84-CP		INCREMENT (cm)	76-84
CORE NO.	GC8	TEST NO.	D220
SIG1c'(kPa)	577.3	STATIC qf (kPa)	212.0
SIG3c'(kPa)	577.3	AVG MAX q (kPa)	186.6 (88.0%)
INDUCED OCR	1.0	AVG MIN q (kPa)	-161.0 (75.9%)

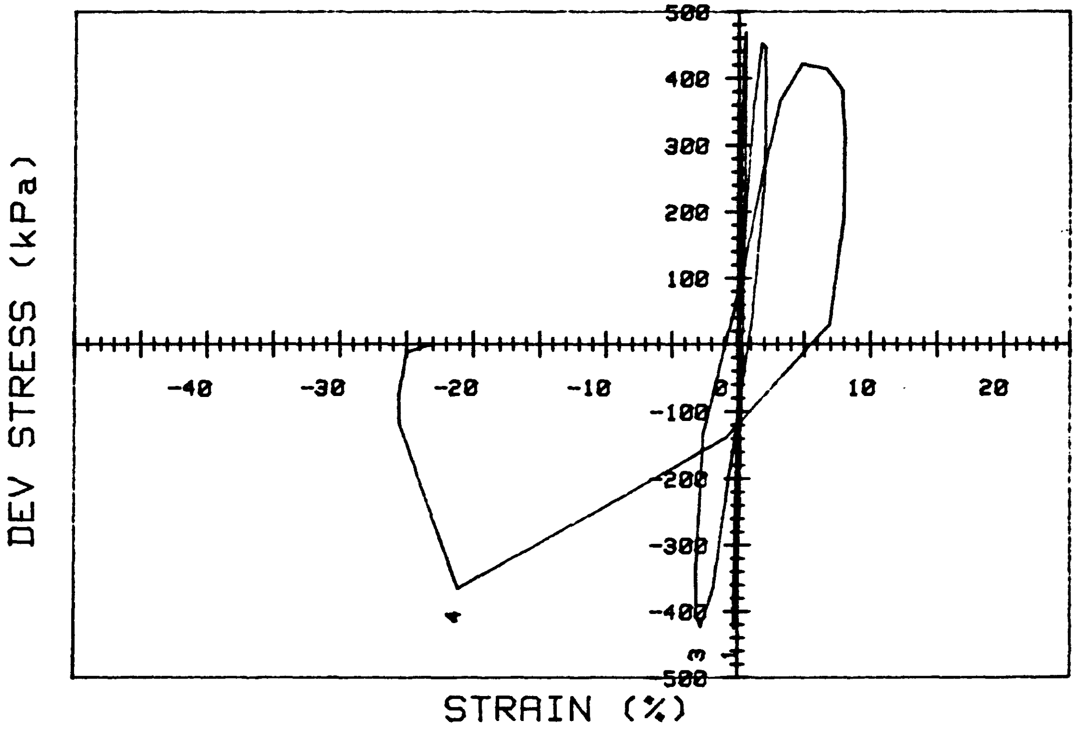

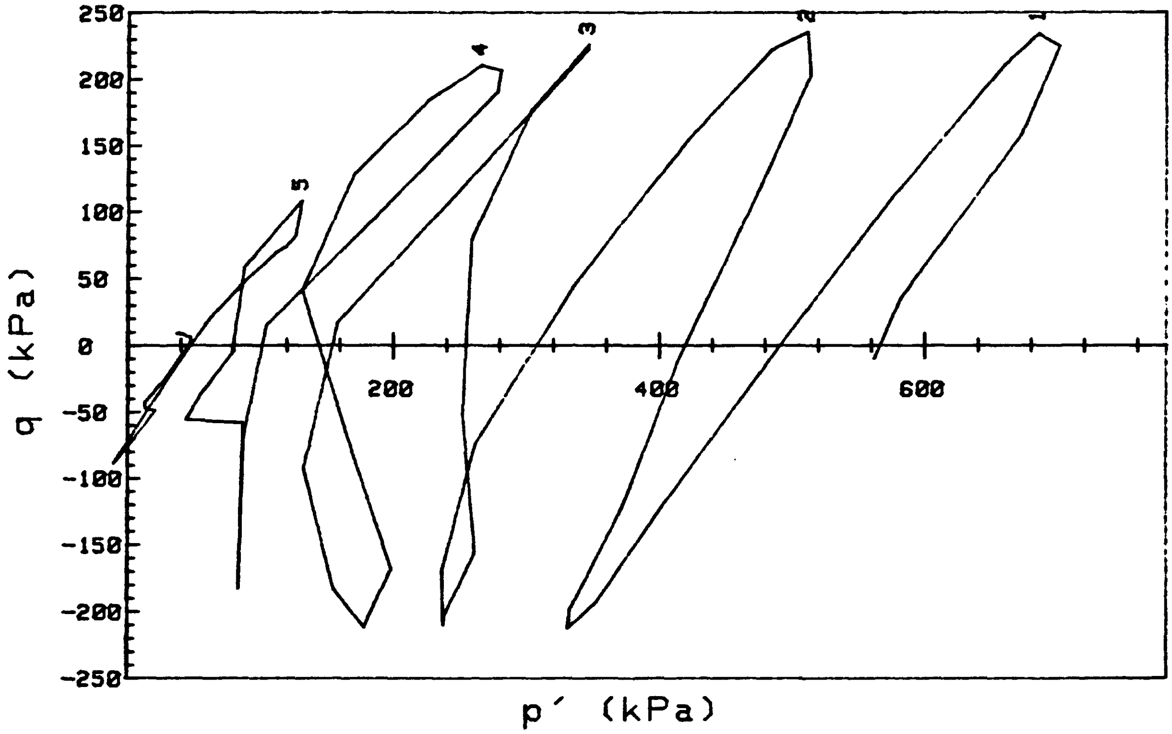

L9-84-CP		INCREMENT (cm)	66-74
CORE NO.	GC8	TEST NO.	D221
SIG1c´(kPa)	572.1	STATIC qf (kPa)	212.0
SIG3c´(kPa)	572.1	AVG MAX q (kPa)	202.9 (95.7%)
INDUCED OCR	1.0	AVG MIN q (kPa)	-181.3 (85.5%)

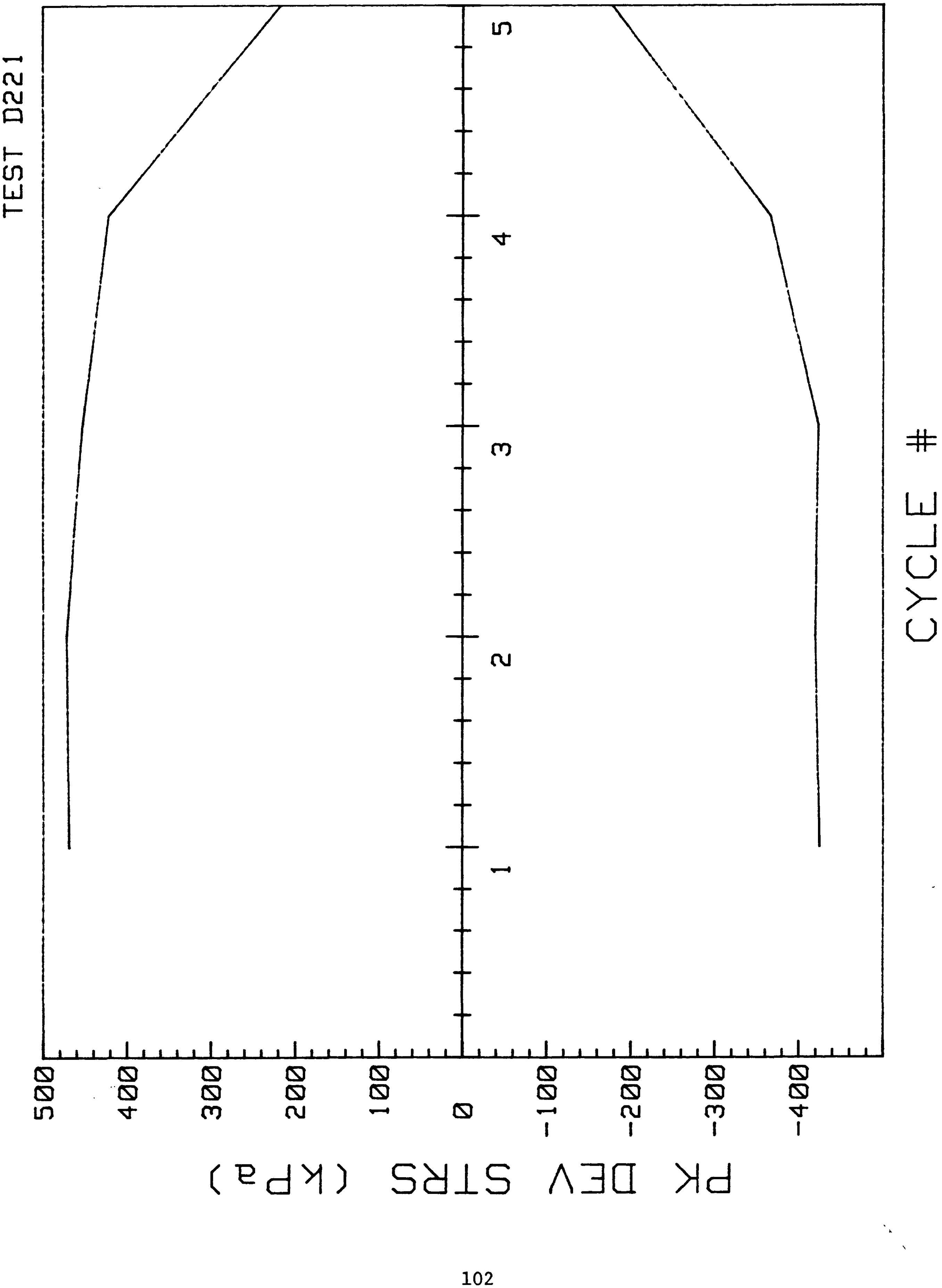
TEST D221
PK DEV STRS (kPa)
500
400
300
200
100
0
-100
-200
-300
-400
CYCLE #
1
2
3
4
5

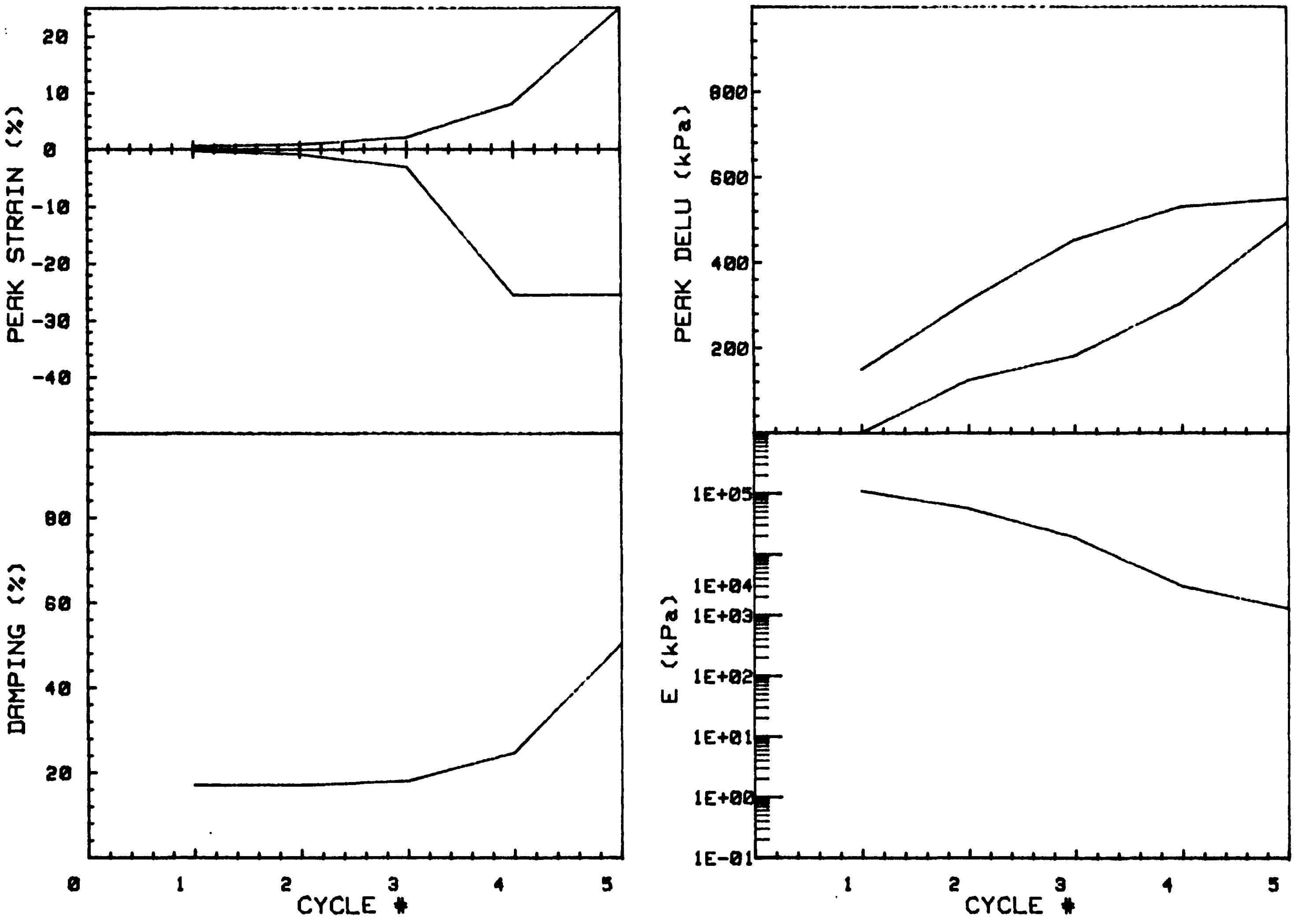

L9-84-CP		INCREMENT (cm)	66-74
CORE NO.	GC8	TEST NO.	D221
SIG1c′(kPa)	572.1	STATIC qf (kPa)	212.0
SIG3c′(kPa)	572.1	AVG MAX q (kPa)	202.9 (95.7%)
INDUCED OCR	1.0	AVG MIN q (kPa)	-181.3 (85.5%)

III. CURRENT METER AND TEMPERATURE MEASUREMENTS ON HORIZON GUYOT AND IMPLICATIONS FOR SEDIMENT TRANSPORT

by

David A. Cacchione, William C. Schwab, George Tate, and Marlene Noble

Introduction

This investigation of near-bottom currents over Horizon Guyot was largely motivated by earlier results reported by Lonsdale and others (1972). Based on speed data from Savonius rotor-type current meters moored at 3 sites within 12 meters of the bottom in about 1675 meters water depth, Lonsdale and others (1972) reported high tidal-current speeds of up to 17 cm/s atop the guyot where sand waves and sand ripples were observed in sidescan-sonar records and bottom photographs. Unfortunately, all of the current meter records were of short duration (less than 5 days each), limiting the analysis of the tidal and lower frequency motions. Other geological evidence of current-induced erosion reported by Lonsdale and others (1972), such as truncated sedimentary units and scour along the guyot's rim, suggested that the mechanism(s) responsible for these features might still be active.

Lonsdale and others (1972) argued that the bedforms and the erosional features were probably caused by internal tidal currents that were intensified along the guyot's surface. Intensification of internal waves above a sloping sea floor were first described theoretically by Wunsch (1969) and Keller and Mow (1969), and later investigated in the laboratory by Cacchione and Wunsch (1974). Based on the results of a combined laboratory and theoretical study of internal waves over sediment-covered slopes, Cacchione (1970) proposed that shoaling internal waves could resuspend and transport sediment in oceanic settings.

Other direct measurements of internal tidal currents and lower frequency motions at mid-Pacific ocean water depths in the vicinity of Horizon Guyot are unavailable. In fact, very few measurements of currents in the mid-water of the deep north Pacific have been reported. Most data taken recently has been obtained in the upper 1000 meters in the low latitudes of the northern Pacific Ocean, in large part a consequence of the general interest in El Nino and deep-ocean mining (Halpern, 1979).

Experiment

A single current meter mooring was deployed during cruise L5-83-HW (Hein and others, 1985a) atop Horizon Guyot in about 1640 m water depth on 10 November 1984. The location (Figure 1-4) was about 3 km to the southeast of mooring site 3 used by Lonsdale and others (1972) on the northeastern sector the guyot cap. Gravity cores, bottom photographs and Conductivity-Temperature-Depth (C-T-D) profiles were also obtained in close proximity to the mooring location (Figs. 1-2, 1-4, and 3-1). The current meter mooring consisted of two vector-averaging current meters (VACM's) at 15 m and 213 m above the guyot summit. A light-emitting diode (LED) deep-sea transmissometer was attached to the lower VACM, and two sediment traps were installed in the mooring at 20 m and 220 m above the bottom. Two ranging acoustic releases were used in parallel arrangement above a 1600 lb. anchor (dual railroad

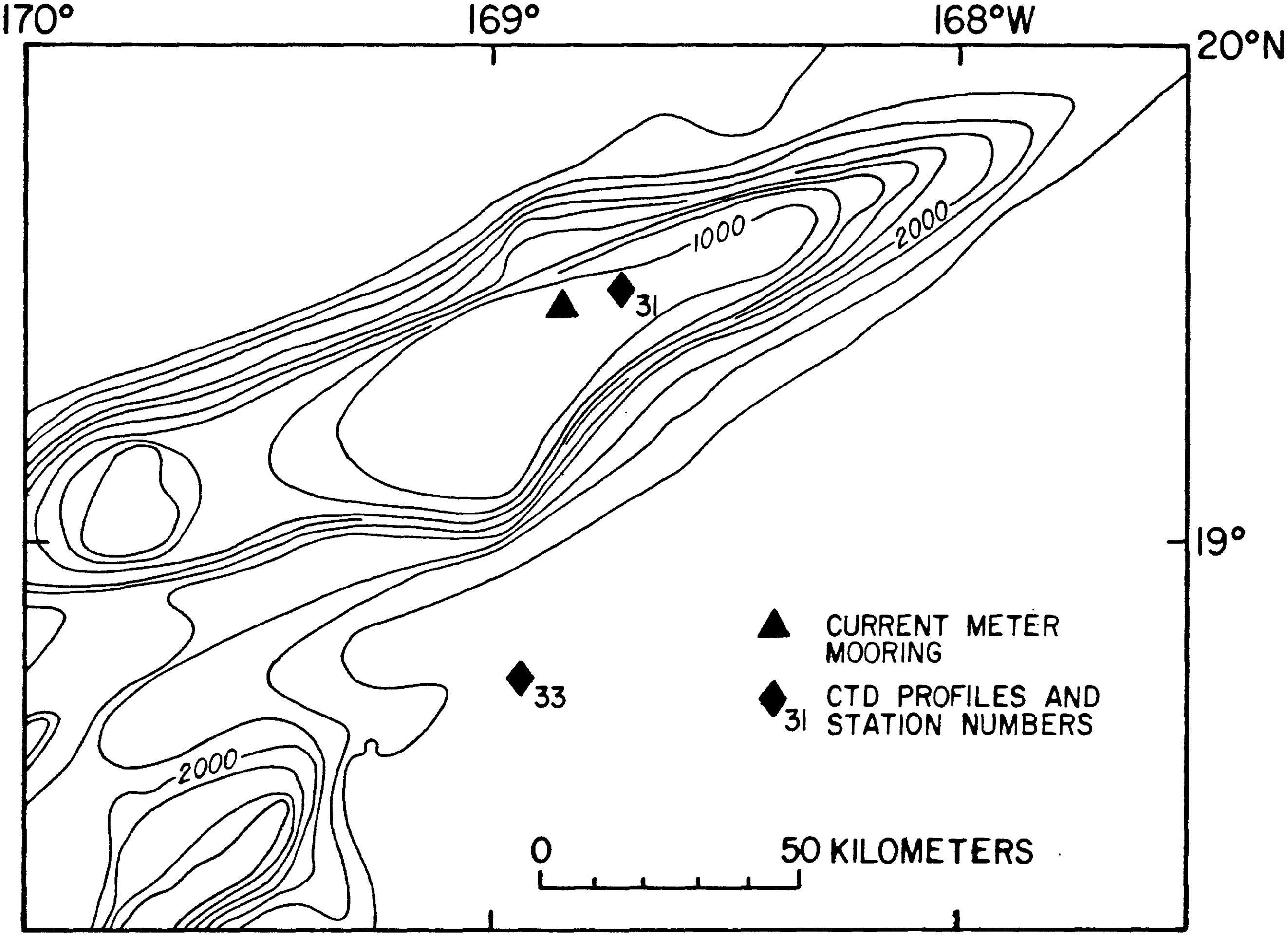

Figure 3-1. Location of C-T-D profiles above Horizon Guyot.

wheels) to recover the mooring. Nineteen buoyant glass floats with plastic covers were distributed along the mooring line above the uppermost sediment trap to provide about 1000 lbs. positive buoyancy. A large recovery float package with submersible flasher and radio transmitter was attached to the top of the mooring. The total mooring length was about 400 meters.

The mooring was recovered successfully during cruise L9-84-CP (Schwab and Bailey, 1985) on 11 August 1984. Initial inspection showed that both sediment traps were intact, with about 1 cm of sediment collected in the upper trap. The current meters and LED transmissometer appeared normal and were not fouled. Unfortunately, later inspection of the sensors showed that the lower VACM had leaked, apparently caused by a failure in the bottom electrical connector to the LED transmissometer. The transmissometer also had flooded because of deformation to its pressure housing. Both instruments were a total loss.

The upper VACM operated successfully for the entire deployment. Vector-averaged currents (N-S and E-W components) and temperature at 213 m above the guyot were obtained every 15 minutes from 14 November 1983 through 10 August 1984. Hourly averages of the current components and temperature were computed, and the hourly values were low-pass filtered using a half-power cut-off of 30 hours. Statistical and spectral analyses were performed for each of the three types of data sets (raw 15 min. values, hourly averages and low-pass filtered hourly values).

Results

The time-series plots of hourly values of temperature, current-components and low-pass filtered current clearly indicate the dominance of the tidal motion above the guyot (Fig. 3-2). Strongest tidal currents occur during the spring months (March-May), with peak speeds of about 30 cm/s. Lonsdale and others (1972) measured maximum tidal current speeds of 17 cm/s within 12 m of the bottom over a 5 day recording duration during March, 1970. The period of most energetic tidal currents in the present experiment is apparently correlated with a gradual warming event in which mean temperatures rose from about 2.8°C in early February to a maximum of nearly 3.1°C in March, and then cooled to about 2.9°C in May. There is also a clear indication in Fig. 3-2 that the energetic tidal currents in March and again in May are correlated with the largest, apparently tidally driven fluctuations in temperature.

Results of a statistical analysis of the hourly data of currents and temperature are presented in Table 3-1. Mean current speed is about 1.5 cm/s for the entire 9 month record (1.3 cm/s to the east and 0.86 cm/s to the south); mean temperature was 2.92°C. Although the mean component speeds were low, the variance in the currents was large, not surprising since the dominance of the tidal fluctuations is so apparent in Fig. 3-2. Maximum values of the current components basically represent the peak values of the tidal currents (about 30 cm/s). We computed the current ellipse for the hourly current data using the technique of Noble and others (1986) and found a weak ellipticity index = 0.35, suggesting rotary-like tidal flow, with an ellipse orientation of 151° true. The major and minor axes were 7.9 and 5.2 cm/s, respectively. It is worth noting that the tidal current ellipse is oriented nearly orthogonal to the orientation of the long axis of the guyot (60° True) as seen in Fig. 3-1.

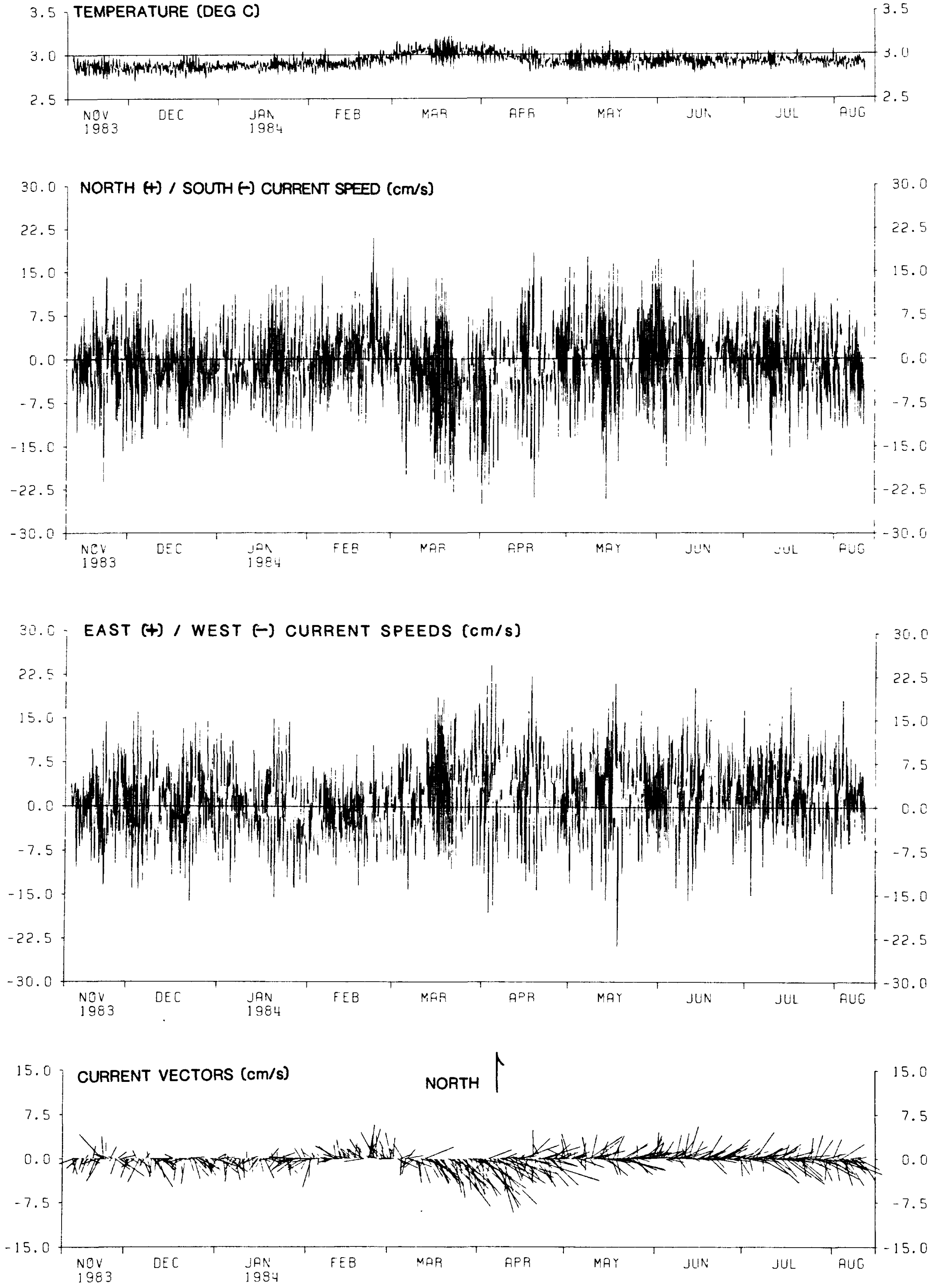

Figure 3-2. Time series of hourly values of temperature, N-S current component, E-W current component and low frequency currents at 213 m above Horizon Guyot. Measurements were obtained with a bottom moored vector-averaging current meter.

Table 3-1. Statistics of hourly current and temperature measurements on Horizon Guyot during 14 Nov 83 - 10 Aug 84. Data points = 6,481 each.

Statistical Parameter	North (+) - South (-) (cm/s)	East (+) - West (-) (cm/s)	Temperature (°C)
mean	-0.59	1.48	2.92
variance	48.74	41.54	0.0061
maximum	20.95	27.46	3.27
minimum	-28.21	-25.12	2.67

Table 3-2. Statistics of low-pass filtered current and temperature measurements on Horizon Guyot during 14 Nov 83 - 10 Aug 84. Data points = 1,081 each.

Statistical Parameter	North (+) - South (-) (cm/s)	East (+) - West (-) (cm/s)	Temperature (°C)
mean	-0.59	1.48	2.92
variance	6.03	6.05	0.0028
maximum	5.83	11.84	3.07
minimum	-9.27	-5.95	2.82

The distinct dominance of the M_2 tidal signal can be clearly seen in the spectra of currents and temperature (Figs. 3-3a to 3-3c). These spectra have been normalized so that the total area under the curve is equal to the variance; therefore, the relative magnitudes of the peaks represent the relative magnitudes of the kinetic energy in that frequency band. The M_2 tidal energy overwhelms the other portions of the spectra for both currents and temperature. A broad near-inertial peak can be found at about 34 hours in current and temperature (inertial period = 37.1 hours), but its amplitude is nearly an order of magnitude less than that of the M_2 tidal current signal. The broadening of the energy band near the inertial signal can be seen in the power spectral plots in Figs. 3-4a to 3-4c. These plots again show the dominance of the M_2 tidal signal (note that the vertical scale is logarithmic), and additionally indicate that a few peaks in the higher frequency motions might be significant at the 95% level of confidence. It appears that some of these higher frequency peaks are probably M_2 tidal harmonics, but further analysis of these are needed to investigate this relationship. The second peak up from the M_2 tidal peak into the higher frequency band is at about 6.2 hours, and most likely is a first harmonic of the tide. The first peak up from the M_2 tide that appears significant at the 95% confidence level is at 9.4 hours, and possibly represents higher frequency internal wave motion.

The low frequency motion above the guyot is represented by the plot of vectors of low-pass filtered hourly currents in Fig. 3-2. Table 3-2 gives the statistics for the low frequency currents. From Table 3-2, we can estimate that the mean speed is only about 1.6 cm/s in a southeasterly direction. The maximum low frequency current speeds are easterly (+11.8 cm/s) and southerly (-9.3 cm/s), which occurs during the period of relatively high current activity during March-April (Fig. 3-2). The low frequency flow shows a dramatic change in character during these two months in contrast to the other periods when the currents are variable and of low magnitude. Starting in early March and persisting through April the low frequency flow is decidedly toward the SE with speeds of up to 15 cm/s. This period of higher speeds toward the SE is coincident with the time of increased tidal current speeds and temperature activity. The current ellipse for the low-pass filtered values for the entire record has an orientation of 135^o true, with major and minor axes of 2.7 and 2.2 cm/s, respectively. The ellipticity index is only 0.17, suggesting (along with the nearly equal values of the major and minor axes) that the low-frequency currents generally do not have a preferred direction. However, during the months of March and April, as has already been discussed, there was a definite preferred SE flow across the strike of the guyot's bathymetric orientation.

C-T-D profiles were taken near the site of the current meter mooring above the guyot cap and over the southern flank (Fig. 3-1). The profiles are shown in Figures 3-5a to 3-5c (guyot top) and Figures 3-6a to 3-6c (guyot flank). There is a strong upper pycnocline from about 80 m to 700 m (Fig. 3-6c) associated with a large temperature gradient (Figs. 3-6a). Below about 700 m the temperature and density gradients are substantially more reduced, and become approximately linear below about 1200 m (Figs. 3-5c and 3-6c). The Brunt-Vaisala frequency, N, can be calculated from the density profile and is approximately given by

$$N = [(g/\rho') (d\rho/db)]^{1/2} \tag{1}$$

Figure 3-3. Spectral plots of (a) north-south currents, (b) east-west currents and (c) temperature. Spectra have been normalized so that total area under each curve is equal to the variance. Data are shown in Figure 3-2.

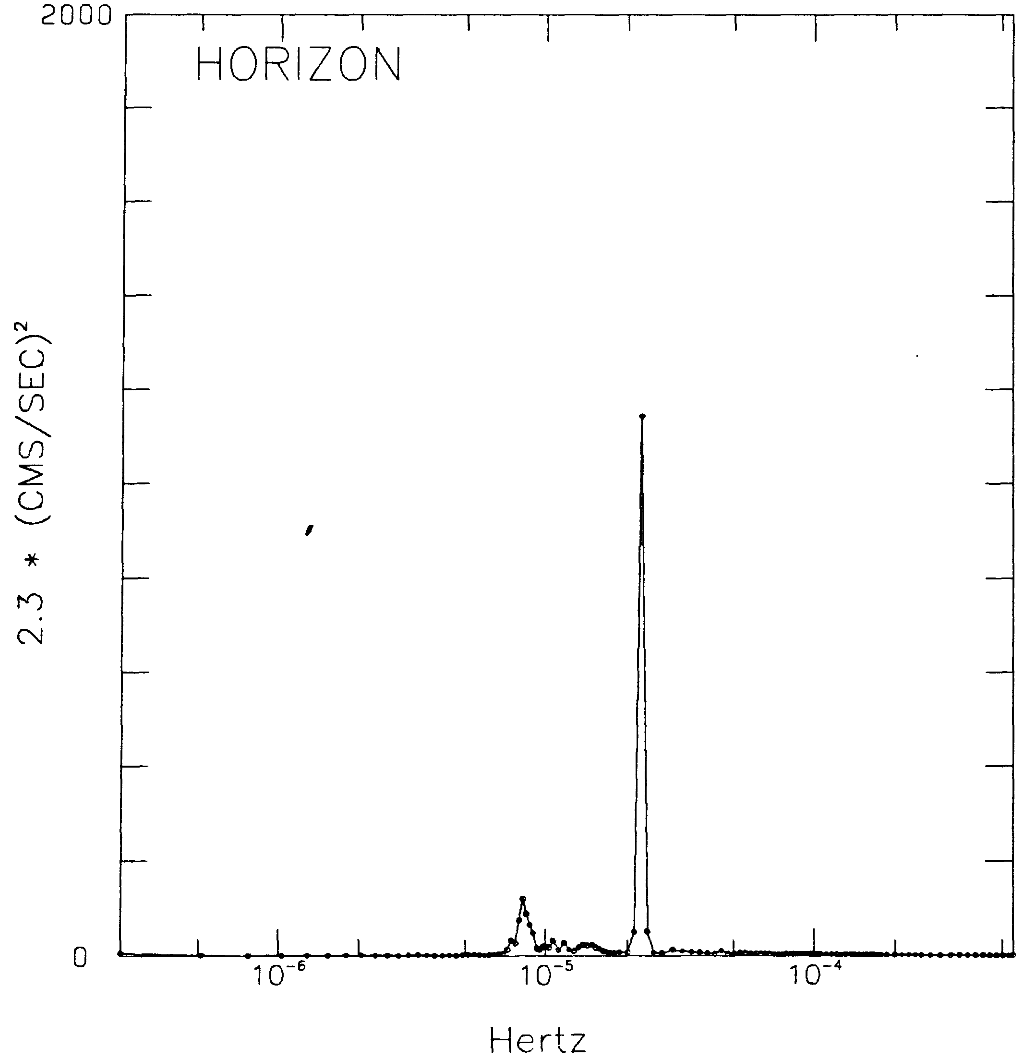

Figure 3-3a.

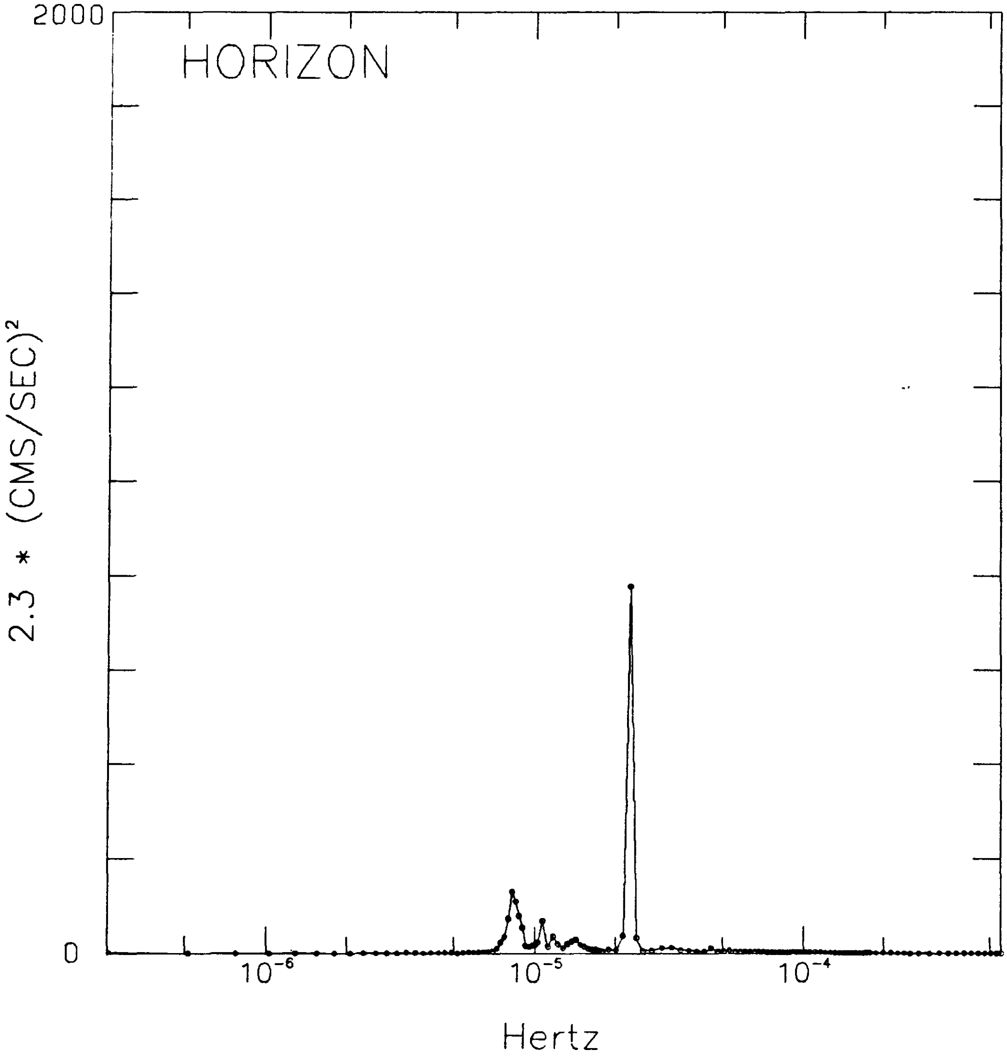

Figure 3-3b.

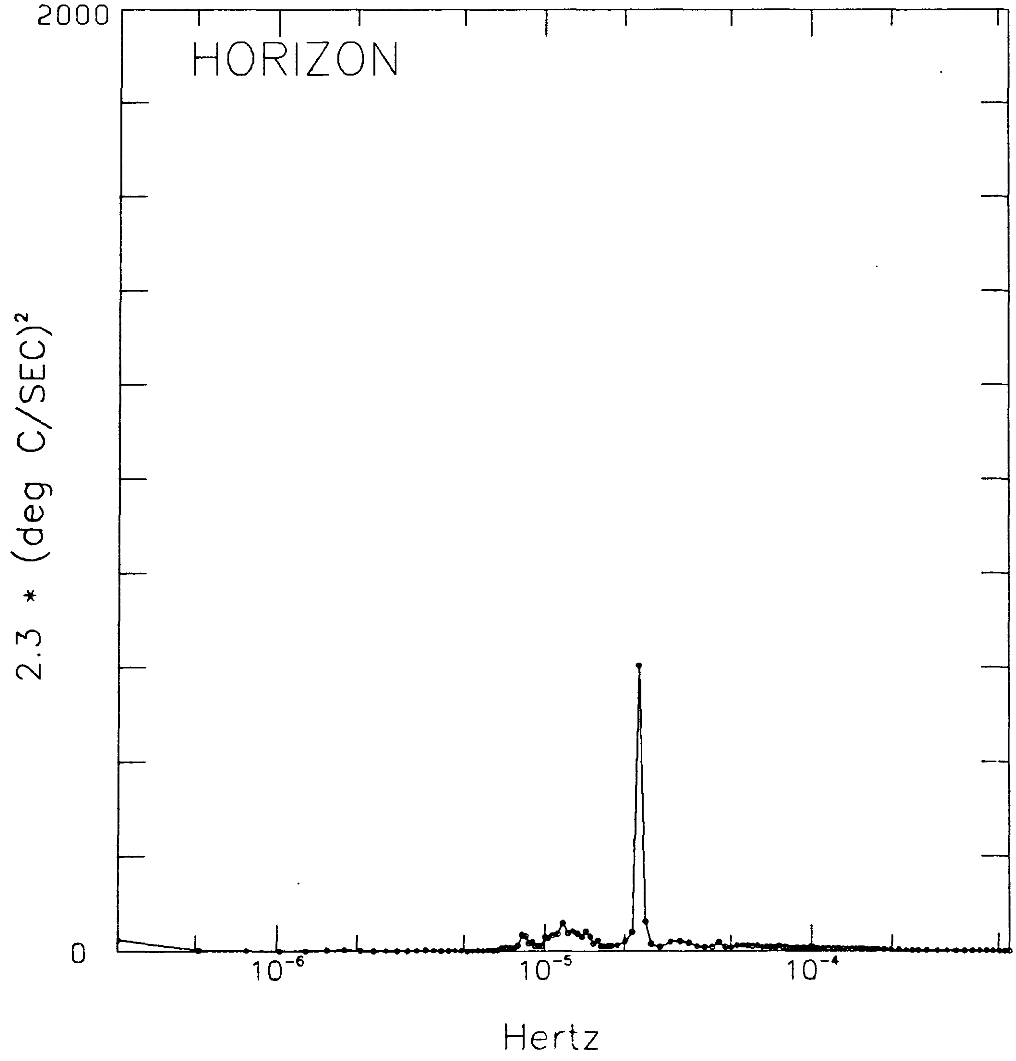

Figure 3-3c.

Figure 3-4. Power spectra plots of (a) north-south currents, (b) east-west currents and (c) temperature. Data are shown in Figure 3-2.

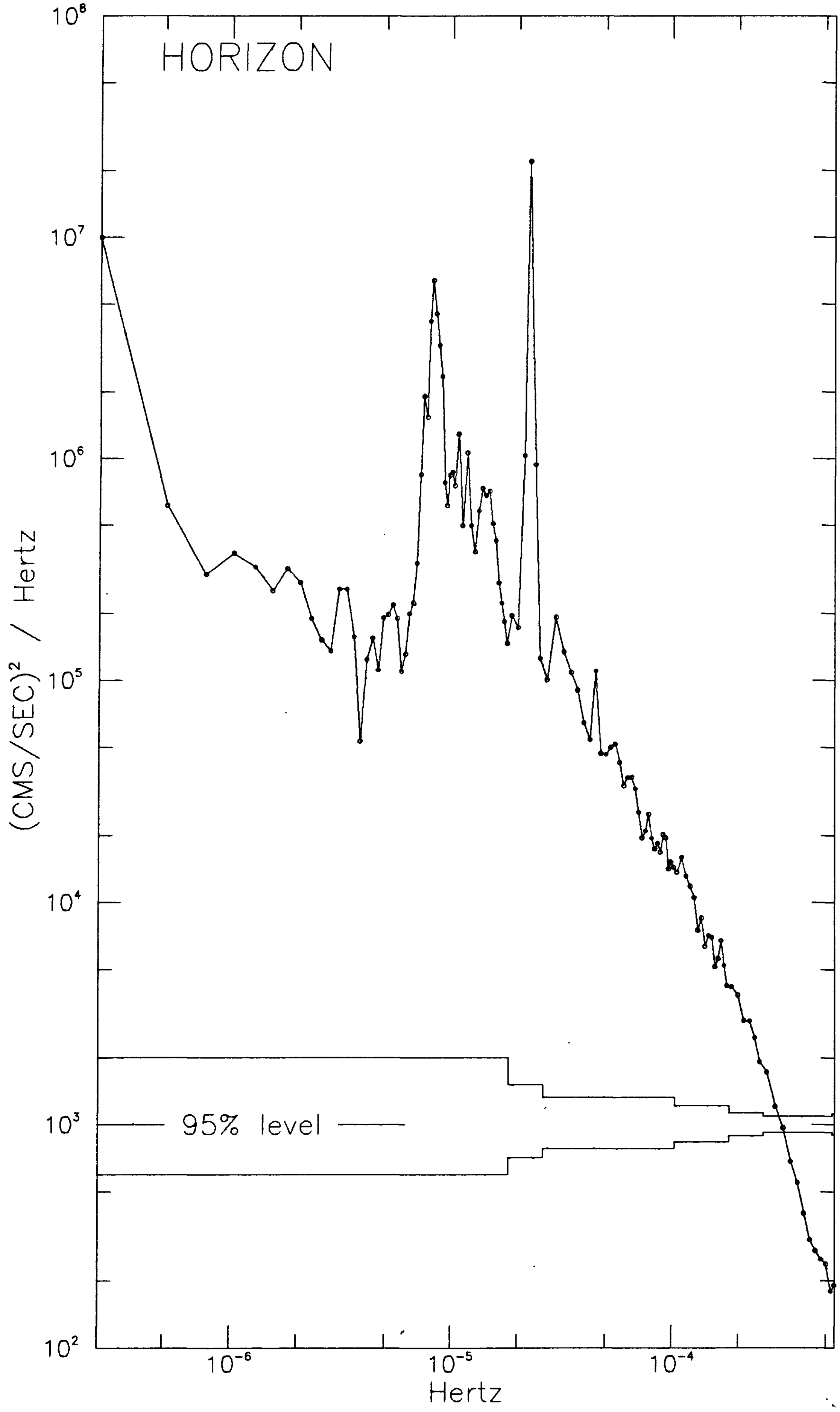
HORIZON
10^8
10^7
10^6
10^5
10^4
10^3
10^2
(CMS/SEC)^2 / Hertz
95% level
10^{-6}
10^{-5}
10^{-4}
Hertz

Figure 3-4a.

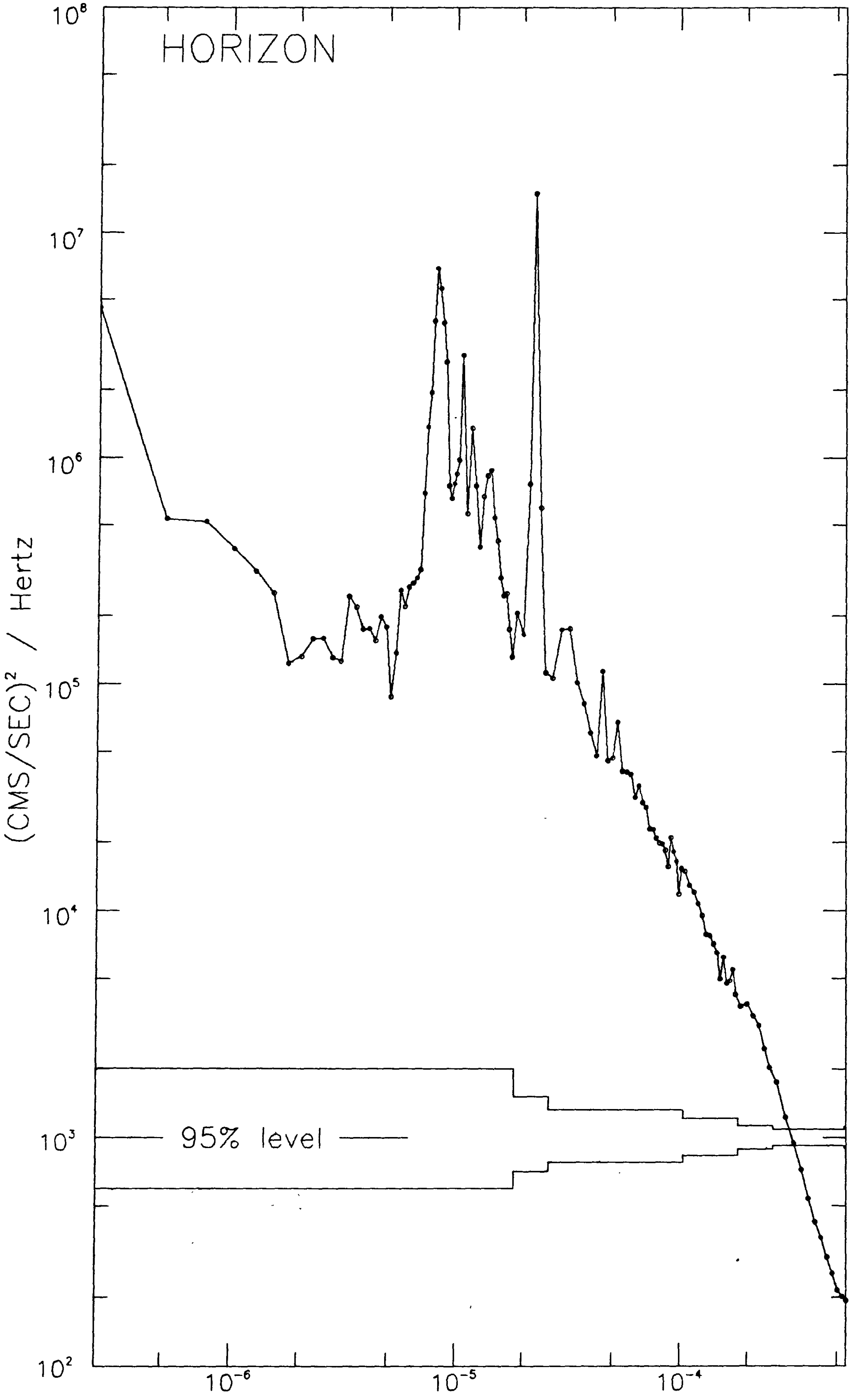
HORIZON
10^8
10^7
10^6
10^5
10^4
10^3
10^2
$(CMS/SEC)^2$ / Hertz
95% level
10^{-6}
10^{-5}
10^{-4}
Hertz

Figure 3-4b.

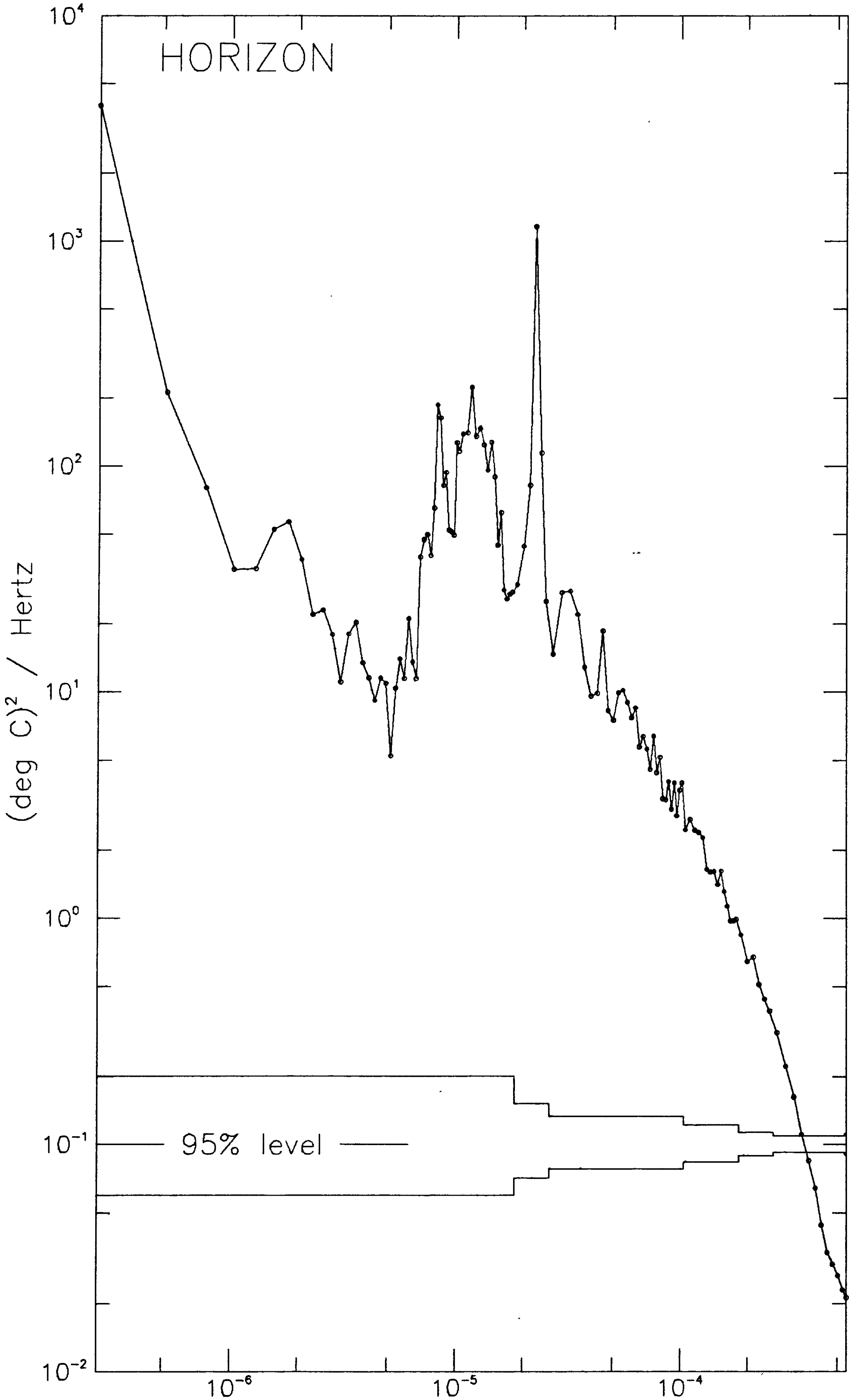
HORIZON
10^4
10^3
10^2
10^1
10^0
10^{-1}
10^{-2}
(deg C)² / Hertz
95% level
10^{-6}
10^{-5}
10^{-4}
Hertz

Figure 3-4c.

Figure 3-5. Conductivity-Temperature-Depth (C-T-D) profiles on top of Horizon Guyot (from Hein and others, 1985a) taken near the site of the current meter mooring shown in Figure 3-1 (Station 31). (a) Temperature, (b) Salinity, and (c) Sigma-t.

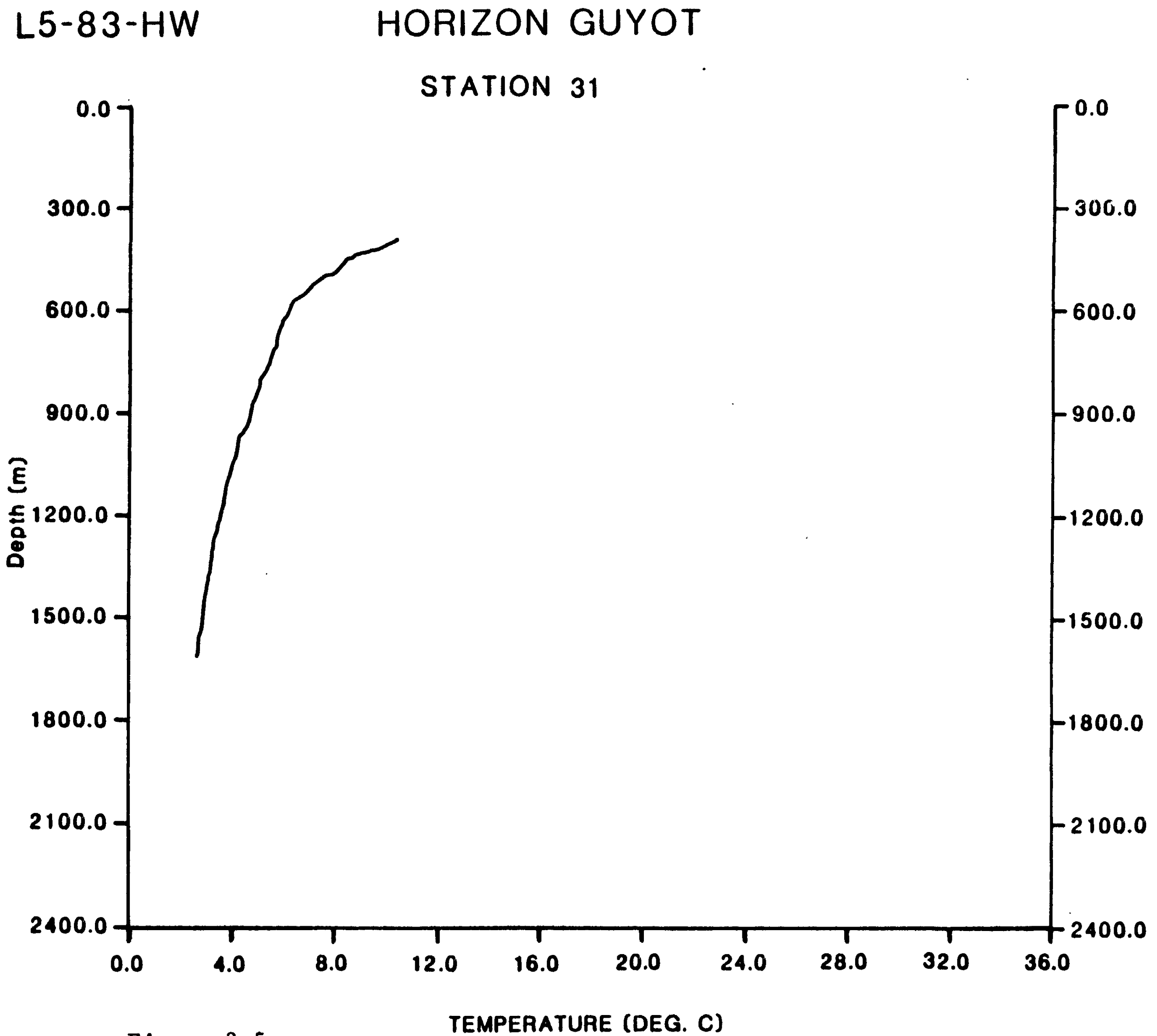
L5-83-HW
HORIZON GUYOT
STATION 31
Depth (m)
0.0
300.0
600.0
900.0
1200.0
1500.0
1800.0
2100.0
2400.0
0.0
4.0
8.0
12.0
16.0
20.0
24.0
28.0
32.0
36.0
TEMPERATURE (DEG. C)

Figure 3-5a.

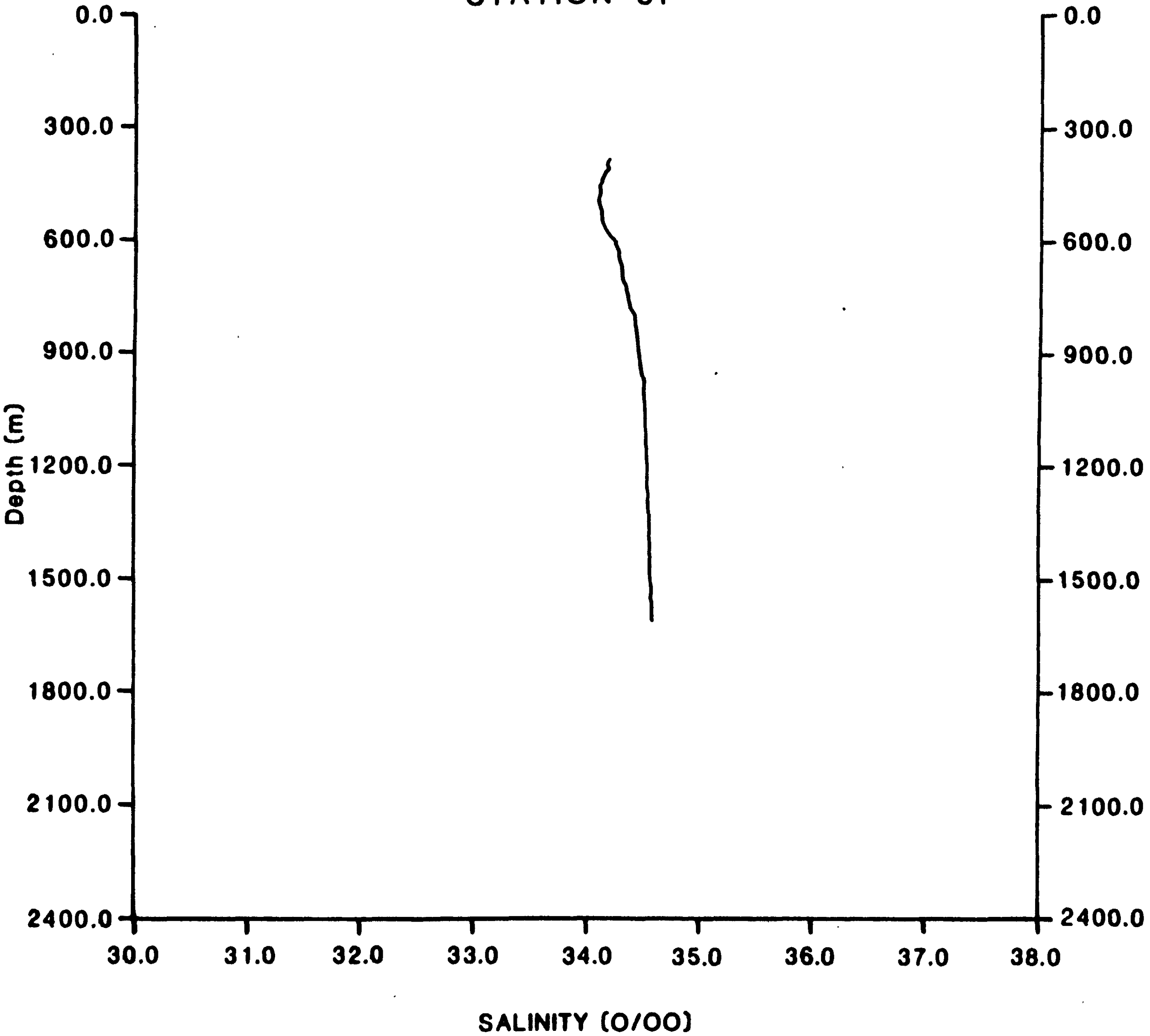
L5-83-HW HORIZON GUYOT

STATION 31

Figure 3-5b.

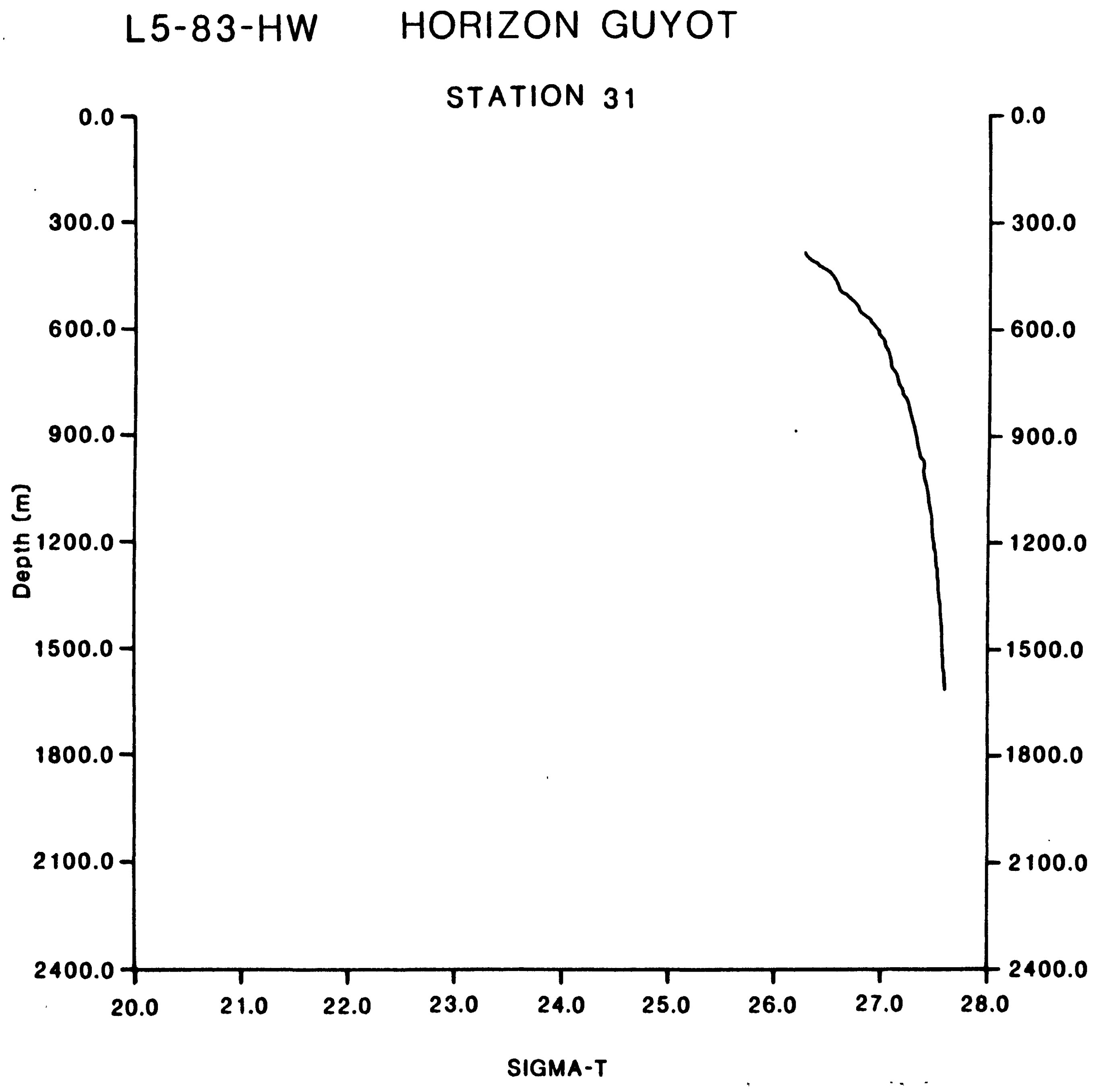
L5-83-HW HORIZON GUYOT
STATION 31
Depth (m)
0.0
300.0
600.0
900.0
1200.0
1500.0
1800.0
2100.0
2400.0
20.0
21.0
22.0
23.0
24.0
25.0
26.0
27.0
28.0
SIGMA-T

Figure 3-5c.

Figure 3-6. C-T-D profiles from the flank of Horizon Guyot (Station 33, Figure 3-1) (from Hein and others, 1985a). (a) Temperature, (b) Salinity, and (c) Sigma-t.

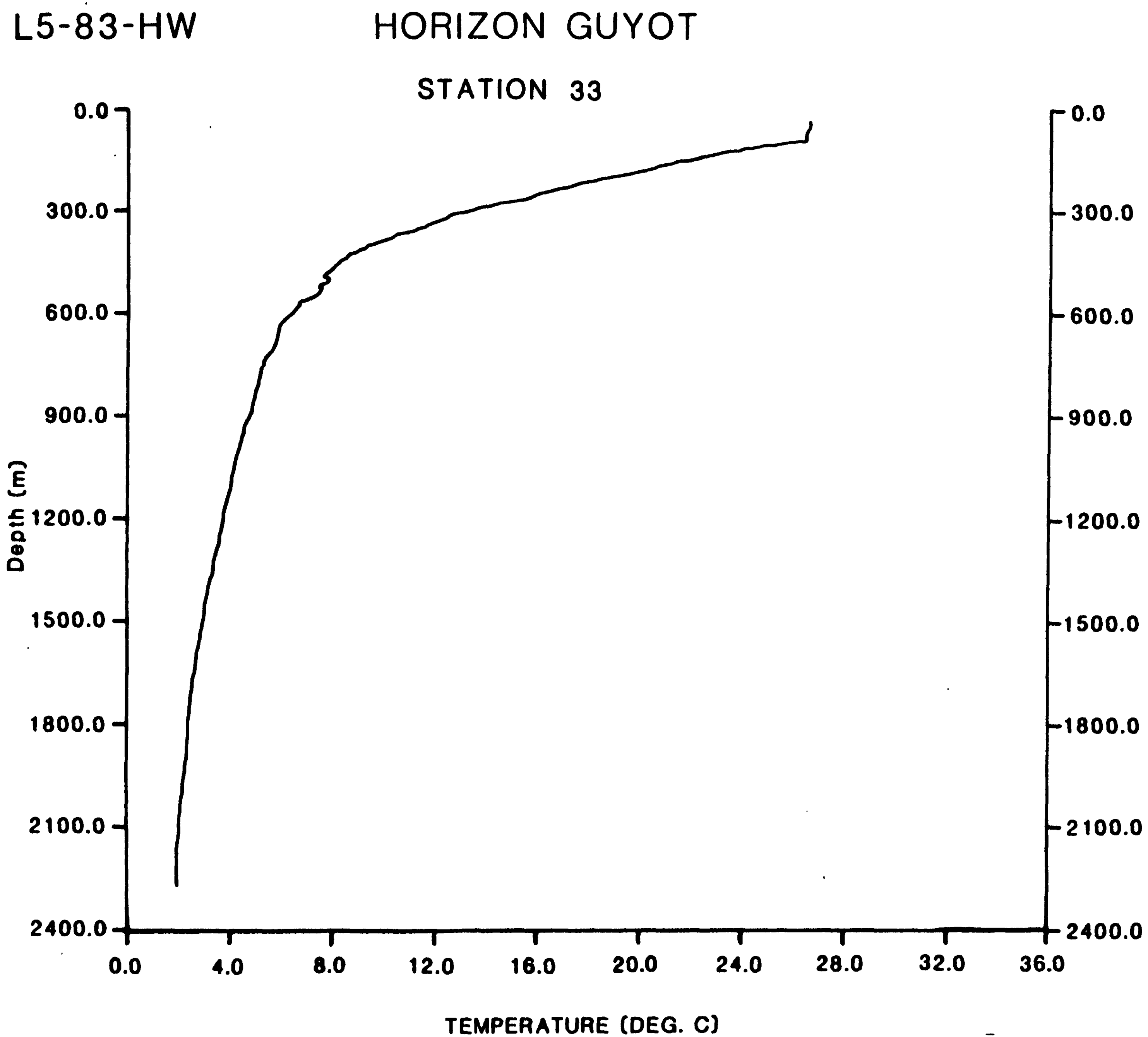
L5-83-HW
HORIZON GUYOT
STATION 33
Depth (m)
0.0
300.0
600.0
900.0
1200.0
1500.0
1800.0
2100.0
2400.0
0.0
4.0
8.0
12.0
16.0
20.0
24.0
28.0
32.0
36.0
TEMPERATURE (DEG. C)

Figure 3-6a.

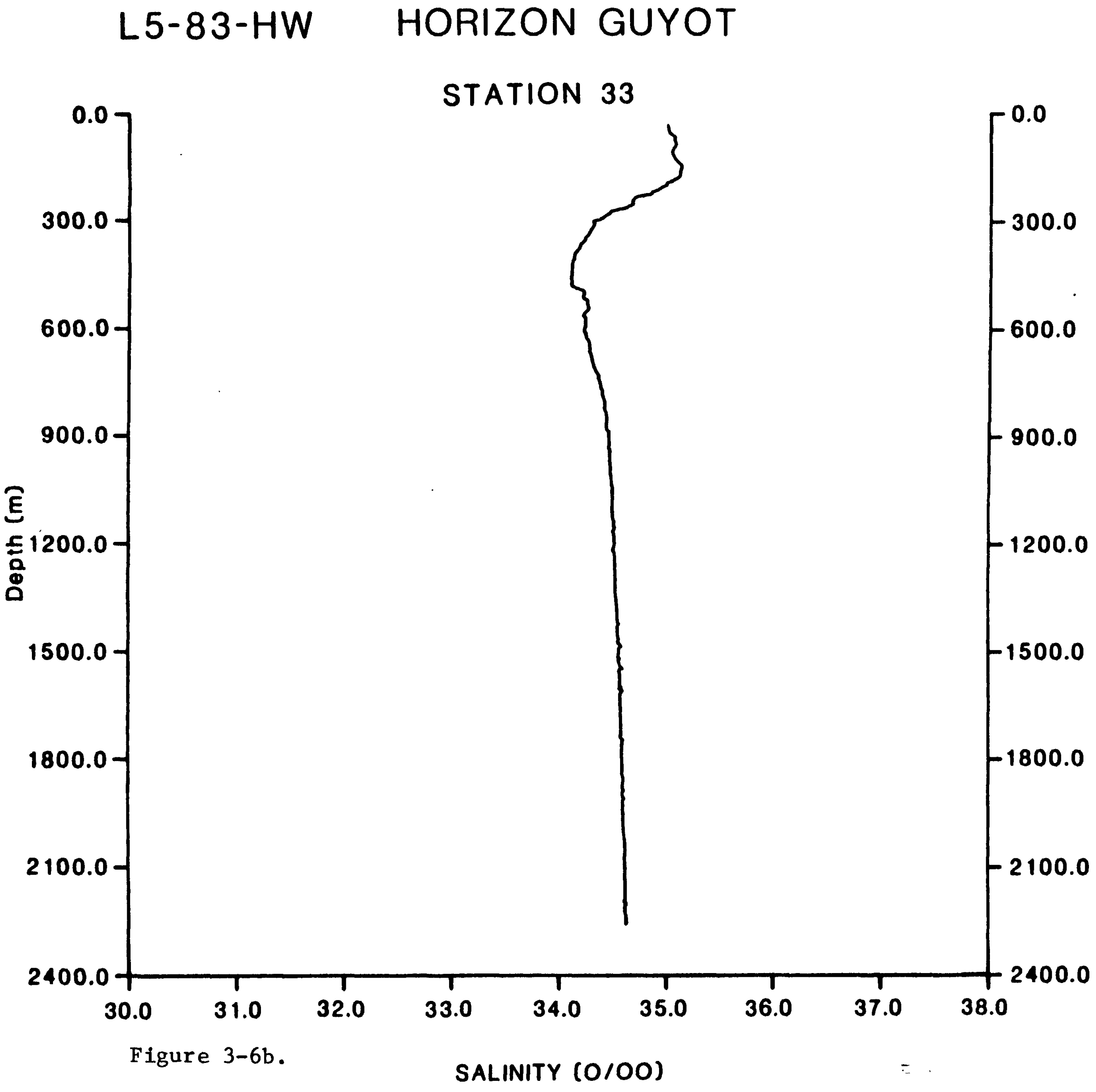
L5-83-HW HORIZON GUYOT
STATION 33
Depth (m)
0.0
300.0
600.0
900.0
1200.0
1500.0
1800.0
2100.0
2400.0
30.0
31.0
32.0
33.0
34.0
35.0
36.0
37.0
38.0
SALINITY (O/OO)

Figure 3-6b.

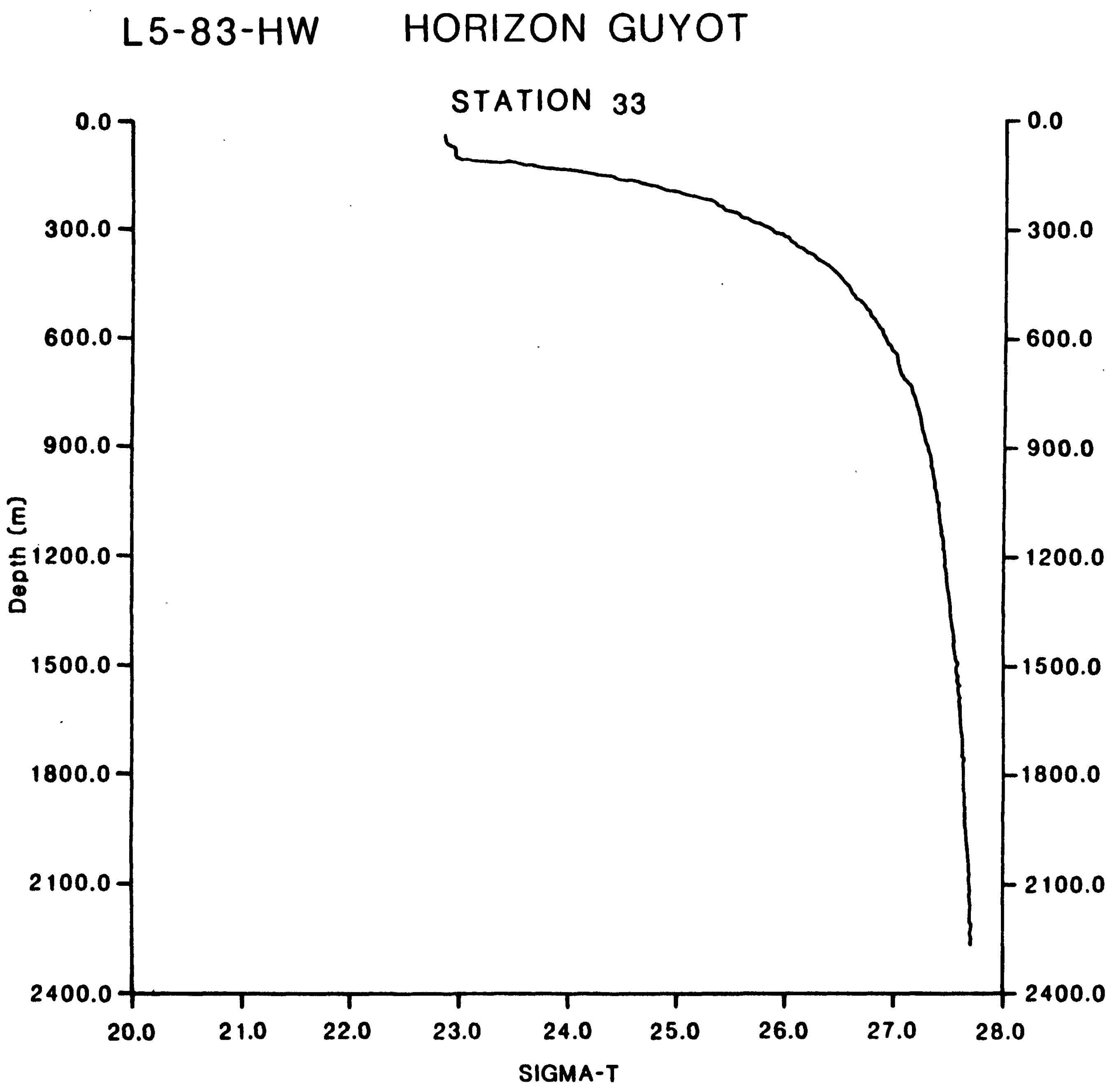

Figure 3-6c

3-6c

where g = 980.2 cm/s^2 (gravitational acceleration), ρ' is the average density over the stratified layer, and $d\rho/db$ is the vertical gradient of density, ρ, with water depth, b. In the near-linear density profile above the guyot cap, N = 1.56 rad/s or N = 0.9 cph.

The salinity profiles generally lack structure, and decrease only slightly below water depths of about 1000 m (Figs. 3-5b and 3-6b). At about 450-500 m water depth, a pronounced salinity minimum of about 34.11^o/oo is seen in the profile (Fig. 3-6b). This feature is well-known and is associated with the relatively low salinity of the Pacific Intermediate Water mass that underlies the warmer, more saline Central Water mass in the north Pacific Ocean (Sverdrup and others, 1942; Reid, 1973).

Discussion

The current meter data contain two striking results: (1) the magnitude of the M_2 tidal current is greater than that expected for mid-ocean depths, and (2) considerable variability in the M_2 tidal current occurs over the 9-month record. The first of these results was reported earlier by Lonsdale and others (1972), based on short-term deployments of near-bottom current meters at three locations, two at 12 m and one at 4 m above the bottom atop Horizon Guyot. Lonsdale and others (1972) reported maximum tidal currents of 17 cm/s at 12 m above the bottom, and a mean speed between 1 and 2 cm/s at each of the sites. A progressive vector plot of currents at 4 m above the bottom indicated a slow north-northeasterly drift (Lonsdale and others, 1972, p. 311). However, this residual or net drift is based on a short data record (5 days), and since the tidal fluctuations are relatively large by comparison, the direction is not statistically meaningful. Our data, taken over 9 months, show a current maxima of nearly 30 cm/s at 213 m above the bottom, a mean speed of 1.5 cm/s and a net southeasterly drift.

Our data also show considerable variability in both the currents and temperature. Maximum M_2 tidal current speeds increase during March-May, and are time-correlated with an increase in both the mean temperature and the magnitude of the tidal thermal fluctuations. The low frequency current changes dramatically during the Spring, increasing in speed to a maximum of about 15 cm/s and persistently flowing toward the southeast. No explanation for the variability in either the tidal currents or the low frequency flow can be given based on this single data set.

Current meter measurements obtained in the middle and near-bottom water depths of the central north Pacific Ocean commonly have significant peaks in spectral kinetic energy at the semidiurnal and inertial frequencies. Benthic current observations of Hayes (1979) within 200 m of the sea floor in about 5000 m water depth at three locations far to the southeast of Horizon Guyot showed maximum M_2 tidal currents of about 6 to 7 cm/s. Hayes (1979) argued that this tidal motion was dominantly baroclinic, and that the M_2 current speeds increased toward the sea floor. He proposed that this downward increase in internal tidal energy toward the bottom might be caused by the generation of the internal tide by barotropic tidal motion over proximal, low abyssal hills. Mean currents were small (0 to 2 cm/s) and toward the northwest (Hayes, 1979).

In mid-water depths (1900 to 2800 m) of the central north Pacific between 30°N and 35°N and 140°W to 150°W, Earle (1975) reported relatively large values of spectral kinetic energy in both inertial and semi-diurnal bands. A time-series plot of half-hourly values of currents at 1900 m water depth showed peak speeds of about 6 to 8 cm/s which Earle (1975) ascribed principally to M_2 tidal and inertial motions. Earle (1975) also reported a general increase in semi-diurnal energy density near the bottom, and proposed that barotropic tidal flow over abyssal hills might generate semi-diurnal internal tides, and thereby increase the energy at this frequency. Mean current speed at each of the current meters was always less than 2 cm/s (Earle, 1975).

The principal point to be noted is the relatively low values of the hourly current speeds in the available current records for mid- and deep-ocean water depths when compared to the Horizon Guyot measurements (Fig. 3-2). Our data show a five-fold increase in current speeds above other data that have similar spectral structure and that were taken from relatively long-term records in mid- and near-bottom water depths of the north central Pacific Ocean.

Lonsdale and others (1972) argued that a possible cause of the anomalously high semi-diurnal tidal currents above Horizon Guyot was the intensification of the M_2 internal tide over the guyot's surface. Theoretical and laboratory studies by Wunsch (1969) and Cacchione and Wunsch (1974) have shown that bottom velocities caused by internal waves propogating over an inclined bottom intensify upslope. The behavior of the waves in this shoaling process is largely governed by the ratio of bottom slope, γ, to the inclination of the internal wave characteristics, c (Wunsch, 1969). The later describes the direction of energy propagation for single frequency internal waves for which non-linear effects have been neglected, and is usually given as:

$$c^2 = [(\omega^2-f^2)/(N^2-\omega^2)] \qquad (2)$$

where ω is the internal wave frequency, f is the local inertial frequency ($f=\sin\phi$; ϕ is latitude); and N is the Brunt-Vaisala frequency (Equation 1).

Using the location and available density profiles for Horizon Guyot, we find that $f=2.69\text{x}10^{-2}$ cph ($\phi=19°30'$ N), and N=0.9 cph. Therefore, for the semi-diurnal frequency ($\omega=8.065\text{x}10^{-2}$ cph) we obtain c=0.085. The sediment cap on Horizon Guyot ranges in water depth from about 2000 m to about 1400 m. Based on bathymetric profiling (Fig. 1-3), the bottom slope over the lower section of the cap between water depths of 2000 and 1600 m is about 0.04; toward the top of the guyot from water depths of 1600 to 1440 m the bottom gradient decreases to about 0.02. Lonsdale and others (1972) made similar estimates and reported that c was about 0.07 (note: they used N=1.1 cph), and that γ was between 0.026 and 0.035. Therefore, based on both sets of results, $\gamma/c\cong0.5$ for the lower section of the guyot top; and $\gamma/c\cong0.2$ over the upper portion.

For cases with $\gamma/c<1$, Cacchione (1970) found that the theoretical solutions of Wunsch (1969) adequately predicted the upslope increases in bottom current velocities due to shoaling internal waves. In the laboratory cases with $\gamma/c<1$, the internal wave energy propagated upslope with increasing slope-parallel bottom velocities until internal-wave breaking occurred (Cacchione and Wunsch, 1974). The magnitude of the upslope amplification in the laboratory cases tested was about 5 to 10 times the input velocities.

Therefore, we propose that one possible explanation for the high M_2 tidal currents above Horizon Guyot is intensification of the bottom velocities by the shoaling process. Assuming that the internal tide is generated in the mid-ocean pycnoline by interaction of barotropic tidal flows or low frequency currents with topographic irregularities (like guyots and ridges) as has been proposed by others (Prinsenberg and Rattray, 1975), then we predict that the internal tidal motion will be intensified over the gently sloping surfaces of the guyot cap. Near-bottom current velocities above the guyot would then be higher than the input internal tidal velocities in the mid- and deep-water of the nearby open ocean.

An additional possibility is that the internal M_2 tide breaks down well up onto the shallowest sections of the guyot through a boundary instability caused by the shoaling effects (Cacchione, 1970), giving rise to higher frequency internal waves and enhanced near-bottom turbulence. There is some indication in the K.E. spectra at 213 m above the bottom (Figs. 3-4a to 3-4c) that internal motions at frequencies higher than semi-diurnal are present. The higher frequency waves and the water motions caused by the turbulent mixing along the boundary might explain the presence of the small, symmetrical sand ripples in the bottom photographs (Fig. 1-3). The most common pattern of ripples on Horizon Guyot is straight, sharp-crested symmetrical ripples with wavelengths that vary from 10 to 35 cm (Lonsdale and others, 1972). Cacchione and Southard (1974) observed that nearly symmetrical ripples in artificial sediment were generated by shoaling internal-interfacial waves in a large tank. The height and length scales of the sediment ripples were not simply related to the spatial scales of the interfacial waves, but probably were related to the scale of the boundary layer turbulence. In the internal wave laboratory experiments for which γ/c was not greatly less than unity, that is, for which the internal wave energy propagated upslope at an inclination that was close to the bottom slope, each internal wave formed a bore-like feature which dissipated in a thin energetic zone of internal runup and backwash (Cacchione, 1970). A similar result occurred shoreward of the zone of breaking for the interfacial wave experiments, in the region of bottom slope where the ripples formed in the artificial sediment (Cacchione and Southard, 1974). We hypothesize that a similar intense zone of boundary flow driven by the shoaling internal tide might be responsible for the bedforms on Horizon Guyot. Obviously, more field data on the boundary currents above the guyot are needed to test this idea.

Evidence for erosion is found along the northwestern and southeastern rim of Horizon Guyot. Lonsdale and others (1972) and more recent data (Chapter I, this report) show a pattern of exhumed terraces, rock outcrops and truncated strata along the rim of the long sides of the guyot. It is interesting that the hourly-averaged currents have a preferred orientation to the NW-SE. This suggests that the M_2 tidal currents are incident to the guyot at the sides of most active erosion. Furthermore, the most energetic low frequency flows, March-April (Fig. 3-2), also had a southeasterly direction.

Lonsdale and others (1972) described the directions of sediment transport to be orthogonal upslope on both northwest and southeast sides of the ridge that forms Horizon Guyot. These transport paths were inferred from features on the oriented bottom photographs (Fig. 1-3), including the orientation of asymmetric ripples, the orientation of asymmetric sand waves (found at one location in the Deep-Tow study area; Fig. 1-4) with wavelengths of about 30 m, and heights of about 1 m, and scour marks, lee deposits, and modified ripple patterns around exposed fragments of rock. Sand waves and ripples migrating toward the top of banks have been observed in tidal flows in shallow water (Caston and Stride, 1970).

Implications for sediment movement

There are several indications of active sediment movement and erosion on Horizon Guyot. Data collected during cruise L9-84-CP (Chapter I) and by Lonsdale and others (1972) show truncated sedimentary horizons and exhumed, hard chert layers along the margins of the guyot cap, and winnowed surficial foraminiferal sand that in several locations has been molded into sand waves and ripples. The shallowest core which was recovered by Lonsdale and others (1972) and is located in Fig. 1-2 (core 29G) was 26-cm-long and consisted of a fine to medium Eocene and Quaternary foraminiferal sand underlain by a Pliocene, nanno-rich foraminiferal silty sand. Lonsdale and others (1972) interpreted the sandy upper section to represent the effects of current winnowing. Other cores recovered by Lonsdale and others (1972) at slightly deeper locations on the guyot top did not show well-defined sorting of the surficial sediment, although there was upward coarsening in the sections.

Cores recovered during cruises L5-83-HW and L9-84-CP (fig. 1-2) also showed evidence for winnowing. Core GC-6 (Fig. 1-2) had a sand content of >80% at a subsurface depth of 12 cm. Other cores had badly disturbed tops, but in their uppermost sections had enriched sand content.

The resuspension and mobility of the bottom sediment on the guyot cap is closely linked to the specific grain density of the foraminiferal tests. Threshold conditions for movement of sandy bottom sediment on a flat bottom are usually given in terms of the critical Shield's parameter, ψ_c (Smith, 1977), which defines the ratio of skin friction, τ_c, to the submerged weight of the particles at the time of initial motion:

$$\psi_c = \tau_c/[(\rho_s - \rho)gD] \qquad (3)$$

where ρ_s and ρ are grain and fluid densities, respectively, $g = 980$ cm/s^2 and D is the mean particle diameter. Lonsdale and others (1972) estimated that for particles with an average density of 1.46 g/cc (planktonic foraminifera) and $D = 0.03$ cm (medium sand), $\psi_c = .05$, leading to a value of $\tau_c = 0.675$ dynes/cc from equation 3. Our data suggest that $D = 0.025$ cm (fine to medium sand) for the uppermost granular materials in the cores.

Additionally, we conducted settling velocity experiments on the foram sand recovered from the tops of cores (Fig. 1-2) to test the density equation for hollow particles formulated by Bachman (1984). Our work basically confirmed Backman's (1984) results, and extended the useful range of his work to include finer sands. Our data suggest that for $D = 0.25$ mm, $\rho_s = 1.80$ g/cc, for $D = 0.125$ mm, $\rho_s = 2.40$ g/cc and for $D = 0.0625$ mm, $\rho_s = 2.73$ g/cc. Therfore, assuming a mean grain diameter in the surficial material as $D = 0.025$ cm, we chose $\rho_s = 1.8$ g/cc in the following initiation of motion analysis.

Using the modified Shield's diagram given by Grant and Madsen (1982) we find that for $D = 0.025$ cm and $\rho_s = 1.8$ g/cc, $\psi_c = 0.058$. The difference between our estimated value of ψ_c and that found by Lonsdale and others (1972) is insignificant considering the possible errors in the selections of D and ρ_s. From equation 3 we then estimate that τ_c will be about 1.14 dynes/cm^2, a value about 40% larger than that estimated by Lonsdale and others (1972). The difference can again be explained by the slightly different values of D and ρ_s. Based on the quadratic stress law, the total shear stress, τ, is expressed by:

$$\tau = c_d \rho u^2 \qquad (4)$$

where c_d is a bottom drag coefficient at 1 m above a physically roughened bed (ripples), and u is the mean current speed at 1 m above the bed. Lonsdale and others (1972) calculated that a current speed of $u = 17$ cm/s would be necessary to initiate sediment movement when the bottom drag coefficient ($c_d = 2.2 \times 10^{-3}$) was obtained from sediment transport studies in shallow water tidal flow over a rippled quartz sand (Sternberg, 1968).

The velocity profile in fully turbulent flow over a rough bed is usually described by the "law of the wall" (Smith, 1977):

$$u/u_* = (1/k) \ln (z/z_o) \qquad (5)$$

where the shear velocity, $u_* = (\tau/\rho)^{1/2}$, u is the mean flow speed at a level z above the sea floor, z_o is the roughness parameter and k is von Karman's constant (0.4). It can be readily seen from equations 4 and 5 that:

$$1/c_d = (u/u_*)^2 = [(1/k) \ln (z/z_o)]^2 \qquad (6)$$

Recent analyses of bed roughness for tidal flows over rippled sands (Heathershaw, 1981; Rubin and McCullouch, 1980) indicate that z_o is approximately bounded by $0.05 \text{ cm} < z_o < 0.25$ cm. Assuming the bounding values of z_o, we find from equation 6 that $2.8 \times 10^{-3} < C_d < 4.5 \times 10^{-3}$, somewhat larger than the estimates used by Lonsdale and others (1972). The principal reason for this discrepancy is a larger form drag contribution from the ripples.

It is difficult to estimate the flow speeds at large distances from the bed necessary to resuspend the bottom sediment without more knowledge of the internal boundary layer structure. That is, there is no explicit means to match the bottom logarithmic part of the tidal boundary layer (Equation 5) to the upper portion. Some estimates of deep oceanic boundary layers suggest that the thickness of the lowest logarithmic portion of the boundary layer is given approximately by:

$$\delta_1 = 0.1\, u_*/f_d \qquad (9)$$

where f_d is the frequency of the dominant motion (tidal or inertial). If we assume that $u_* = 1.1$ cm/s (for initiation of motion) and $fd = 1.43 \times 10^{-4}$ rad/s (M_2 tide), then $\delta_1 = 7.7$ m. At this distance above the sea floor, using equation 5, we estimate that initiation of motion of the rippled bottom sediment ($z_o = 0.1$ cm) would require $u > 24$ cm/s. Our measurements show that at 213 m above the sea floor, maximum tidal current velocities were nearly

30 cm/s during March-May, 1984 (Fig. 3-2). If these currents do not diminish appreciably toward the bed until the logarithmic layer is reached, we would expect that critical conditions for sediment movement are reached during this period. At this time, the ripples are probably actively formed, and bottom sediment is transported along the guyot cap.

In the areas where the larger bedforms occur, the current at the top of the boundary layer must achieve much higher speeds to mobilize the sediment forming the sand waves (Rubin and McCulloch, 1980). A more detailed analysis of the magnitude of the critical stress and current speeds necessary to cause sand-wave migration is not possible without more detailed flow measurements above the guyot cap. The work of Rubin and McCulloch (1980) on large quartz sand waves in San Francisco Bay (mostly depth-limited boundary layers) suggests that flow speeds exceeding 50 cm/s near the top of the boundary layer might be needed to initiate sediment transport in the large dunes. This critical flow speed would likely be reduced considerably for lower density material (ρ_s = 1.8 g/cc for fine to medium foram sand) as was discussed above, and the necessary speeds to mobilize the foram-sand waves will likely be lower than 50 cm/s.

Conclusions

We have found that the currents recorded over a 9 month period in 1983-1984 at 213 m above Horizon Guyot are dominated by M_2 tidal flow. These tidal currents are intensified relative to other tidal currents measured in the north central Pacific, and probably are the result of topographic intensification of the internal tide that propagates across the guyot cap. The generation mechanism of the semi-diurnal internal tide is not definitly known, but most likely this motion is forced by either the barotropic tidal currents or the low frequency flow that passes over the guyot rim (or over nearby ridges and seamounts). The correlation of the maximum internal tidal currents with the period of maximum low frequency flows during March-May, 1984 suggests that the principal generating mechanism is the low frequency current. Energy in the inertial frequency band is considerably reduced relative to the M_2 tide (by about one order of magnitude), and the inertial peak appears as broad and ill-defined.

The low frequency currents achieve peak speeds of about 15 cm/s toward the southeast, normal to the elongate NE-SW orientation of the Guyot, during the Spring. This southeasterly low-frequency flow is in marked contrast to the generally lower speeds and variable directions during the other parts of the record.

Estimates of the mobility of the bottom sediment, which at the surface of the guyot cap is dominantly a fine to medium foram sand, indicate that the internal tidal currents probably form the small sediment ripples during the period of maximum flow (March-May, Fig. 3-2). Lonsdale and others (1972) had earlier proposed that the bottom sediment was probably transported by internal tidal currents. The combination of 30 cm/s peak internal tidal current speeds and 15 cm/s peak low frequency flows during March-May, giving a maximum possible combined flow speed of 43 cm/s, suggests that there could be movement of the foram sand in the large sand waves. Causes and mobility of the large sand waves are uncertain, however, and more data on the velocity structure above these bedforms are needed to investigate their formation and migration rates.

Nomenclature

b - Water depth.
c - Inclination of the internal wave characteristics.
c_d - Bottom drag coefficient.
f - Local inertial frequency.
f_d - Frequency of the dominant tidal or inertial motion.
g - Gravitational acceleration.
k - von Karman's constant.
N - Brunt-Vaisala frequency.
u - Mean current speed.
u_* - Shear velocity.
z - Height above the sea floor.
z_o - Roughness parameter.
γ - Slope of sea floor.
δ_1 - Thickness of the lowest logarithmic portion of the boundary layer.
ρ - Fluid density.
ρ' - Average fluid density.
ρ_s - Grain density.
τ - Total stress at 1 m above the sea floor.
τ_c - Skin friction.
ϕ - Latitude.
ψ_c - Critical Shield's parameter.
ω - Internal wave frequency.

IV. ACKNOWLEDGEMENTS

Many people were responsible for the success of this multidisciplinary investigation. The authors would like to thank Jim Hein and Frank Manheim, the co-chief scientists of cruise L5-83-HW, for their cooperation and Peter Lonsdale (SCRIPPS) for allowing us access to his Deep Tow data. Carol Hirozawa (U.S.G.S.) worked extremely hard on the micropaleontologic analyses and David Bukry's (Minerals Management Service) adivse and expertise was deeply appreciated. In these times of restricted budgets and on-again off-again cruises, we appreciate Peter Halbach's (Clausthal University, W. Germany) offer to use the research vessel SONNE as a backup to retrieve the current-meter mooring. We would like to thank Polly Shoukimas (USGS) for translating the VACM tapes and Brad Butman (USGS) and Bill Strahle (USGS) for their help in equipment preparation, and the crew of the R/V S.P. LEE. Finally, we would like to thank Elizabeth Winget, Dave Drake, Page Valentine, Wylie Poag, Bill Winters, and Brad Butman, all from the USGS for their helpful discussions and reviews of the manuscript, and Patty Forrestal, Dan Blackwood, and Susan Peterson for their aid in preparation of the manuscript.

V. REFERENCES

American Society for Testing and Materials (ASTM), 1983, Annual Book of ASTM Standards, part 19, Natural Building Stones; Soil andRock, ASTM, Philadelphia, 710 p.

Blatt, H., Middleton, G.V., and Murray, R., 1972, Origin of Sedimentary Rocks: Prentice-Hall, Inc., Engelwood Cliffs, N.J., 634 p.

Blow, W.H., 1971, Deep Sea Drilling Project, Leg 6, Foraminifera from selected samples, IN Fischer, A.G., and others, Initial Reports DSDP: vol. 6, Washington, D.C., p. 1013-1026.

Budinger, T.F., 1967, Cobb Seamount: Deep-Sea Research, vol. 14, p. 191-201.

Bukry, David, 1971, Cenozoic calcareous nannofossils from the Pacific Ocean: Transactions, San Diego Society of Natural History, vol. 16, no. 14, 327 p.

Bukry, David, 1973, Phytoplanktonic stratigraphy, central Pacific Ocean, DSDP Leg 17, IN Winterer, E.L., and others, Initial Reports of DSDP, vol. 17, Washington, D.C., p. 871-889.

Cacchione, D.A., 1970, Experimental study of internal waves on a slope: Ph.D. dissertation, Dept. of Earth and Planetary Sciences, Mass. Inst. of Tech., 226 p.

Cacchione, D.A., and Wunsch, C.I., 1974, Experimental study of internal waves over a slope: Journal of Fluid Mechanics, vol. 66, p. 223-239.

Cacchione, D.A., and Southard, J.B., 1974, Experiments on bottom sediment movement by breaking internal waves, IN Swift, D., Duane, D., and Pilkey, O.H., eds., Shelf Sediment Tranport: Dowden, Huchinson, and Ross, Stroudsburg, PA, p. 83-97.

Carver, R.E., 1971, Procedures in sedimentary petrology: John Wiley and Sons, Inc., New York, 653 p.

Casagrande, Arthur, 1936, The determination of the pre-consolidation load and its practical significance: Soil Mechanics and Foundation Engineering, vol. III, Cambridge, MA, p. 60-64.

Caston, V., and Stride, A., 1970, Tidal sand movement between some linear sand banks in the North Sea off northeast Norfolk: Marine Geology, vol. 9, p. 38-48.

Clague, D.A., 1981, Linear island and seamount chains, aseismic ridges, and intraplane volcanism: Results from DSDP, IN Warme, J.E., Douglas, R.G., and Winterer, E.L., eds., The deep sea drilling project: a decade of progress: Society of Economic Paleontologists and Mineralogists, Special Publication No. 32, p. 7-22.

Craig, J.D., Andrews, J.E., and Meyland, M.A., 1982, Ferromanganese deposits in the Hawaiian Archipelago: Marine Geology, vol. 45, p. 127-139.

Douglas, R.G., 1973, Planktonic foraminiferal biostratigraphy in the central North Pacific Ocean, IN Winterer, E.L., and others, Initial Reports of the Deep Sea Drilling Project: Washington, D.C., vol. 17, p. 673-694.

Earle, M.D., 1975, Current measurements in the eastern central North Pacific Ocean: Deep Sea Research, vol. 22, p. 875-881.

Fischer, A.G., Heezen, B.C., and others, 1971, Initial reports of the Deep Sea Drilling Project, vol. VI, Washington, D.C., U.S. Government Printing Office, 1329 p.

Goddard, E.N., 1970, Chairman of the Rock Color Chart Committee: Boulder, CO, distributed by the Geological Society of America, 10 p.

Grant, W.D., and Madsen, O.S., 1982, Moveable bed roughness in unsteady oscillatory flow: Journal of Geophysical Research, vol. 87, p. 469-481.

Halbach, Peter, and Manheim, F.T., 1984, Potential of cobalt and other metals in ferromanganese crusts in seamounts of the central Pacific Basin: Marine Mining, vol. 4, pno. 4, p. 319-336.

Halpern, D., 1979, Observations of upper ocean currents at DOMES sites A, B, and C in the tropical North Pacific Ocean during 1975 and 1976, IN Bischoff, J.L., and Piper, D.Z., eds., Marine Geology and Oceanography of the pacific manganese nodules province: Plenum Publishers, New York, p. 43-82.

Hamilton, E.L., 1953, Upper Cretaceous, Tertiary, and recent planktonic foraminifera from mid-Pacific flat-topped seamounts: Journal of Paleontology, vol. 27, no. 2, p. 204-237.

Hay, W.W., 1971, Preliminary dating by fossil calcareous nannoplankton, Deep Sea Drilling Project: Leg 6, IN Fischer, A.G., and others, Initial Reports of the Deep Sea Drilling Project, vol. 6, Washington, D.C., p. 1005-1012.

Hayes, M.C., 1979, Benthic current observations at DOMES sites A, B, and C in the tropical North Pacific Ocean, IN Bischoff, J.L., and Piper, D.Z., eds., Marine geology and oceanography of the Pacific manganese nodules province: Plenum Publishers, New York, p. 83-112.

Heezen, B.C., Fischer, A.G., and others, 1971, Site 44, IN Fischer, A.G., and others, Initial reports of the Deep Sea Drilling Project, vol. 6, Washington, D.C., p. 17-39.

Hein, J.R., Manheim, F.T., Schwab, W.C., and Clague, D.A., 1986, Cobalt-rich manganese crust potential from the central Pacific: Proceedings 18th Annual Offshore Technology Conference, Houston (in press).

Hein, J.R., Manheim, F.T., Schwab, W.C., and Davis, A.S., 1985b, Ferromanganese crusts from Necker Ridge, Horizon Guyot, and S.P. Lee Guyot: Geological Considerations: Marine Geology, vol. 69, p. 25-54.

Hein, J.R., Manheim, F.T., Schwab, W.C., Davis, A.S., Daniel, C.L., Bouse, R.M., Morgenson, L.A., Sliney, R.E., Clague, D.A., Tate, G.B., and Cacchione, D.A., 1985a, Geological and geochemical data for seamounts and associated ferromanganese crusts in and near the Hawaiian, Johnston Island, and Palmyra Island Exclusive Economic Zones: U.S. Geological Survey Open-File Report 85-292, 129 p.

Heirtzler, J.R., Taylor, P.T., Ballard, R.D., and Houghton, R.L., 1977, A visit to the New England Seamounts: American Scientist, vol. 65, p. 466-472.

Hess, H.H., 1946, Drowned ancient islands of the Pacific basin: American Journal of Science, vol. 244, p. 772-791.

Jackson, E.D., Koizumi, I., and others, 1978, Initial reports of the Deep Sea Drilling Project, Washington, D.C., vol. 55, 1320 p.

Johnson, D.A., and Lonsdale, P.F., 1976, Erosion and sedimentation around Mytilus Seamount, New England continental rise: Deep Sea Research, vol. 23, p. 429-440.

Karig, D.E., Peterson, M.N.A., and Shor, G.G., Jr., 1970, Sediment-capped guyots in the mid-Pacific Mountains: Deep Sea Research, vol. 17, p. 373-378.

Keller, J.B., and Mow, V.C., 1969, Internal wave propagation in an inhomogeneous fluid of non-uniform depth: Journal Fluid Mechanics, vol. 38, p. 365-374.

Krashininhikov, V.A., 1971, Cenozoic foraminifera, IN Fischer, A.G., Heezen, B.C., and others, Initial Reports of the Deep Sea Drilling Project, vol. VI, Washington, D.C., U.S. Government Printing Office, p. 1055-1068.

Ladd, C.C., and Foott, Roger, 1974, New design procedure for the stability of soft clays: Journal of Geotechnical Engineering Division, ASCE, vol. 100, no. GT7, p. 763-786.

Ladd, C.C., Foott, Roger, Ishihara, K., Schlosser, F., and Paulos, H.G., 1977, Stress-deformation and strenght characteristics: Proceedings, 9th International Conference on Soil Mechanics and Foundation Engineering, Tokyo, vol. 2, p. 421-494.

Lee, H.J., Edwards, B.D., and Field, M.E., 1981, Geotechnical analysis of a submarine slump, Eureka, CA, IN Proceedings, 13th Offshore Technology Conference, Houston, OTC 4125, p. 53-65.

Lee, H.J., and Edwards, B.D., 1986, Regional method to assess offshore slope stability: Journal of the Geotechnical Engineering, ASCE, vol. 112, p. 489-509.

Lee, H.J., and Schwab, W.C., 1983, Geotechnical framework, northeast Gulf of Alaska: U.S. Geological Survey Open-File Report 83-499, 417 p.

Lonsdale, P.F., Normark, W.R., and Newman, W.A., 1972, Sedimentation and erosion on Horizon Guyot: Geological Society of America, Bulletin, vol. 83, p. 289-316.

Manheim, F.T., 1986, Cobalt resources: Science (in press).

Mayne, P.W., 1980, Cam-Clay predictions of the undrained strength: Journal of the Geotechnical Engineering Division, ASCE, vol. 106, no. GT11, p. 1219-1242.

Mayne, P.W., 1985, Stress anisotropy effects on clay strength: Journal of the Geotechnical Engineering Division, ASCE, vol. 111, no. GT3, p. 356-366.

McManus, D.A., and Morrison, D.R., 1968, Quinn Guyot (GA-3) not tilted toward the Atlantic Trench: Marine Geology, vol. 7, p. 365-368.

Morgenstern, N.M., 1967, Submersible slumping and the initiation of turbidity currents, In Richards, A.F., ed., Marine Geotechnique, University of Illinois Press, p. 189-220.

Noble, Marlene, Rosenseld, L.K., Robert, R., Smith, L., Gardner, J.D., and Beardsley, R.C., 1986, Tidal currents seaward of the northern California continental shelf: Journal of Geophysical Research (in press).

Nowrooski, A.A., Ewing, M., Nafe, J.E., and Fliegel, M., 1968, Deep ocean current and its correlation with the ocean tide off the coast of northern California: Journal of Geophysical Research, vol. 73, p. 1921-1932.

Pimm, A.C., 1971, Grain size results and composition of the sand fraction, Leg VI, IN Fischer, A.G., and others, Initial Reports of the Deep Sea Drilling Project, Washington, D.C., vol. 6, p. 709-737.

Postuma, J.A., 1971, Manual of planktonic foraminifera: Amsterdam, Elsevier Publ. Co., 420 p.

Pratt, R.M., 1963, Great Meteor Seamount: Deep-Sea Research, vol. 10, p. 17-25.

Prinsenberg, S.J., and Rattray, M., 1975, Effects of continental slope and variable Brunt-Vaisala frequency on the generation of internal tides: Deep-Sea Research, vol. 22, p. 251-263.

Reid, J.L., Jr., 1973, The shallow salinity minima of the Pacific Ocean: Deep-Sea Research, vol. 20, p. 51-68.

Roberts, D.G., Hogg, N.G., Bishop, D.G., and Flewellen, C.G., 1974, Sediment distribution around moated seamounts in the Rockall Trough: Deep-Sea Research, vol. 21, p. 175-184.

Roth, P.H., 1973, Calcareous nannofossils, Leg 17, DSDP, IN Winterer, E.L., and others, Initial Reports of the Deep Sea Drilling Project, Washington, D.C., vol. 17, p. 695-795.

Rubin, D.M., and McCulloch, D.S., 1980, Single and superimposed bedforms: a snynthesis of San Francisco Bay and flume observations: Sedimentary Geology, vol. 26, p. 207-231.

Sangrey, D.A., 1977, Marine Geotechnology - state of the art: Marine Geotechnology, vol. 2, p. 45-80.

Schwab, W.C., and Bailey, N.G., 1985, High-resolution seismic-reflection data collected on R/V S.P. LEE: L9-84-CP, Marshall Islands to Hawaii: U.S. Geological Survey Open-File Report 85-24, 6 p.

Schwab, W.C., and Lee, H.J., 1983, Geotechnical analysis of submarine landslides in glacial-marine sediment, northeast Gulf of Alaska, IN Molnia, B.F., ed., Glacial-marine sedimentation: Plenum Publ., New York, p. 145-184.

Schwab, W.C., Hein, J.R., Davis, A.S., Morgenson, L.A., Daniel, C.L., and Haggerty, J.A., 1986, Geological and geochemical data for seamounts and associated ferromanganese crusts in the Ratak Chain, Marshall Islands: U.S. Geological Survey Open-File Report 86-338, 26 p.

Smith, J.D., 1972, Modeling of sediment transport on continental shelves, IN Goldberg, E.D., McCave, I.N., O'Brien, J.J., and Steele, J.H., eds., The Sea: Interscience, New York, vol. 6, p. 313-332.

Stainforth, R.M., and others, 1975, Cenozoic planktonic foraminiferal zonation and characteristics of index forms: Univ. Kansas Paleo. Contr. Article 62, 425 p.

Sternberg, R.S., 1968, Friction factors in tidal channels: Marine Geology, vol. 6, p. 243-260.

Sverdrup, H.U., Johnson, M.W., and Fleming, R.H., 1942, The oceans: their physics, chemistry, and general biology: Prentice-Hall, Inc., New Jersey, 1087 p.

Taylor, P.T., Stanley, D.J., Simkin, Tom, and John, Walter, 1975, Gilliss Seamount: detailed bathymetry and modification by bottom currents: Marine Geology, vol. 19, p. 139-157.

Toth, J.R., 1968, Deposition of submersible crusts rich in manganese and iron: Geological Soceity of America, Bulletin, vol. 91, p. 44-54.

Uchupi, Elazar, Phillips, J.D., and Prada, K.E., 1970, Origin and structure of the New England Seamount chain: Deep-Sea Research, vol. 17, p. 483-494.

Valent, P.J., 1979, Engineering behavior of two deep ocean calcareous sediments, including influence on the performance of the Propellant Driven Anchor: Ph.D. dissertation, Purdue University, 343 p.

Winterer, E.L., Ewing, J.I., and others, 1973, Initial reports of the Deep-Sea Drilling Project, vol. 17, Washington, D.C., 1283 p.

Winters, W.J., and Lee, H.J., 1982, Evaluation of geotechnical properties and slope stability of a calcareous ooze on the southwest slope off Oahu, Hawaii: U.S. Geological Survey Open-File Report 82-468b, 273 p.

Wissa, A.E., Ladd, C.C., and Lambe, T.W., 1965, Effective stress strength parameters of stabilized soils: 6th International Conference, International Society of Soil Mechanics and Foundation Engineering, Professional Paper no. P64-28.

Wissa, A.E., Christian, J.T., Davis, E.H., and Heiberg, Sigord, 1971, Consolidation at constant rate of strain: Journal of Soil Mechanics and Foundations Division, ASCE, vol. 97, no. SM10, p. 1393-1413.

Wunsch, C.I., 1969, Progressive internal waves on slopes: Journal of Fluid Mechanics, vol. 35, p. 131-144.